Understanding local electronic structure variations in bio-inspired aromatic molecules

Kumulative Dissertation

zur Erlangung des akademischen Grades
doctor rerum naturalium
(Dr. rer. nat.)
in der Wissenschaftsdisziplin
Experimentalphysik

eingereicht an der
Mathematisch-Naturwissenschaftlichen Fakultät
der Universität Potsdam

von
Robby Büchner

Disputation am
22.06.2022

Hauptbetreuer	Prof. Dr. Alexander Föhlisch
Zweitbetreuer	Prof. Dr. Tobias Lau
Gutachter	Prof. Dr. Alexander Föhlisch
	Prof. Dr. Birgit Kanngießer
	Prof. Dr. Jan-Erik Rubensson

Published online on the
Publication Server of the University of Potsdam:
https://doi.org/10.25932/publishup-55319
https://nbn-resolving.org/urn:nbn:de:kobv:517-opus4-553192

Understanding local electronic structure variations in bio-inspired aromatic molecules

Abstract

In this thesis, the dependencies of charge localization and itinerance in two classes of aromatic molecules are accessed: pyridones and porphyrins. The focus lies on the effects of isomerism, complexation, solvation, and optical excitation, which are concomitant with different crucial biological applications of specific members of these groups of compounds. Several porphyrins play key roles in the metabolism of plants and animals. The nucleobases, which store the genetic information in the DNA and RNA are pyridone derivatives. Additionally, a number of vitamins are based on these two groups of substances. This thesis aims to answer the question of how the electronic structure of these classes of molecules is modified, enabling the versatile natural functionality. The resulting insights into the effect of constitutional and external factors are expected to facilitate the design of new processes for medicine, light-harvesting, catalysis, and environmental remediation.

The common denominator of pyridones and porphyrins is their aromatic character. As aromaticity was an early-on topic in chemical physics, the overview of relevant theoretical models in this work also mirrors the development of this scientific field in the 20th century. The spectroscopic investigation of these compounds has long been centered on their global, optical transition between frontier orbitals.

The utilization and advancement of X-ray spectroscopic methods characterizing the local electronic structure of molecular samples form the core of this thesis. The element selectivity of the near-edge X-ray absorption fine structure (NEXAFS) is employed to probe the unoccupied density of states at the nitrogen site, which is key for the chemical reactivity of pyridones and porphyrins. The results contribute to the growing database of NEXAFS features and their interpretation, e.g., by advancing the debate on the porphyrin N K-edge through systematic experimental and theoretical arguments. Further, a state-of-the-art laser pump – NEXAFS probe scheme is used to characterize the relaxation pathway of a photoexcited porphyrin on the atomic level.

Resonant inelastic X-ray scattering (RIXS) provides complementary results by accessing the highest occupied valence levels including symmetry information. It is shown that RIXS is an effective experimental tool to gain detailed information on charge densities of individual species in tautomeric mixtures. Additionally, the hRIXS and METRIXS high-resolution RIXS spectrometers, which have been in part commissioned in the course of this thesis, will gain access to the ultra-fast and thermal chemistry of pyridones, porphyrins, and many other compounds.

With respect to both classes of bio-inspired aromatic molecules, this thesis establishes that even though pyridones and porphyrins differ largely by their optical absorption bands and hydrogen bonding abilities, they all share a global stabilization of local constitutional changes and relevant external perturbation. It is because of this wide-ranging response that pyridones and porphyrins can be applied in a manifold of biological and technical processes.

Understanding local electronic structure variations in bio-inspired aromatic molecules

Zusammenfassung

In dieser Arbeit werden die Abhängigkeiten von Ladungslokalisierung und -wanderung in zwei Klassen von aromatischen Molekülen untersucht: Pyridone und Porphyrine. Der Schwerpunkt liegt auf den Auswirkungen von Isomerie, Komplexierung, Lösung (in Wasser) und optischer Anregung, die mit verschiedenen entscheidenden biologischen Anwendungen spezifischer Mitglieder dieser Gruppen von Verbindungen einhergehen. Mehrere Porphyrine spielen eine Schlüsselrolle im Stoffwechsel von Pflanzen und Tieren. Die Nukleobasen, die die genetische Information in der DNA und RNA speichern, sind Pyridonderivate. Auch mehrere Vitamine basieren auf diesen beiden Stoffgruppen. Ziel dieser Arbeit ist es, die Frage zu beantworten, wie die elektronische Struktur dieser Molekülklassen modifiziert wird, sodass die vielfältigen Funktionen in der Natur ermöglicht werden. Die sich daraus ergebenden Erkenntnisse über die Wirkung konstitutioneller und externer Einflussfaktoren ermöglichen die Entwicklung neuer Verfahren in der Medizin, Katalyse, Solar- und Umwelttechnik.

Die Gemeinsamkeit von Pyridonen und Porphyrinen ist ihr aromatischer Charakter. Da Aromatizität von Beginn der chemischen Physik an thematisiert wurde, spiegelt der Überblick relevanter theoretischer Modelle in dieser Arbeit auch die Entwicklung dieses Wissenschaftsgebiets im 20. Jahrhundert wieder. Die spektroskopische Untersuchung dieser Verbindungen konzentrierte sich lange Zeit auf die globalen, optischen Übergänge zwischen den Grenzorbitalen.

Die Anwendung und Weiterentwicklung röntgenspektroskopischer Methoden zur Charakterisierung der lokalen elektronischen Struktur von molekularen Proben bilden den Kern dieser Arbeit. Die Elementselektivität der Röntgen-Nahkanten-Absorptions-Spektroskopie (NEXAFS) wird genutzt, um die unbesetzte Zustandsdichte an den Stickstoffatomen zu untersuchen, welche für die chemische Reaktivität von Pyridonen und Porphyrinen verantwortlich sind. Die Ergebnisse tragen zum wachsenden Bestand von NEXAFS-Spektren und ihrer Interpretation bei, z.B. indem sie die Debatte über die N K-Kante von Porphyrinen durch systematische experimentelle und theoretische Argumente voranbringen. Zudem wird ein modernes Laser-Pump – NEXAFS-Probe System verwendet, um den Relaxationsprozess eines photoangeregten Porphyrins auf atomarer Ebene zu charakterisieren.

Die resonante inelastische Röntgenstreuung (RIXS) liefert komplementäre Ergebnisse, indem sie die höchsten besetzten Valenzniveaus einschließlich Symmetrieinformationen zugänglich macht. Es wird gezeigt, dass RIXS eine effektive experimentelle Methode ist, um detaillierte Informationen über die Ladungsdichten einzelner Tautomere in einem Gemisch zu erhalten. Zudem werden es die hochauflösenden RIXS-Spektrometer hRIXS und METRIXS, die im Rahmen dieser Arbeit mit in Betrieb genommen wurden, erlauben, Informationen zur ultraschnellen und thermischen Chemie von Pyridonen, Porphyrinen und vielen anderen Verbindungen zu gewinnen.

Im Hinblick auf beide Klassen biologisch inspirierter, aromatischer Moleküle wird in dieser Arbeit gezeigt, dass sich Pyridone und Porphyrine zwar durch ihre optischen Absorptionsbanden und ihre Fähigkeit zu Wasserstoffbrückenbindungen unterscheiden, aber alle Verbindungen eine globale Stabilisierung lokaler Konstitutionsänderungen und relevanter äußerer Einflüsse aufweisen. Aufgrund dieser weitreichenden Anpassung können Pyridone und Porphyrine in einer Vielzahl von biologischen und technischen Prozessen eingesetzt werden.

List of Publications

The published research, which I conducted as a PhD student, is listed below. The numbering is used to refer to the publications throughout this work. Since the studies are based on state-of-the-art synchrotron spectroscopic studies and high level theoretical modeling, they are the result of collaborative efforts and my personal contribution is indicated below.

I. How Hydrogen Bonding Amplifies Isomeric Differences in Pyridones toward Strong Changes in Acidity and Tautomerism
R. Büchner, M. Fondell, E. J. Mascarenhas, A. Pietzsch, V. Vaz da Cruz, and A. Föhlisch
The Journal of Physical Chemistry B 125, 9 (2021), 2372–2379
I planned and conducted the experiment, analyzed and interpreted the data and wrote the manuscript.

II. Targeting Individual Tautomers in Equilibrium by Resonant Inelastic X-ray Scattering
V. Vaz da Cruz, R. Büchner, M. Fondell, A. Pietzsch, S. Eckert, and A. Föhlisch
Accepted by The Journal of Physical Chemistry Letters (19.01.2022)
I largely contributed to the planning and execution of the experiment, analyzed the data and participated in the interpretation.

III. The porphyrin center as a regulator for metal–ligand covalency and π hybridization in the entire molecule
R. Büchner, M. Fondell, R. Haverkamp, A. Pietzsch, V. Vaz da Cruz, and A. Föhlisch
Phys. Chem. Chem. Phys. 23 (2021), 24765-24772
I planned and conducted the experiment, analyzed and interpreted the data and wrote the manuscript.

IV. Fundamental electronic changes upon intersystem crossing in large aromatic photosensitizers: free base 5,10,15,20-tetrakis(4-carboxylatophenyl)porphyrin
R. Büchner, V. Vaz da Cruz, N. Grover, A. Charisiadis, M. Fondell, R. Haverkamp, M. O. Senge, and A. Föhlisch
Accepted by Phys. Chem. Chem. Phys. (19.01.2022)
I planned and conducted the experiment, analyzed and interpreted the data and wrote the manuscript.

During my work as a PhD student, I also participated in the following studies, which lie outside the scope of this thesis.

1. **Measuring the atomic spin-flip scattering rate by x-ray emission spectroscopy**
R. Decker, A. Born, R. Büchner, K. Ruotsalainen, C. Stråhlman, S. Neppl, R. Haverkamp, A. Pietzsch, and A. Föhlisch
Scientific Reports 9, 1 (2019), 8977

2. **Thresholding of the Elliott-Yafet spin-flip scattering in multi-sublattice magnets by the respective exchange energies**
A. Born, R. Decker, R. Büchner, R. Haverkamp, K. Ruotsalainen, K. Bauer, A. Pietzsch, and A. Föhlisch
Scientific Reports 11, 1 (2021), 1883

3. **Spin-lattice angular momentum transfer of localized and itinerant electrons in the demagnetization transient state of gadolinium**
   R. Decker, A. Born, K. Ruotsalainen, K. Bauer, R. Haverkamp, R. Büchner, A. Pietzsch, and A. Föhlisch
   Applied Physics Letters 119, 15 (2021), 152403

4. **The manifold of molecular H_2O potential energy surfaces in liquid water at ambient conditions**
   A. Pietzsch, J. Niskanen, V. Vaz da Cruz, R. Büchner, S. Eckert, M. Fondell, R. M. Jay, X. Lu, D. McNally, T. Schmitt, and A. Föhlisch
   Under review at Proceedings of the National Academy of Sciences of the United States of America (Revision submitted on 20.01.2022)

5. **Photo-induced Ligand Substitution of $Cr(CO)_6$ in 1-pentanol Probed by Time Resolved X-Ray Absorption Spectroscopy**
   E. J. Mascarenhas, M. Fondell, R. Büchner, S. Eckert, V. Vaz da Cruz, and A. Föhlisch
   Under review at Phys. Chem. Chem. Phys. (Submitted on 21.12.2021)

6. **Elucidating the electronic structure of the products in the photo-aquation of ferrohexacyanide via multi-site transient X-ray absorption spectroscopy**
   V. Vaz da Cruz, E. J. Mascarenhas, R. Büchner, R. M. Jay, S. Eckert, M. Fondell, and A. Föhlisch
   Manuscript in preparation

7. **Time-resolved NEXAFS of photoexcited α-Fe_2O_3 nanoparticles**
   M. Fondell, R. Büchner, S. Eckert, V. Vaz da Cruz, R. Mitzner, S. Neppl and A. Föhlisch
   Manuscript in preparation

List of Abbreviations

BESSY	Berliner Elektronenspeicherring-Gesellschaft für Synchrotronstrahlung
CASSCF	Complete active space self-consistent field method
CCD	Charge-coupled device
CI	Configuration interaction
CPCM	Conductor-like polarizable continuum model
DFT	Density functional theory
DNA	Deoxyribonucleic acid
EDAX	Excited states dynamics with X-rays
EXAFS	Extended X-ray absorption fine structure
FEL	Free electron laser
HF	Hartree-Fock
HOMO	Highest occupied molecular orbital
HP	Hydroxypyridine
hRIXS	Heisenberg resonant inelastic X-ray scattering
KS	Kohn-Sham
LUMO	Lowest unoccupied molecular orbital
MD	Molecular dynamics
METRIXS	Momentum and energy transfer resonant inelastic X-ray scattering setup
NEXAFS	Near-edge X-ray absorption fine structure
NMR	Nuclear magnetic resonance
P	Porphyrin (unsubstituted)
PDT	Photodynamic therapy
PO	Pyridone
RIXS	Resonant inelastic X-ray scattering
RNA	Ribonucleic acid
RSA	Restricted subspace approximation
SASE	Self-amplified spontaneous emission
SCF	Self-consistent field method
SGM	Spherical grating monochromator
TCPP	5,10,15,20-Tetrakis(4-carboxyphenyl)porphyrin
TD	Time-dependent
TP	Transition potential
TPP	5,10,15,20-Tetraphenylporphyrin
UE	Elliptical undulator
UV	Ultraviolet
VIS	Visible

Contents

1 Introduction

This thesis concentrates on the electronic structure variations of the pyridone and porphyrin groups of molecules. A fundamental understanding of the electronic states, their occupancies and influencing factors is of physical, biological, and chemical interest. The proper description of the interactions between electrons, atomic nuclei, and photons touches upon the core of quantum mechanics and hence modern physics. Especially porphyrins are promising building blocks for molecular electronics [158] and organic semiconductors [28]. These technologies have the potential for the further miniaturization of electronic devices and the utilization of quantum effects. The possibility to use chemical bulk production for their manufacturing promises atomic precision and tunability, as well as cost-efficiency. Considering the biological functions of pyridones and porphyrins, a fundamental understanding of the electronic structure and its parameters helps to comprehend natural processes such as photosynthesis, oxygen transport, storage of genetic information, or the cause and pathology of related diseases [157,143,96]. This knowledge can be applied, e.g. in the development of artificial photosynthesis [110,52] or medical treatment [14,134,92] by tailoring the molecular structure of bio-inspired compounds. The common denominator of all molecules, which are investigated in this thesis as well as their biologically relevant derivatives, is their aromatic character.

Aromaticity is a quantum-mechanical property with global intramolecular effects up to the mesoscopic scale [69]. The term aromatic stems from the odor of the first compounds of this class of molecules which were investigated in the 19th century [152]. While many of these molecules do not exhibit a distinctive aroma, they all show characteristic absorption bands which shift with increasing size from the ultraviolet (UV) to the visible (VIS) range causing grass to be green and blood to be red [51] – in most of the cases. The green blood of some worms [40] demonstrates that it is not the metal center of the oxygen transport complex, but the porphyrin ligand, which is responsible for the color. Besides their optical properties, aromatic molecules are characterized by a high thermodynamic stability and a low chemical

reactivity[69], giving rise to their wide applicability.

The basis for the optical appearance, the high stability, and all other molecular properties leading to the diversified functions of pyridones, porphyrins, and their derivatives is the electronic structure[25]. All these molecules have a highly delocalized π electron system in common, which is usually the result of the planar geometry of these cyclic species with resonance structures of alternating single and double bonds. In benzene (C_6H_6) – the prototypical aromatic molecule – the charge is equally distributed over all carbon atoms. The introduction of a heteroatom like nitrogen unbalances the electron density giving rise to chemical reactions, such as proton transfer and complex formation of pyridine (C_5H_5N), pyrrole (C_4H_4NH), as well as their investigated derivatives[44]. Peripheral substitution of the aromatic center leads to further modifications of the electronic structure depending on the position and orientation of specific groups (isomerism). The resulting molecular structure is further modified by external influences, i.e. interactions with a solvent (solvation) or UV/VIS photons. The latter can be treated as a major perturbation raising the system to excited states of different multiplicities, molecular geometries, and potential energy surfaces compared to the ground state. The influence of all these internal constitutional and external effects in the form of hydrogen bonding and optical excitation are addressed in this thesis.

X-ray spectroscopy has been shown to be ideally suited to monitor the electronic structure as a function of the above-mentioned perturbations[49,31,68]. The unique feature of this toolbox is the element selectivity, hence the methods allow to probe widespread state and charge differences locally – in this work at the nitrogen heteroatoms. These were chosen due to their role to enable chemical activity and their predominance in the aromatic moieties of biomolecules compared to other heteroatoms. The site selectiveness of nitrogen K-edge spectroscopy is a result of the excitation of the localized 1s electrons. By inducing transition to bound states and observing the absorption and subsequent emission of X-rays, information is obtained on the unoccupied and occupied manifold of valence states, respectively. In detail, X-ray absorption spectroscopy in the energy region of, but mainly below the ionization potential – also known as near-edge X-ray absorption fine structure (NEXAFS)[139] — is applied in this thesis; as well as resonant inelastic X-ray scattering (RIXS)[46] – describing the fluorescence caused by the absorption in the same energy window. Thereby, the influence of complexation, isomerism, solvation, and UV/VIS excitation on the electronic levels and their occupation close to the Fermi level is determined – revealing a global response to local constitutional changes and for the class of molecules relevant external perturbations.

In publication I the interaction of the electronic and solvation structure is studied on the example of pyridine and pyridone isomers (POs), in which one of the hydrogen atoms of pyridine is substituted by a hydroxyl group ($-$OH). The proton transfer between these POs and their hydroxypyridines (HP) counterparts – in which the nitrogen site is protonated instead of the oxygen one – is a prototypical example for tautomerism[137] and of biological interest due to the close relationship with vitamin B_6[99,140] and nucleobases[100]. Independent of the distance between the oxygen and nitrogen moieties, the HP tautomers are dominating in the gas phase. However, in aqueous solution, the PO tautomers are dominating or present in equal proportion depending on the substitution position. The analysis of the NEXAFS reveals that the three orders of magnitude difference of the tautomeric constant[74,11] and also acidity[1,8] upon hydration is a result of the internal degree of charge delocalized onto the substituent as well as the steric hindrance or enhancement of solvation in the PO isomers.

In 3PO the substituent is least conjugated, leading to a 1:1 mixture with 3HP – even though 3PO is highly stabilized by hydrogen bonding with the solvent [10]. It has been a long-standing chemical problem to obtain individual information on the molecular structure of each species in a tautomeric mixture. In publication II, the utilization of the chemical selectivity and scattering anisotropy of RIXS [45] to disentangle spectral features of such mixtures is generally proposed and exemplified by an aqueous 3HP/3PO solution. It is established that the polarization of the occupied orbitals is inverted between the tautomers: 3HP shows a higher charge density at the oxygen site in accordance with the higher electronegativity and is therefore dominating in the gas phase, whereas the orbital rehybridization upon hydration enhances the favorability of 3PO.

Compared to the rather small six π electron systems considered so far, the aromatic porphyrin macrocycle – of at least 18 π electrons which are distributed over four pyrrole moieties and methine (−CH=) bridges – shows a low solvent dependency [49]. On the other hand, the incorporation of a metal ion forming coordinate bonds to each pyrrole nitrogen has severe effects on the electronic structure. Publication III identifies the porphyrin center as a regulator for metal-ligand covalency and π hybridization to outer substituents by NEXAFS spectroscopy. It becomes clear why magnesium is used in natural photosynthesis [73], while zinc porphyrin is better suited for the technical imitation [148]. The maximum charge delocalization between the metal center and porphyrin ligand is established for transition metals, giving rise to the natural occurrence of iron porphyrins for oxygen transport in blood [71] and the application of copper porphyrin derivatives for catalysis, in pharmaceuticals, as well as in the food industry [43,22,123].

The natural precursor of metal porphyrins, the so-called free base form with two protons in the center, is studied by laser pump – X-ray probe spectroscopy in publication IV. The time-dependent NEXAFS is used to uncover the unusual deactivation path that makes this species an efficient photosensitizer for singlet oxygen generation [18] and a promising candidate for organic photovoltaics [54]. By direct observation of the frontier orbitals, the question of the present excited state electronic configurations is answered. In addition, the competition between stabilization by the conservation of angular momenta and vibronic relaxation is established to govern the de-excitation in this chromophore.

Besides the physical insights into biochemical processes, this thesis is characterized by advancements in experimental and theoretical methodologies. For example, the recently proposed restricted subspace approximation [150] for the efficient calculation of RIXS spectra is applied to study solvation effects on the electronic structure – not only statically but also in combination with molecular dynamics simulations mimicking ambient conditions. In the course of this thesis, the restricted subspace approximation is also adapted to NEXAFS spectrum simulation of optically excited states.

For the acquisition of the corresponding experimental laser pump – X-ray probe data, the state-of-the-art nmTransmission NEXAFS endstation has been used. The RIXS data has been acquired at the high-transmission EDAX spectrometer, which has been permanently installed and commissioned at the high-flux beamline UE49-SGM (Bessy II, Berlin) as part of this thesis. Additionally, the high-resolution spectrometers Heisenberg RIXS (hRIXS) and momentum and energy transfer RIXS (METRIXS) have been initially commissioned and optimized regarding data acquisition and analysis. Both setups will be able to gain access to the potential energy surfaces inter alia of bio-inspired aromatic molecules in the near future.

2

Physical aromatic chemistry

The molecular structure of aromatic molecules, giving rise to their unique features, is governed by the principles of quantum mechanics. As aromaticity – mainly in the form of benzene – was one of the first problems studied by the emerging chemical physics in the first half of the 20$^{\text{th}}$ century, the following approaches to describe the electronic structure not only serve as the theoretical foundation of this thesis but also mirror the developments in this scientific field: valence-bond theory, Hückel molecular orbital theory and its further developments culminating in modern computational methods[86]. At the end of this chapter, the influences of hydrogen bonding and photoexcitation on the chemical structure of aromatic biomolecules are discussed.

2.1 Electronic structure

The quantum mechanical description of matter is based on the Schrödinger equation. The time-independent form was published in 1926[131] and relates the wave function of a system (Ψ) to its energy (E).

$$\hat{H}\Psi = E\Psi \tag{2.1}$$

$\hat{H}$ denotes the Hamiltonian operator which evaluates the kinetic and potential energy of the system.

The solution of the Schrödinger equation for the hydrogen atom yields three quantities, which define the state of the electron: the principal (n), the azimuthal (l), and the magnetic (m_l) quantum number[5]. Based on these quantum numbers the single-electron wave functions – or orbitals – of all elements are classified. For example, the carbon and nitrogen $2p_z$ atomic orbitals, which are the origin of aromaticity, correspond to $n = 2$, $l = 1$, and $m_l = 0$.

Already one year before the Schrödinger equation was published, Pauli postulated a set of four quantum numbers, out of which at least one has to be different between any two electrons of a single atom.

Shortly after, the additional quantum number was interpreted as intrinsic angular momentum (spin)[147]. As a consequence, chemical bonds are described by pairs of electrons with antiparallel spin in one or two overlapping orbitals.

The study of molecular systems solely based on the Schrödinger equation is impossible since no analytical solution exists even for the smallest molecule (H_2^+), as it consists of three particles[4]. Therefore approximations need to be applied out of which the one by Born & Oppenheimer is used in virtually all theories of molecular structure. Since atomic nuclei are much heavier than electrons, the latter adapt to positional changes of the nuclei on a fast timescale. Therefore the Schrödinger equation of the electronic system can be solved with fixed nuclei positions yielding the electronic structure for that geometry. The optimization of the nuclei positions in order to minimize the potential energy yields the equilibrium structure. The representation of the molecular energy as a function of bond lengths and angles is referred to as potential energy surface and allows to predict the course of chemical reactions[4].

Consequently, the concepts of electronic structure and potential energy surfaces are the result of the Born-Oppenheimer approximation. The limitation of this approach is that the coupling of electronic and nuclear (vibrational) motion is neglected. In publication IV, it is exemplarily shown that even for molecules where this vibronic coupling is essential for the relaxation after photoexcitation, the evaluation of the electronic structure at the equilibrium geometries of the intermediate states is in good agreement with the experimental findings.

2.2 Valence-bond theory

Valence-bond theory provides a rather intuitive quantum mechanical description of chemical bonds, as they are treated as paired electrons similar to the common representation in Lewis structures. This theory is therefore used in this thesis for the qualitative description of electronic structure variations upon constitutional modifications. The following presentation of this theory is based on Atkins et al., but focuses on the prominent role of benzene as a prototypical aromatic molecule.

In valence-bond theory, a covalent bond is formed by two electrons, which remain in the atomic orbitals of separate atoms (A, B) while pairing their spins. The unnormalized wave function of the two electrons with position vector $\vec{r}_1$ and $\vec{r}_2$ is given by

$$\Psi(\vec{r}_1, \vec{r}_2) = \psi_A(\vec{r}_1)\psi_B(\vec{r}_2) \pm \psi_A(\vec{r}_2)\psi_B(\vec{r}_1). \tag{2.2}$$

The linear combination, which is a result of the indistinguishability of electrons, allows interference of the two wave functions. In the $+$ case, this interference is constructive, which enhances the electron density in the internuclear region and lowers the energy of this configuration.

To describe the electronic structure of benzene (Fig. 2.1a), the concept of orbital hybridization needs to be introduced. While the ground state configuration of a carbon atom ($1s^2 2s^2 2p_x^1 2p_y^1$) provides only two unpaired electrons, the notional excitation (promotion) $2s \rightarrow 2p_z$ gives rise to the capability of carbon to form four bonds. In addition, the inequality of the s and up to three p orbitals can be lifted by interference between these orbitals yielding up to four hybrid orbitals which take the maximum angle between each other. In aromatic molecules, two p orbitals (e.g. $2p_x$, $2p_y$) participate in the hybridization forming three hybrid orbitals pointing to each corner of a triangle, of which the surface is perpendicular

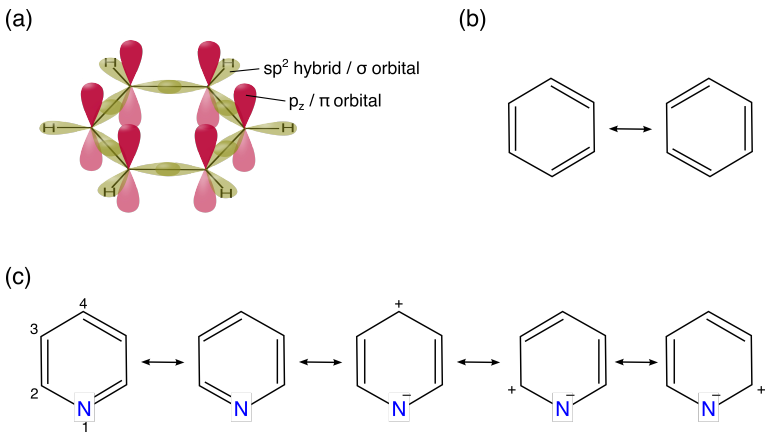

Figure 2.1: a) Valence orbitals of carbon in benzene according to valence-bond theory. b) Benzene resonance structures. c) Pyridine substitution positions and resonance structures.

to the non-hybridized p (e.g. $2p_z$) orbital. The geometry of these four orbitals gives rise to the planar structure of aromatic molecules. In this context, orbitals are typically classified by their symmetry with respect to the molecular plane into σ (symmetric) and π (anti-symmetric) orbitals[86].

The full agreement of the 120° bond angle in the benzene hexagon with the angle between the hybridized orbitals is suggestive of the high stability of this molecule. However, the main factor for the low reactivity of benzene is the delocalization of the six electrons in the π orbitals. This is represented in valence-bond theory by the concept of resonance (Fig. 2.1b). Therein, the total electronic wave function is improved and the corresponding ground state energy lowered by the superposition of multiple wave functions in the same molecular geometry, e.g.

$$\Psi = \Psi(\hexagon) + \Psi(\hexagon). \tag{2.3}$$

The combination of these resonance structures accounts for the equal bond length in benzene in contrast to alternating longer C−C and shorter C=C bonds. The equivalence of all bond lengths is characteristic for aromatic systems and hence a possible measure to quantify the degree of aromaticity[80,81].

For pyridine, where a carbon atom of benzene is replaced by a more electronegative nitrogen atom, ionic resonance structures gain importance, which are shown in Figure 2.1c. They suggest a reduction of the electron density at the carbon atoms next to the nitrogen atom (2 in Fig. 2.1c) and on the opposite side of the ring (4 in Fig. 2.1c). This observation is related to the functionality of three pyridine derivatives commonly referred to as vitamin B_6. In all of these molecules, a hydroxyl group (−OH) substitutes the hydrogen atom at the intermediate position (3 in Fig. 2.1c). The particularity of this isomer in the vitamin B_6 core moiety 3HP is fathomed in publication I. While valence-bond theory is useful for predictions of substituent effects – not only in the case of vitamin B_6 – the concept of molecular orbitals is usually employed for the quantitative description of the chemical structure.

2.3 Hückel molecular orbital model

Hückel's description of aromaticity can be seen as the cornerstone of molecular orbital theory[86]. It is a precursor of the computational methods used in this thesis, which will be introduced in the next section.

In contrast to a valence-bond between two atomic orbitals, a molecular orbital can be distributed over all atoms in a molecule. To reduce the complexity and enable the solution of the Schrödinger equation (2.1) for polyatomic compounds, molecular orbitals are approximated by linear combinations of atomic orbitals (ψ_r)[5]

$$\Psi = \sum_r c_r \psi_r. \tag{2.4}$$

All modern electronic structure calculations are additionally based on the variational principle, stating that the expectation value of the Hamiltonian (E) for any wave function is always larger or equal to the true energy (E_0). Including the normalization $\int \Psi^\star \Psi d\tau$ of the trial wave function (Ψ), the variational principle can be expressed by[4]

$$E_0 \leq E = \frac{\int \Psi^\star \hat{H} \Psi d\tau}{\int \Psi^\star \Psi d\tau}. \tag{2.5}$$

The substitution of equation 2.4 into 2.5 and the definitions of the resonance integral $H_{rs} = \int \psi_r \hat{H} \psi_s d\tau$ and overlap integral $S_{rs} = \int \psi_r \psi_s d\tau$ of two atomic orbitals ψ_r and ψ_s yields[44,5]

$$E = \frac{\sum_r \sum_s c_r^\star c_s H_{rs}}{\sum_r \sum_s c_r^\star c_s S_{rs}}. \tag{2.6}$$

To obtain values for the coefficients at the energy minimum of the given set of orbitals, the partial derivatives $\frac{\partial E}{\partial c_i}$ need to be zero. The resulting secular equations are usually transformed into their matrix representation, which contains the resonance integrals in the Hamiltonian matrix $\mathbf{H}$, the overlap integrals in $\mathbf{S}$, the coefficients of atomic orbitals in $\mathbf{c}$, and the energies in the diagonal matrix $\mathbf{E}$[4].

$$0 = (\mathbf{H} - \mathbf{ES})\mathbf{c} \tag{2.7}$$

From algebra it is known that a non-trivial solution for the coefficients in $\mathbf{c}$ only exist, if the secular determinant vanishes[44].

$$0 = |\mathbf{H} - \mathbf{ES}| \tag{2.8}$$

In the specific case of benzene, the solution of equation 2.8 requires 42 electrons to be described (and 12 nuclei if the Born-Oppenheimer approximation would not be applied). The Hückel approximation helps to simplify the procedure, by considering only the six electrons of the unhybridized C 2p orbitals (see section 2.2), which form the delocalized π system[44]. Additionally, the overlap integrals are assumed to be negligible for atomic orbitals of different atoms ($S_{rs} = 0$ for $r \neq s$). Since the overlap of an orbital with itself is one ($S_{rr} = 1$), the overlap matrix turns into a unit matrix ($\mathbf{S} = \mathbf{1}$) and is neglected within the Hückel approximation. Furthermore, each Coulomb integral (H_{rr}), which is related to the energy of an electron occupying ψ_r, is set to α. The remaining resonance integrals H_{rs} are set to β for neighboring atoms and otherwise to zero[4]. If r and s are integers denoting one of the six C $2p_z$ orbitals in benzene

the determinant is modified as follows.

$$0 = \begin{vmatrix} H_{11} - ES_{11} & \dots & H_{16} - ES_{16} \\ H_{21} - ES_{21} & \dots & H_{26} - ES_{26} \\ H_{31} - ES_{31} & \dots & H_{36} - ES_{36} \\ H_{41} - ES_{41} & \dots & H_{46} - ES_{46} \\ H_{51} - ES_{51} & \dots & H_{56} - ES_{56} \\ H_{61} - ES_{61} & \dots & H_{66} - ES_{66} \end{vmatrix} \overset{\text{Hückel}}{\approx} \begin{vmatrix} \alpha - E & \beta & 0 & 0 & 0 & \beta \\ \beta & \alpha - E & \beta & 0 & 0 & 0 \\ 0 & \beta & \alpha - E & \beta & 0 & 0 \\ 0 & 0 & \beta & \alpha - E & \beta & 0 \\ 0 & 0 & 0 & \beta & \alpha - E & \beta \\ \beta & 0 & 0 & 0 & \beta & \alpha - E \end{vmatrix} \tag{2.9}$$

The simplified determinant yields six energy levels corresponding to six molecular orbitals, which are denoted (E) in the following. According to the aufbau principle, the benzene configuration of frontier orbitals is $(\alpha+2\beta)^2\,(\alpha+1\beta)^2\,(\alpha+1\beta)^2\,(\alpha-1\beta)^0\,(\alpha-1\beta)^0\,(\alpha-2\beta)^0$, where both α and β are negative[4]. The aromatic stability stems from the occupation of all bonding ($E < \alpha$) and neither non-bonding ($E = \alpha$) nor anti-bonding ($E > \alpha$) molecular orbitals[44].

The solution for benzene has been generalized to any C_NH_N monocycle by Hückel. The energy of the π orbitals is given by[64,65]

$$E = \alpha + 2\beta\cos\left(\frac{2\pi}{N}k\right) \quad \text{with} \begin{cases} N \text{ is even:} & k = 0, \pm1, \pm2, \dots, +\frac{N}{2}. \\ N \text{ is odd:} & k = 0, \pm1, \pm2, \dots, \pm\frac{N-1}{2}. \end{cases} \tag{2.10}$$

This equation has two important implications for the molecules considered in this thesis:

Firstly, full aromatic stabilization is only reached for $N\,\pi$ electrons, where $N = 4n + 2$ with $n = 1, 2, 3\dots$. This is because for an odd N, not all bonding orbitals can be doubly occupied, while all antibonding orbitals are unoccupied. The delocalization energy[4] is therefore reduced. If N is even, the considered molecular orbitals consist of energetically symmetric pairs viz. $\alpha \pm b\beta$ with $0 \leq b \leq 2$. For $N = 2, 6, 10, \dots$ exactly all bonding π orbitals are occupied. However, for $N = 4, 8, 12, \dots$ k can have the value of $\frac{N}{4}$, in which case two singly occupied orbitals of non-bonding character are expected ($\alpha + 2\beta\cos(\frac{2\pi}{N}\frac{N}{4}) = \alpha$), which do not contribute to the stabilization of the respective molecule. Thus, monocyclic systems with $4n + 2$ and $4n$ π electrons are considered to be aromatic and anti-aromatic respectively.

Secondly, the energy gap between the highest occupied molecular orbital (HOMO) and the lowest unoccupied molecular orbital (LUMO) is continuously reduced for an increasing value of n, since $\alpha \pm 2\beta$ are always the highest and lowest π orbitals while more and more molecular orbitals with intermediate energies are formed[44]. This has important implications on the photophysical properties of aromatic molecules, as discussed in section 2.5.2.

As shown in Figure 2.2, pyridine, pyrrole and the porphyrin macrocycle contain an aromatic system of six or 18 π electrons and are therefore expected to exhibit a similar chemical stabilization as benzene. However, the higher electronegativity of nitrogen unbalances the charge distribution in the molecule (as discussed in section 2.2). In the Hückel model this effect can be expressed by an increase of the Coulomb integral $H_{\text{NN}} = \alpha + b \cdot \beta$ ($b_{\text{Pyridine}} \approx 0.5$, $b_{\text{Pyrrole}} \approx 1.5$)[44].

As a result of the charge imbalance, these heterocyclic systems participate in proton transfer and complex formation reactions, which are the foundation of their biological functions. The significant role of

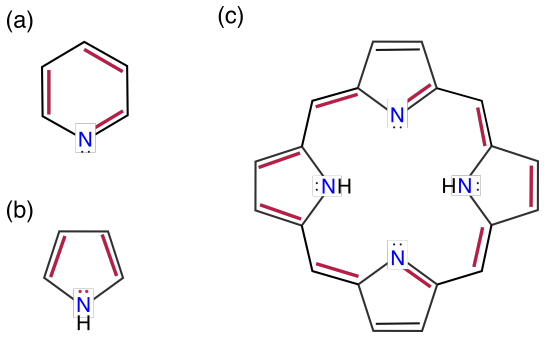

Figure 2.2: Lewis structures with highlighted aromatic electron pairs (red): a) pyridine, b) pyrrole, and c) porphyrin.

aromaticity in nature can be explained by the high stability of these molecules according to the Hückel model. While the underlying approximations facilitate the understanding of aromaticity[86], for the precise analysis of the electronic structure (as provided by all publications of this thesis) modern computational methods are superior.

2.4 Computational methods

This section focuses on Hartree-Fock-based methods and density functional theory according to the description of Atkins & Friedman if not stated otherwise. Both approaches are employed in this thesis to model the electronic structure of bio-inspired aromatic molecules.

The Hartree-Fock (HF) method[56], which is the basis for most *ab initio* calculations for small molecules is based on the variational principle (equation 2.5). The relativistic electron spin is introduced into the classical Schrödinger equation (2.1) by multiplying the wave function of each electron with a spin function. The resulting spin-orbital is denoted $\varphi_u(v)$ in the following, where u and v indicate the individual spin-orbital and electron, respectively. In order to ensure the Pauli principle, which states (more generally than the exclusion principle in section 2.1) that the total wave function must be antisymmetric upon interchanging two fermions, the wave function of the system is typically expressed as a Slater determinant

$$\Psi = (N!)^{-\frac{1}{2}} \begin{vmatrix} \varphi_a(1) & \dots & \varphi_z(1) \\ \vdots & \vdots & \vdots \\ \varphi_a(N) & \dots & \varphi_z(N) \end{vmatrix}, \tag{2.11}$$

where N denotes the number of electrons and $a, \dots z$ index the same number of spin-orbitals.

When neglecting the spin polarization, which is valid for a system of fully doubly occupied orbitals, the HF equation of an individual electron v in the averaged field of the other $N-1$ electrons reads

$$f_v \psi_u(v) = \varepsilon_u \psi_u(v) \tag{2.12}$$

Therein, ε_u denotes the energy of the orbital u and f_v is the Fock operator. f_v includes the one-electron Hamiltonian of the electron v, the Coulomb repulsion between the electrons (Coulomb operator), and the energy modification by spin correlation as a consequence of the Pauli principle (exchange operator).

Since the solution of the HF equation (2.12) for one electron demands the knowledge of the $N-1$ other orbitals, the calculation starts with approximated wave functions. These orbitals are iteratively

optimized by solving (2.12) for all electrons yielding optimized wave functions and new averaged potentials. The iteration is stopped when the orbitals do not change more than a certain threshold. In other words, this procedure yields self-consistent orbitals and is therefore also referred to as the self-consistent field method (SCF).

In order to apply the HF-SCF procedure to molecular systems, the computational complexity is reduced by defining spatial wave functions as a linear combination of basis functions analogous to the linear combination of atomic orbitals (equation 2.4). The HF equivalents of the matrix problem in equation 2.7 are known as Roothaan equations. As in equation 2.8, the energies of the iteratively optimized orbitals in HF-SCF can be calculated from the secular determinant. The accuracy of the computational results and the computation time depend on the size of the selected basis set.

Even with an infinite set of basis functions, the inherent neglection of instantaneous electron-electron interactions that are averaged in the HF method cannot be overcome. These electron correlations are accounted for in post-HF methods such as perturbation theory or configuration interaction (CI) calculations. In the latter, not a single Slater determinant is used for the wave function of the electronic system, but a linear combination of multiple ones, representing excited states in which not all energetically low spin-orbitals are occupied.

In the complete active space self-consistent field method (CASSCF)[118] only those wave functions are linearly combined, in which a set of inactive orbitals is always occupied and a set of virtual orbitals is never occupied. The considered Slater determinants arise from all excitations within the remaining active orbitals. In contrast to simpler CI calculations, both the expansion coefficients defining the single orbitals from basis functions and those determining the total wave function from the Slater determinants are optimized during a CASSCF calculation.

With today's computational power, CASSCF calculation can be carried out for medium-sized molecules like pyridine derivatives (HP/PO in publication I), but they are computationally too expensive for large molecules such as porphyrins (publication III, IV) or a large number of calculations for different molecular geometries (publication II). In this case density functional theory (DFT) is applied.

DFT is based on the theoretical foundation by Hohenberg & Kohn and the practical implementation of Kohn & Sham (KS), who have shown how the energy of a ground-state N-electron system can be obtained from the electron density

$$\rho(\vec{r}) = \sum_{j=1}^{N} |\psi_j^{\mathrm{KS}}(\vec{r})|^2. \tag{2.13}$$

For optimizing a trial electron density, the KS equations are used. In these modified Schrödinger equations, the KS Hamiltonian depends on the electron density and the solution yields the KS orbitals $\psi_j^{\mathrm{KS}}(\vec{r})$. These orbitals are the basis for a new electron density, which is then again used to solve the KS equations. This iterative procedure is carried out until convergence is reached[4].

The drawback of this approach is that the KS Hamiltonian is not completely known. While the evaluation of the kinetic, potential, and coulomb energy is established, the exchange and correlation energy can only be approximated. Two exchange-correlation functional families are used in this thesis, PBE/ PBE0 for *ab initio* and BLYP/ B3LYP/ BHandHLYP/ CAM-B3LYP for semi-empirical calculations. The members of these families differ in terms of exact HF exchange.

In publication III, the performance of different exchange-correlation functionals is a subject of discussion. In short, pure functionals (such as BLYP [12,91]) describe the electronic structure of the aromatic porphyrin macrocycle well. However, if the focus lies on the porphyrin as a ligand of a metal complex the incorporation of exact HF exchange is demanded (as provided by BHandHLYP [13]) [24,16]. In range separated functionals (e.g. CAM-B3LYP [159]), the amount of HF exchange is no longer constant but increases with distance. While this group has been proposed for aromatic molecules in different fields [17,70], the agreement with X-ray spectroscopic data is rather poor (more information on the used time-depend DFT are provided in section 3.2.4). The selection and development of exchange-correlation functionals is an open scientific task that is not limited to the description of the electronic properties of aromatic molecules.

2.5 Influencing factors on biochemical systems

The electronic structure of bio-inspired aromatic molecules depends on multiple factors, out of which the chemical composition is most important. As mentioned in section 2.3, the nitrogen heteroatom introduces reactivity into the stable benzene ring, giving rise to substitution and complex formation reactions. Both are addressed in the publications presented in this thesis. Additionally, the effect of external influences – such as hydrogen bonding by the solvent or optical excitations – on the electronic structure are assessed. The theoretical description of these influencing factors is summarized in this section.

2.5.1 Hydrogen bonding

Hydrogen bonding is the dominant solvent-induced effect in all publications included in this thesis and biologically relevant for the three-dimensional order of nucleic acids and proteins [3].

The computational evaluation of hydrogen bonding is typically achieved by molecular dynamics (MD) simulations. Thereby, the temporal evolution of the arrangement of molecules at a defined temperature, corresponding to the mean kinetic energy, can be followed [4]. Classical force fields are used at least for solvent molecules as the trajectory of whole atoms largely obeys Newton's laws of motion: Bending and stretching of bonds are modeled by oscillators; electrostatic and van der Waals interactions by Coulomb and Lennard-Jones potentials, respectively [62].

Out of the MD simulations the average hydrogen bond number, length, and angle can be determined for each molecular site. Additionally, general characteristics of the solvation such as radial distribution functions and solvent densities are obtained. This information can be further used to create minimally-solvated models for a full quantum mechanical treatment (as shown in publication I). In this case, the description of the environment beyond the first solvation shell becomes important.

The conductor-like polarizable continuum model (CPCM) is a tool for such an implicit treatment of solvation, which is used in all publications of this thesis. In the CPCM approach, the solute is enclosed in a molecule-shaped cavity, which separates it from the solvent continuum with a constant dielectricity. In an infinitely polar solvent, the apparent polarization charges on the surface of this cavity completely cancel out the electrostatic potential of the solute. In a real solvent this effect is reduced according to the dielectric constant. The inclusion of the resulting approximated charges in the Fock operator or KS Hamiltonian allow an efficient treatment of electrostatic solvation effects in the previously described

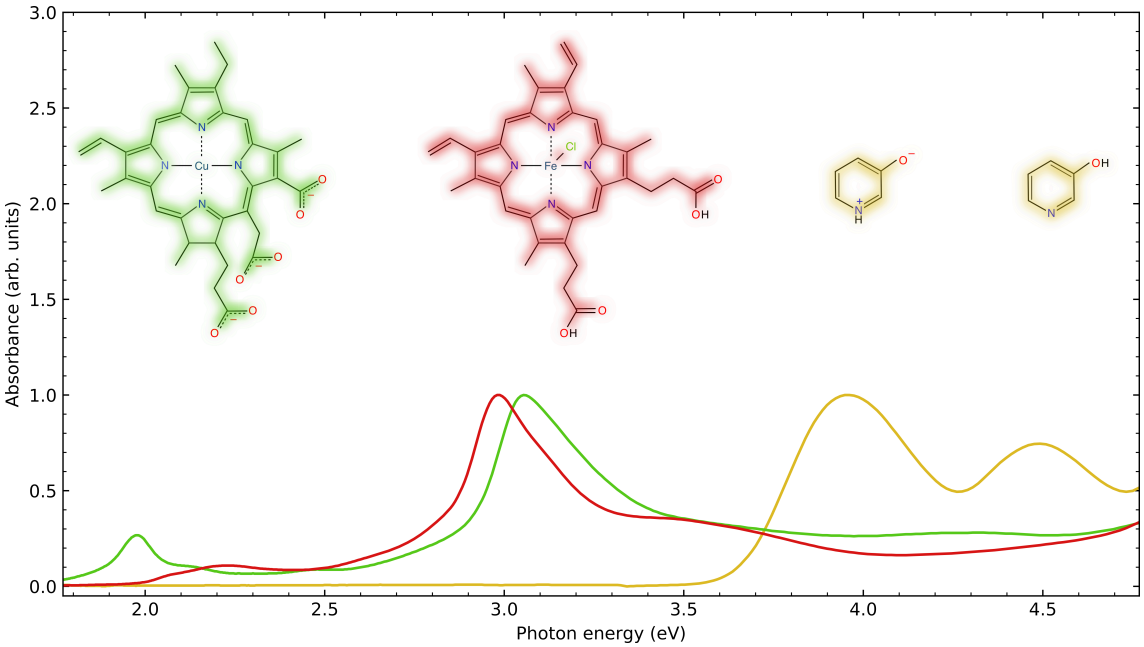

Figure 2.3: UV/VIS spectra [energy of most intense feature] of chlorophyllin [3.1 eV], hemin [3.0 eV], as well as the 3PO [4.0 eV] and 3HP [4.5 eV – assignment based on Metzler & Snell] tautomers.

computational methods[9,20].

2.5.2 Optical excitation

As optical spectroscopy is a widely used tool for the characterization of aromatic compounds, this thesis builds upon the concepts developed for the interpretation of UV/VIS spectra of the investigated molecules. Figure 2.3 shows the optical absorption spectra of chlorophyllin, hemin (chloride salt of the oxygen transport complex heme), as well as the 3HP and 3PO tautomers. As derived from the Hückel model (section 2.3) the HOMO–LUMO gap of aromatic molecules decreases with the number of π electrons. Therefore the corresponding absorption band moves to higher energies with decreasing aromatic ring size[146,77].

The alternative – but closely related[121] – free electron ring model provides a more direct explanation of the shifts and also the splitting of the porphyrin (hemin) and chlorin (chlorophyllin) bands. While the approximation of aromatic molecules by a particle on a ring was initially proposed by Schmidt[86], the application to porphyrins and derivatives is the life's work of Gouterman[48].

The approach can be motivated by a persistent ring current in an external magnetic field[112,94,93,128], which is another defining property of aromatic systems[19]. The Schrödinger equation (2.1) for an electron (with mass m_e) on a ring with radius r yields the energy E_{m_l} dependent on the quantum number m_l[4]

$$E_{m_l} = \frac{\hbar^2 {m_l}^2}{2 m_e r^2} \qquad \text{with } m_l = 0, \pm 1, \pm 2, \dots . \tag{2.14}$$

Thus, the HOMO-LUMO gap corresponding to the energetically lowest absorption feature is in this simple model expected to be indirectly proportional to the square of the radius $E_{m_l+1} - E_{m_l} \propto \frac{2m_l+1}{r^2}$.

Considering the 18 π electron ring of porphyrins, the ground state configuration can be expressed by $(0)^2\ (\pm1)^4\ (\pm2)^4\ (\pm3)^4\ (\pm4)^4\ (\pm5)^0$, if (m_l) denotes the energetically lowest orbital or a pair of the

remaining, degenerate ones. The total angular momentum is $L_z = \sum m_l \hbar = 0$. Since the frontier orbitals consist of two degenerate pairs, the two lowest singlet excited states are dominated by configuration interactions leading to an average configuration of $(+4)^{1.5}(-4)^{1.5}(+5)^{0.5}(-5)^{0.5}$. The excited states differ by their total angular momentum of either $L_z = \pm 1\hbar$ or $L_z = \pm 9\hbar$. Following the considerations of Hund for atomic spectra[87], the $L_z = \pm 1\hbar$ state is high and the $L_z = \pm 9\hbar$ state low in energy. From the dipole selection rules*, it can be seen that the $\Delta L_z = \pm 1\hbar$ band is allowed, while the $\Delta L_z = \pm 9\hbar$ is forbidden[50].

In publication IV, this model is discussed in terms of the generation of singlet oxygen by photoexcited free base porphyrins, which have an absorption spectrum similar to hemin. When free base porphyrins accumulate in the body of patients with erythropoietic protoporphyria, who exhibit an inborn reduced activity of the enzyme which converts (free base) protoporphyrin IX to heme, the generation of singlet oxygen causes intense skin inflammation[143]. On the other hand, the cellular damage caused by the singlet oxygen formation of photoactivated free base porphyrins and derivatives is intentionally induced in the treatment of tumors[14,134] and other diseases[63,113,89] by photodynamic therapy (PDT). The benefit of these systems compared to other photosynthesizers such as 3HP[157] is their selectivity for tumor tissue and the absorption of light in the phototherapeutic window ($1.4 - 2.1$ eV)[7], where human tissue is most transparent.

The previously presented four-orbital model explains not only the porphyrin absorption bands and parts of the deactivation pathway, but also the difference to the chlorin derivatives with the popular representatives chlorophyll (Mg chlorin) and chlorophyllin (Cu chlorin – Fig. 2.3). Due to the reduction of one pyrrole ring, the chlorin frontier orbital can no longer be considered to be pairwise degenerate[51]. Therefore the concentration of intensity at the $\approx$ 3 eV feature is reduced, enabling photosynthetic plants to harness both blue and red light. In the words of Gouterman: "More poetically the model explains why 'grass is green and blood is red,' that is, the basic spectroscopic facts of porphyrins and related molecules."[51]

However, as highlighted in publication III, the Gouterman model is not sufficient to explain all chemical properties of porphyrins and derivatives, as it becomes immediately clear by the influence of different metal centers on the porphyrin functionality. This limitation is linked to the non-localized nature of optical spectroscopies. In this thesis the selectivity of X-rays is utilized, which enables inter alia to disentangle the individual chemical structure of the 3HP/3PO tautomers (publication II). The following chapter sheds light on the relevant X-ray spectroscopic tools for this thesis and their technical implementation.

*The basis for this selection rule along with the quantum mechanical description of light absorption is given in section 3.1.

3

Soft X-ray spectroscopy

Experimental access to the electronic structure, defining the chemical properties of matter, can be gained by different spectroscopic techniques. In this thesis, soft X-ray spectroscopy is applied to shed light on the local charge distribution and its response to external influences, due to its element and chemical state selectivity. In detail, near-edge X-ray absorption fine structure (NEXAFS) and resonant inelastic X-ray scattering (RIXS) are applied to bio-inspired aromatic molecules in solution. Besides an overview of these techniques, their practical implementation at a synchrotron light source is presented in this chapter.

3.1 Golden rule and dipole transition intensity

The macroscopic effects of absorption and resonant inelastic scattering in the soft X-ray regime, which are used in this thesis, can be described on the microscopic level of matter by the time-dependent Schrödinger equation [132]. While the concept of orbitals requires most of the previous equations to be based on wave functions, this chapter makes use of the Dirac notation, in which $|\alpha, t_0; t\rangle$ is the state ket of the system corresponding to the wave function $\Psi_\alpha(t)$ [125].

$$i\hbar\frac{\partial}{\partial t}|\alpha, t_0; t\rangle = \hat{H}|\alpha, t_0; t\rangle \tag{3.1}$$

By the development of time-dependent perturbation theory, Dirac derived the transition probability per unit time $w_{0\to[f]}$ from the initial state $|0\rangle$ to a number of final states $|f\rangle$, which reads to the second order [101]

$$w_{0\to[f]} = \frac{2\pi}{\hbar}\sum_f \left| \overbrace{\langle f|\hat{V}|0\rangle}^{\text{first order}} + \overbrace{\sum_i \frac{\langle f|\hat{V}|i\rangle\langle i|\hat{V}|0\rangle}{E_i - E_0 - \hbar\omega}}^{\text{second order}} \right|^2 \delta(E_f - E_0 - \hbar\omega + \hbar\omega'). \tag{3.2}$$

This equation was later termed "Golden Rule #2" by Fermi. In the simplest case of a constant perturbation (starting at $t = 0$), the terms including angular frequencies vanish $\omega = \omega' = 0$ [125]. Besides the time-independent initial and final eigenstates with the energy eigenvalues E_0 and E_f, a number of intermediate eigenstates $|i\rangle$ with the energy eigenvalues E_i are included in the second order term. The interaction operator $\hat{V}$ represents the time-dependent perturbation and is part of the otherwise time-independent Hamiltonian in equation 3.1. The δ function ensures energy conservation.

The generally dominating first order term of equation 3.2 can be used to describe the absorption of light exciting the system from the ground state $|0\rangle$ to a valence or core-excited state $|f\rangle$, which corresponds to the fundamental process of UV/VIS or NEXAFS spectroscopy, respectively. In this case the absorbed energy is represented by $\hbar\omega$. The second order term becomes important, if the incident radiation is in resonance $\hbar\omega \approx E_i - E_0$, similar to RIXS. When the denominator approaches 0, the second order term is dominating, describing a virtual excitation and decay as represented by the transition matrix elements $\langle i|\hat{V}|0\rangle$ and $\langle f|\hat{V}|i\rangle$. For energy conservation, the term $\hbar\omega'$ is needed, denoting the emitted energy. The derived expressions for the NEXAFS and RIXS cross-sections are discussed in detail in the following sections 3.2.1 and 3.3.2, respectively.

In the remaining part of this section, the meaning of the transition matrix elements is elucidated with a focus on interactions with soft X-rays. Analogous to the ground state description (section 2.1), only the electronic transitions are considered here, since they are assumed to occur much faster than the nuclear motion (Condon approximation) [139]. The interaction operator for either absorption or emission of a classical, monochromatic plane wave by N electrons can be expressed by [125]

$$\hat{V} = -\frac{e}{m_e\, c} \sum_{j=1}^{N} \overbrace{A_0 \underbrace{e^{\pm \mathrm{i}(\vec{k}\cdot\vec{r}_j)}}_{\approx 1}}^{\text{from plane wave}} \vec{\varepsilon}\cdot\hat{p}_j, \tag{3.3}$$

where e, m_e, and c are natural constants. A_0 represents the amplitude of the vector potential. $\vec{k}$ is the wave vector and $\vec{\varepsilon}$ is a unit vector indicating the polarization. $\hat{p}_j$ denotes the momentum operator of electron j.

Within the electric dipole approximation, the expansion of $e^{\pm \mathrm{i}(\vec{k}\cdot\vec{r}_j)} = 1 \pm \mathrm{i}(\vec{k}\cdot\vec{r}_j) + \ldots$ is truncated after the leading term so that the expression vanishes in the interaction operator. This simplification is justified if $\vec{k}\cdot\vec{r}_j \ll 1$, which is the case up to the soft X-ray regime. Here the product of the magnitude of the wave vector $|\vec{k}| \leq \frac{2\pi}{1\,\mathrm{nm}}$ and the spacial dimension of an atomic core orbital $|\vec{r}_j| \approx 0.01\,\mathrm{nm}$ [139] is still below 0.1, so that the approximation is valid.

The momentum operator $\hat{p}_j$ is typically transformed into the dipole operator $e\hat{r}_j$ to yield the dipole matrix element from the transition matrix element [101].

$$\begin{aligned} \left\langle \alpha' \middle| \hat{V} \middle| \alpha \right\rangle &\overset{\propto}{\approx} A_0 \omega \vec{e} \left\langle \alpha' \middle| \sum_{j=1}^{N} \hat{r}_j \middle| \alpha \right\rangle \\ &\overset{\propto}{\approx} A_0 \omega \vec{e} \left\langle \alpha'_1 \middle| \hat{r}_1 \middle| \alpha_1 \right\rangle \underbrace{\left\langle \alpha'_{N-1} \middle| \alpha_{N-1} \right\rangle}_{\approx 1} \end{aligned} \tag{3.4}$$

The factor ω corresponds to the energy being absorbed or emitted during the transition. When ignoring configuration interactions, the electronic state $|\alpha\rangle \in \{|0\rangle, |i\rangle, |f\rangle\}$ can be expressed by a single Slater determinant (equation 2.11).

The transition dipole moment can be further simplified by separating the matrix element of one excited electron (let it be $j = 1$) and that of the remaining $N - 1$ electrons (sudden approximation [139]) as shown in equation 3.4. In the commonly applied frozen-orbital approximation, it is assumed that the $N - 1$ passive orbitals are not modified by the transition of electron 1, so that $|\alpha'_{N-1}\rangle = |\alpha_{N-1}\rangle$ and the overlap integral vanishes [66].

An advantage of the applied approximations is that orbital energies can be defined as the difference between the energy of an incident photon and the kinetic energy of an ejected electron upon ionization.

$$E_\alpha = \hbar\omega - E_{\text{kin}} \tag{3.5}$$

This relation is known as Koopmans theorem [139]. It is of primary importance for photoelectron spectroscopy, but is also considered in publication I and III, since it is the reference for calculated Hartree-Fock orbital energies.

As discussed in these articles, the simple picture of a single excited-state configuration, in which only the state of one electron changes, is often not suitable for a quantitative description of the interaction of X-rays and molecules. Instead, relaxation in the core-excited state needs to be considered. Firstly, the reduced shielding of the atomic nucleus causes an attractive relaxation and polarization in the valence region. A first-order estimate is the equivalent core approximation, in which it is assumed that the response of the valence electrons to the core hole is similar to an increase of the nuclear charge by one. In the case of a N 1s excitation, this means that the excited nitrogen atom behaves largely like a ground state oxygen atom. Secondly, if the excited electron is not ejected, it causes a repulsive polarization of the valence electrons [106]. These effects need to be captured by the computational approaches to facilitate the interpretation of NEXAFS, RIXS, and other inner-shell spectroscopic data (as shown in the next sections).

For an understanding of the distinctive feature of soft X-ray spectroscopy, the simplified expression of the dipole matrix element within the frozen-orbital approximation (equation 3.4) is sufficient. While all statements up to this point were equally true for spectroscopic methods in the UV/VIS range, the local approximation is only applicable for the excitation of core electrons. Within this approximation, the initial state of the excited electron is described by an atomic orbital $|\alpha_1\rangle \approx |n, l, m_l\rangle$. While transitions to bound states, in general, populate molecular orbitals, one coefficient in the linear combination (equation 2.4) is often dominant, so that the final state can be approximated by an atomic orbital $|\alpha'_1\rangle \approx |n', l', m'_l\rangle$, too [97]. The possibility to probe the local electronic structure at defined atomic centers is the key asset of the spectroscopic techniques used in this thesis.

It can be mathematically shown that the transition intensity $|\langle n', l', m'_l|\hat{r}_1|n, l, m_l\rangle|^2$ is bigger than zero only if the quantum numbers of the involved orbitals (section 2.1) differ by $l' - l = \pm 1$ and $m'_l - m_l = \pm 1$ or 0 depending on the polarization of the radiation. To conserve angular momentum, the change in l is compensated by the absorption or emission of a photon with spin angular momentum $S_{\text{ph}} = 1$. Since the electron spin is not affected by the described transition in light atoms, it cannot

change. These restrictions are commonly referred to as dipole selection rules.

The latter rule is the reason for the long lifetime of triplet excited states (in molecules with a singlet ground state and no heavy atom), as they cannot decay without the spin-flip of an electron (see e.g. publication IV). Regarding the probe of the aromatic π system, being built from carbon and nitrogen 2p orbitals, the selection rule $l' - l = \pm 1$ suggests a high transition intensity for the excitation of 1s electrons, which makes K-edge spectroscopy ideally suited for this purpose. For related studies with a focus on the porphyrin and chlorin transition metal center, $L_{2,3}$-edge spectroscopy has been employed. Especially RIXS at this edge is beneficial, since it has been shown that the virtual two-step process allows the study of d$\rightarrow$ d excitations, which are dipole forbidden in UV/VIS absorption spectroscopy [141,78,85].

Overall, soft X-ray spectroscopies follow the same approximations as techniques in the UV/VIS regime. However, the excitation of localized core electrons yields an element-specific projection of the valence states and the nature of the transitions can allow final states, which are dipole forbidden for other spectroscopic techniques.

3.2 Near-edge X-ray absorption fine structure

NEXAFS focuses on the energetically lowest features of an X-ray absorption edge, where transitions of core electrons to bound states are dominating [139]. It is therefore used in publications I and III of this thesis to elucidate the local unoccupied density of states at the chemically relevant nitrogen sites of a series of pyridones and porphyrins. In publication IV a laser pump – NEXAFS probe scheme is used to follow the relaxation of a photo-excited free base porphyrin. Both for the static and transient measurements, the nmTransmission NEXAFS endstation [39] has been used, which allows a direct probe of the X-ray absorption cross-section of samples in solution.

3.2.1 Macroscopic and microscopic measurement quantities of absorption

The microscopic absorption cross-section $\sigma_{\text{Abs.}}$ is defined as the absorbed energy ($\hbar\omega$) per unit time divided by the energy flux of the incident radiation F_{ph} (which eliminates the $A_0\omega$ factors of equation 3.4)

$$\sigma_{\text{Abs.}} = \frac{\hbar\omega\, w_{0\rightarrow[f]}}{F_{\text{ph}}} \propto \sum_f \omega \left|\langle f|\vec{\varepsilon}\cdot\hat{r}|0\rangle\right|^2 \Delta(\omega_{0\rightarrow f} - \omega, \Gamma). \tag{3.6}$$

In comparison to the golden rule (equation 3.2), the absorption features have a non-zero broadening around $\omega_{0\rightarrow f} = (E_f - E_0)/\hbar$, as given by the Lorentzian function $\Delta(\Omega, \Gamma) = \Gamma/\pi(\Omega^2 + \Gamma^2)$. The half width at half maximum Γ is the result of the finite lifetime of the final – in this case core-excited – state. At the N K-edge it amounts to 65 meV [104] corresponding to $\approx$ 5 fs by the uncertainty principle [139]. If the nuclear part of the initial ($|0\rangle$) and final state ($|f\rangle$) were approximated to be constant, vibrational motion and solvation of molecular samples would need to be modeled by further broadening. The exact treatment of these effects is described in publication II.

The oscillator strength, which is proportional to the area under a single experimental absorption feature, is defined by [149,125]

$$F_{0\rightarrow f} = \frac{2m_e\omega}{\hbar} \left|\langle f|\vec{\varepsilon}\cdot\hat{r}|0\rangle\right|^2. \tag{3.7}$$

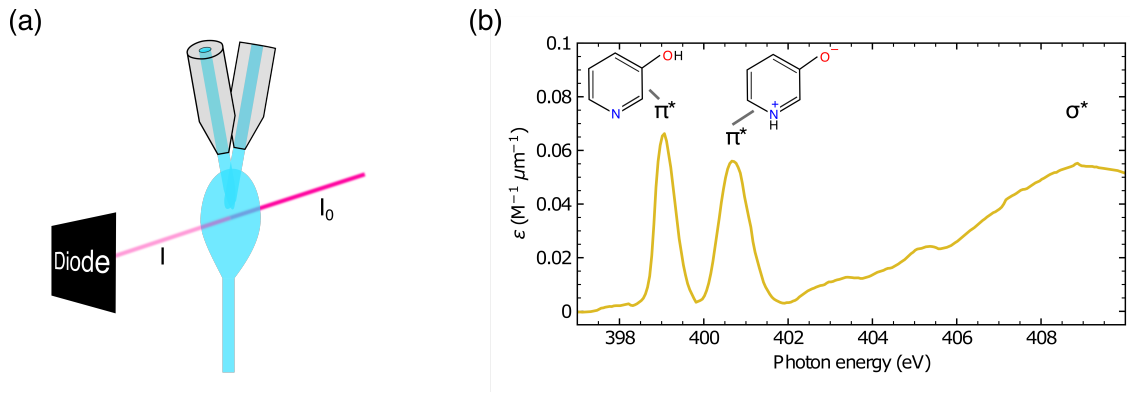

Figure 3.1: a) Measurement scheme of the nmTransmission NEXAFS endstation. b) N K-edge NEXAFS spectrum of 3-hydroxypyridine/3-pyridone (3HP/3PO) tautomers in aqueous solution.

The corresponding macroscopic quantity is the extinction coefficient ε, which relates to the incident (I_0) and transmitted intensity (I) of the sample according to Beer–Lambert's law

$$\varepsilon = \frac{\log_{10}\left(\frac{I_0}{I}\right)}{c \cdot l}. \tag{3.8}$$

The numerator without normalization by sample concentration (c) and thickness (l) is known as absorbance. The inverse intensity ratio $T = I/I_0$ (before logarithmizing) is referred to as transmittance.

3.2.2 nmTransmission NEXAFS setup

The extinction coefficient of most materials in the soft X-ray regime is particularly high, requiring specific experimental setups. A high vacuum prevents absorption of the radiation by residual gases and in the case of a solid sample the contamination of the surface.

The absorbance can be indirectly determined by recording the fluorescence or electron emission resulting from the decay of the core-excited state. Molecular samples in solution are predestined for the direct detection of the transmitted intensity, as they can be characterized by liquid jet systems [124,98,36].

In the nmTransmission NEXAFS [39] setup used in this thesis, the pressurized sample solution enters the vacuum chamber through two nozzles with an orifice diameter between 20 μm and 50 μm (Fig. 3.1a). Upon collision of the two individual round jets, a thin liquid sheet with width and length in the order of 1 mm is formed. More importantly, the thickness profile of this flat jet system is around 1 μm which allows detection of a decent fraction of transmitted soft X-rays – typically in the percent range of the incident radiation. The extinction coefficient of the solute can then be determined by equation 3.8, if the thickness is estimated from the tabulated solvent transmittance [82,58].

The execution of an experiment like this is in practice very challenging, since any precipitate of the solute in the tubing or nozzles leads to jet instabilities. Additionally, the low pressure in the experimental chamber facilitates ice formation. In both cases, cleaning of the experimental setup at ambient pressure and a complete restart of the experiment are required. Nevertheless, this approach has several advantages over prior setups containing a liquid cell, in which the sample flows between two thin membranes [129,103]: Firstly, interactions of the sample or solvent with the windows do not need to be considered. Secondly, the thickness gradient in the flat jet can be used to adjust the sample thickness and resulting transmitted

intensity to the detection sensitivity. The possibility to measure at a fixed position, without the risk of breaking a membrane, reduces the sources of error. Thirdly, the fast sample replenishment in flat jet setups minimizes the risk of radiation-introduced sample damage[83].

The latter virtue is of primary importance for UV/VIS pump – soft X-ray probe spectroscopy. In this case, a laser pump pulse excites the sample molecules to a valence excited state, which is thereupon probed by an X-ray pulse. This can be theoretically described by applying equations 3.6 or 3.7 twice, first for the valence excitation $0 \rightarrow f_{\text{valence}}$ and then for the core excitation $f_{\text{valence}} \rightarrow f_{\text{core}}$. With the time resolution of the described setup at Bessy II ($\approx$ 50 ps[39]), not only the decay of a single core-excited state can be observed, but also transitions to other states, i.e. the intersystem crossing of a photoexcited porphyrin in publication IV. The basis for such a time-resolved NEXAFS experiment is the precise optimization of spatial and temporal overlap of the laser pump and X-ray probe pulses on a spot of the liquid sheet with the desired thickness and stability.

3.2.3 Information content of the NEXAFS

A static X-ray absorption spectrum of the 3HP/3PO isomers, which has been acquired with the nm-Transmission NEXAFS endstation, is shown in Figure 3.1b. If one of the features at 399.0 eV or 400.7 eV is ignored, the spectrum resembles the typical K-edge NEXAFS of simple (i.e. diatomic) molecules[139,53]: The energetically lowest feature corresponds to a transition of a N 1s electron to the lowest unoccupied molecular orbital, which is an antibonding π orbital, typically referred to as π^* resonance. Higher antibonding orbitals and the increasing density of Rydberg states cause a continuous rise of the absorbance towards the continuum of states, energetically located above the ionization potential (around 408 eV). At approximately 409 eV, a broad resonance can be seen. This feature is labeled by σ^* in Figure 3.1b, based on the assignment in the molecular orbital picture[139]. Alternatively, this peak may be interpreted as a shape resonance, since the position above the ionization potential can be explained by a centrifugal potential barrier, which temporarily traps the photoexcited electron. Scattering of this electron by neighboring atoms gives rise to the often observed correlation between the shape resonance energy and bond lengths[133,42]. Such a scattering process is dominating at higher photon energies commonly referred to as extended X-ray absorption fine structure (EXAFS)[139].

As it can be seen in Figure 3.1b, the width of the NEXAFS resonances is not constant, as assumed in equation 3.6. In practice, the Lorentzian broadening increases with the excitation energy, since the increasing overlap with continuum states leads to a continuous reduction of the final state lifetime[53]. Additionally, the features show an experimental broadening of Gaussian shape due to the finite bandwidth of the incoming radiation. The asymmetry of the feature at 400.7 eV indicates additional broadening due to vibrational motion suggesting that this π^* resonance corresponds to a protonated nitrogen site[151].

Due to the tautomeric constant of the sample $K_T \approx 1$[137], the shown spectrum is a mix of 3PO and 3HP signatures. The energy difference of the two π^* resonances can be reasoned by the charge difference between the $-$N$=$ and $-$NH$^+=$ sites leading to better screening of the core hole in the former case[107]. This shift is a general trend in N K-edge NEXAFS spectra[30,33] and relates to the chemical shift in photoelectron spectroscopy[102] by Koopmans' theorem (see section 3.1).

As clarified in publications I and III, the initial charge distribution in a molecule is insufficient to

explain the details of the absorption spectrum. Instead relaxation effects need to be considered, impeding an occasionally proposed one-to-one mapping between NEXAFS and the ground state density of states[117,108]. Consequently quantum-mechanical calculations which account for the absorption process are required for the detailed interpretation of X-ray absorption spectra.

3.2.4 X-ray absorption spectrum calculations

An overview of the calculation methods and their performance for the simulation of K-edge NEXAFS spectra of molecules is given by Fransson et al.. This section focuses on the approaches used in this thesis, which build upon the ground state methods being described in section 2.4.

The calculation of excited states based on the Hartree-Fock method demands a multiconfigurational approach, as provided by CASSCF. Core-exited states can be included by rotating the desired inner-shell orbital (e.g. N 1s) into the active space. For publication I, state-averaged (SA) CASSCF calculations have been carried out, in which a common set of molecular orbitals is optimized[27,155,109]. The absorption cross-section is then obtained by evaluating the transition dipole matrix elements between the multiconfigurational states.

Similar to ground state calculations, DFT provides a computationally more efficient alternative enabling the simulation of absorption spectra of large — or a large number of — molecular geometries. Time-dependent (TD) DFT is based on the TD analog of the first theorem of Hohenberg & Kohn by Runge & Gross. They showed that a one-to-one mapping between the TD many-electron wave function and a TD one-electron density exists. Therefore the evolution of all interacting electrons in time can be described by a non-interacting reference system with an equal electron density[29]. The resulting TD Kohn-Sham (KS) equation is equivalent to equation 3.1 for one particle, except that $\hat{H}$ is the KS operator containing the TD exchange and correlation functional of the TD electron density. In practice, commonly the temporally local, ground state exchange and correlation functionals are used – based on the assumption that there is no rapid change in density – and the initial state is provided by a ground state DFT calculation[106]. The perturbation of the TD KS equations by an electromagnetic field can finally be used to obtain transition dipole moments and energies[5].

For the calculation of transient NEXAFS spectra of different multiplicities after laser excitation, the restricted subspace approximation (RSA) for TD-DFT[55,150] has been applied in publication IV. As commonly assumed for calculations of X-ray spectra, the external oscillating field is infinitesimally small (linear response TD-DFT) and the donor orbital space is restricted to the ground state Kohn-Sham orbitals with anticipated reduced occupancy in the valence and core-excited state (core-valence separation). Since the NEXAFS consists of excitations to bound states, also the acceptor space is limited in the RSA to the lowest unoccupied orbitals. Thereby, the computational complexity is reduced to a feasible level while maintaining a high accuracy for the energetically lowest resonances – apart from the inherent self-interaction error and neglecting of the relaxation effects in TD-DFT.

In publication III, the alternative transition potential method (TP-DFT) is employed, which has been developed for the simulation of X-ray absorption spectra[145,106]. It is a derivation of the Slater transition state method[136]. Therein, an artificial intermediate state with half an electron both in the initial and final orbital is introduced to enable relaxation by the self-consistent optimization of this state. The orbitals of this auxiliary state are thus an approximation for the ground and core-excited state[106]. In TP-DFT,

only the reduced occupancy in the core is considered, which increases the efficiency of the calculations, because only one transition state needs to be calculated. Since the absorption cross-section in TP-DFT is based on the one-electron approximation, the state kets in equation 3.6 correspond to wave functions of single electrons. In detail, $|0\rangle$ and $|f\rangle$ represent optimized orbitals of the transition state and $\omega_{0\to f}$ relates to the corresponding orbital energy eigenvalues of the time-independent KS equation [34]. In the version used in this thesis [35], the energy scale of the resulting spectrum can be improved by calculating the first core-excited state, its energy difference to the ground state, and shifting the first transition to this energy difference. This Δ-KS approach accounts for many-electron effects, which are neglected in the transition potential calculation [34].

3.3 Resonant inelastic X-ray scattering

While NEXAFS, which has been presented in the previous section, is based on the absorption of X-rays, the radiative decay of the resulting core-excited state is assessed in RIXS. As shown in publication II of this thesis, the manifold of valence excited final states of the RIXS process provides site-specific information on the density and symmetry of occupied molecular orbitals. Thereby inter alia the individual electronic structure in tautomeric mixtures can be unraveled. In general, RIXS allows to probe a wide range of elementary excitations, [2] which might be dipole forbidden by other spectroscopic techniques (section 3.1) and provides a sub-natural line width giving rise to the investigation of vibrationally excited states. The possibility to reconstruct potential energy surfaces (section 2.1) from such high-resolution data is a key motivation for the METRIXS and hRIXS spectrometers, which have been in part commissioned and optimized regarding the data acquisition as part of this thesis.

3.3.1 Site-selective probe of occupied states

The chemical selectivity of RIXS, which it inherits from the X-ray absorption step, can be seen from the N K-edge measurement of the 3HP/3PO tautomers in aqueous solution. Figure 3.2a shows the resulting RIXS spectra on the vertical axis for an incoming photon energy range from 398.3 to 401.7 eV. Such a two-dimensional representation is called RIXS map and yields a (partial fluorescence yield) NEXAFS spectrum by integrating the intensity along the scattered photon energy axis. Even though the absorption events are limited to the ones causing a radiative decay in this emission energy range, this NEXAFS spectrum resembles the one in Figure 3.1b.

By the coupling of the absorption and emission step during the RIXS process, the 3HP/3PO tautomers can be selected by the excitation energy and studied individually, which has been a persistent challenge within the field of physical chemistry. In publication II, RIXS is proposed as a general tool to disentangle the electronic structures of tautomeric mixtures. The scattered photon energies at the absorption resonances of the respective chemically active site represent the excited state manifold up to the extended UV region providing information on chemical bonds and solvation effects, which are both related to the origin of tautomerism at the atomic scale.

The emitted photon energy distribution is dominated by the elastic scattering signal (white area in Fig. 3.2a), for which the initial and final electronic states are equivalent. If the final state is valence-excited, the energy loss during the non-elastic scattering event provides information on the electronic levels below

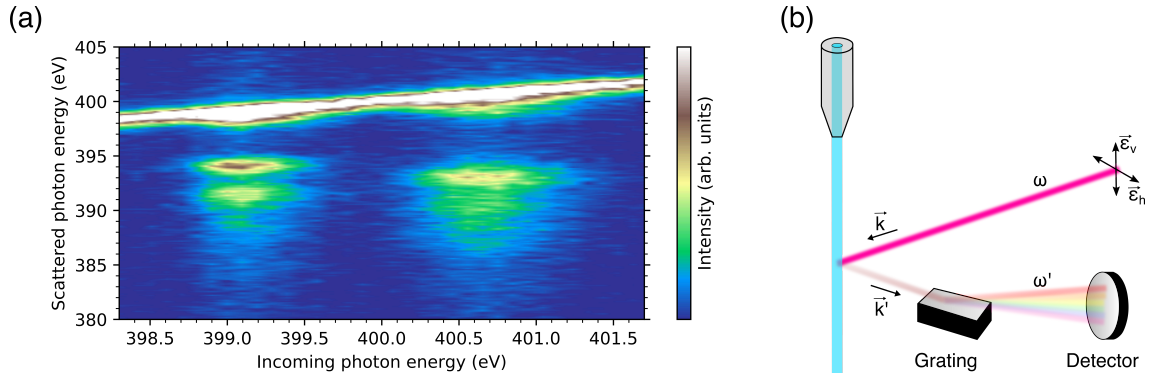

Figure 3.2: a) N K-edge RIXS map of 3HP/3PO tautomers in aqueous solution (data from publication II). b) Measurement scheme of the EDAX RIXS spectrometer.

the Fermi edge[156]. In the present case, only the 3HP resonance (399.0 eV excitation) shows an intense feature with an energy loss of 5 eV (394 eV emission). This feature results from the core hole decay by an electron from the non-bonding nitrogen lone pair. Thus, this transition is not observed for the locally protonated 3PO tautomer (400.7 eV excitation). The remaining differences are a result of the inversion of orbital polarization between the two species, as uncovered in publication II. The interpretation of RIXS spectra is generally facilitated by the theoretical description of the scattering process.

3.3.2 Theoretical description

From the golden rule (equation 3.2), the RIXS cross-section within the dipole approximation can be derived[2].

$$\sigma_{\mathrm{RIXS}} \propto \frac{\omega'}{\omega} \sum_f \left| \sum_i \omega_{i\to f}\,\omega_{0\to i} \frac{\langle f|\vec{\varepsilon}\,'\cdot\hat{r}|i\rangle\langle i|\vec{\varepsilon}\cdot\hat{r}|0\rangle}{\omega-\omega_{0\to i}+\mathrm{i}\Gamma_i} \right|^2 \Delta(\omega-\omega'-\omega_{0\to f},\Gamma_f) \tag{3.9}$$

ω, $\vec{\varepsilon}$ and ω', $\vec{\varepsilon}\,'$ denote the frequency and polarization of the incoming and outgoing X-rays, respectively. As seen in the denominator, the scattering process is resonantly enhanced when the energy of the incoming photon is equal to the energy difference of the initial ground ($|0\rangle$) and intermediate core-excited state ($|i\rangle$). Due to energy conservation, the energy loss during the scattering event provides information on the valence or vibrational excited final state ($|f\rangle$).

The squared term is also known as Kramers & Heisenberg equation, in which Γ_i represents the considerable lifetime broadening of the intermediate state, mainly due to the previously neglected non-radiative decay channels[2]. It should be emphasized that the transition amplitudes are added before the intensity of the united process is revealed by squaring the sum. This allows interference of multiple excitation–emission channels, in cases where the two-step approximation with a single intermediate state is insufficient. In general, RIXS should be considered as a one-step scattering event[120,23].

The width of the Lorentzian function (Δ – as defined for equation 3.6) depends on the final state lifetime. For RIXS, the final state is long-lived, so that the intrinsic broadening is comparatively small. Since the spectral resolution is not limited by the core-excited intermediate state, RIXS is known to possess a sub-natural linewidth[47].

Calculational access to the RIXS cross-section can be granted by several wave function and DFT-

based methods[106]. The relevant approach for this thesis is the RSA-TD-DFT method. As described in section 3.2.4, both core and valence excited states, which are the relevant ones for the RIXS process, can be calculated efficiently with this method. The truncation of the occupied and virtual orbital spaces is justified by the dominance of resonant scattering in the emission spectrum of the energetically lowest core-excited states. The RIXS cross-section can finally be obtained from the transition dipole moments between these states according to equation 3.9. The appealing properties of this method are the high quantitative accuracy of the calculated emission spectra (on the relevant energy loss scale), as well as the speed and automatability of the execution. The latter advantages have been utilized in publication II, to explicitly treat dynamic solvation effects, by calculating an averaged RIXS spectrum from a large number of solvent configurations provided by a molecular dynamics simulation (section 2.5.1). Additionally, the approach allows the inclusion of quantum nuclear dynamics to simulate high-resolution RIXS spectra[150].

3.3.3 Experimental access to orbital symmetry and nuclear dynamics

The decay of core-holes is strongly dominated by the non-fluorescent emission of Auger electrons, which means that RIXS measurements require highly optimized setups.

The EDAX spectrometer for liquid samples[84] has been installed and commissioned at the high flux beamline UE49-SGM at Bessy II (Helmholtz-Zentrum Berlin für Materialien und Energie) in the course of this thesis. This setup, which has been used to acquire the presented RIXS map (Fig. 3.2a) and the spectra for publication II, is schematically represented in Figure 3.2b.

Compared to the nmTransmission NEXAFS endstation (section 3.2) a single, round liquid jet is sufficient for RIXS, since transmission of light is not desired. As before, constant sample replenishment prevents radiation-induced sample damage, which is of particular importance for the comparatively long acquisition times of RIXS spectra. Three turbo-molecular pumps and a cold trap filled with liquid nitrogen compensate for the evaporated liquid to ensure a constantly low pressure ($\approx 10^{-4}$ mbar) in the experimental chamber and two more pumps are used in the differential pumping unit, preventing a pressure increase in beamline ($< 10^{-7}$ mbar).

The diameter of the liquid jet around 20 μm is similar to the comparatively small focus size of the incoming X-rays, so that a maximum number of photons is absorbed by the sample, while the spot size is small enough to serve as the source point for the high-transmission, medium-resolution spectrometer[105]. Based on the Rowland principle, the emitted radiation is spectrally dispersed by a grazing-incidence, spherical grating and at the same time focused on a spatially resolved detector. Therein, the photons are transformed and amplified to electron clouds impinging on a fluorescence screen, which is recorded by a CCD camera.

The symmetry of the emitting orbital can be determined, even though the molecules are randomly oriented in the liquid jet, due to the variable polarization of the incoming light ($\vec{e}_v$, $\vec{e}_h$ – as depicted in Fig. 3.2b) and the 90 ° angle between the incoming ($\vec{k}$) and analyzed scattered radiation ($\vec{k}' \,||\, \vec{e}_h$) in the EDAX endstation[150]. Generally, a low scattering intensity is expected for emission in the polarization direction of the incoming light, when the excitation and relaxation are equally polarized. Therefore elastic scat-

tering is suppressed in this setup for horizontal polarization ($\vec{e}_h$), as well as a $\pi \rightarrow$ 1s de-excitation as a consequence of an 1s$\rightarrow \pi^*$ transition. In contrast, a $\sigma \rightarrow$ 1s de-excitation is enhanced and the opposite applies if the incoming radiation is vertically polarized ($\vec{e}_v$)*. This feature of RIXS can be exemplary seen in the 3HP/3PO map (Fig. 3.2a), which has been acquired with vertically polarized incident radiation and shows a strong elastic line and enhanced 1s$\rightarrow \pi^*$, $\pi \rightarrow$ 1s features in the energy loss range from 6 to 10 eV. By comparing RIXS spectra of both polarizations, the orbital symmetry can thus be assigned purely experimentally.

Dedicated high-resolution RIXS spectrometers are required in order to resolve vibrational excitations in the millielectronvolt range. That this condition is not met by the EDAX setup can be seen by the elastic line in Figure 3.2a, which is unstructured also in the broader regions at the absorption resonances, indicating an underlying vibrational progression. Both the METRIXS and the hRIXS setups will be able to study the nuclear motion of core-excited molecules in a liquid jet. They are based on a similar setup, but contain an optimized spectrometer to achieve at least one order of magnitude higher resolving power in the soft X-ray regime – to the expense of a reduced transmission. For METRIXS (Bessy II), a control and acquisition software has been developed and tested as part of this thesis. Additionally, the commissioning of hRIXS spectrometer (European XFEL, Hamburg/Schenefeld) has been accelerated by real-time data analysis and support.

With these experimental setups, it will be possible to gain access to the ground state potential energy surfaces (section 2.1), for example of aromatic molecules, which determines their thermally driven chemistry [130]. Such an experiment is based on the propagation of the nuclear wave packet on the core-excited state potential energy surface, enabling radiative vertical transitions to the manifold of vibrational excited states on the ground state potential. The detected vibrational progression can then be used to reconstruct the ground state potential energy surface along the stretching, or bending coordinate of the respective core-exited state [32].

High-resolution RIXS experiments require the highest incident X-ray brilliance of the presented methods. The intense and short pulses of the European XFEL will also allow to perform laser pump – RIXS probe studies with the hRIXS setup. The generation of highly intense X-rays with a narrow bandwidth, controllable polarization, and a defined time structure is the focus of the following section.

3.4 Synchrotron radiation

While the X-ray beam being absorbed or scattered by the sample has been taken for granted in the past sections, the required highly intense radiation with a narrow bandwidth in the full soft X-ray regime from 100 to 1000 eV is currently only provided by a limited number of synchrotron and free electron laser (FEL) facilities. Laboratory laser-based sources, reaching higher and higher energies with a sufficient intensity over time, might serve as an alternative in the future [153,138]. For the publications presented in this thesis, beamtime has been proposed and granted by the synchrotron Bessy II (Helmholtz-Zentrum Berlin für Materialien und Energie). As the preparation for the experiments, which are presented in this thesis, included the commissioning of the respective beamline, the working principle of such a light source is outlined in this section.

*The polarization anisotropy of RIXS is quantitatively described in the supporting information for publication II.

In every synchrotron and FEL, X-rays originate from the deflection of relativistic electrons. In principle, any charged particle emits bremsstrahlung, if it does not rest or move along a linear trajectory with constant velocity. In the storage ring of a synchrotron, single dipoles – or bending magnets – force the electrons on a cyclic path. If the electrons would have a velocity much smaller than the speed of light, radiation would be emitted symmetrically around the axis of acceleration. However, close to the speed of light, the electromagnetic radiation is centered on the propagation direction of the electrons forming a beam of light with wavelengths typically up to the hard X-ray regime[66].

Especially for "photon hungry" RIXS experiments, the brilliance of a bending magnet is not sufficient. All results of this thesis are therefore based on measurements at an undulator beamline. Undulators can be inserted between two bending magnets of the storage ring because the incoming and outgoing electron propagation direction is equal. Inside the undulator, at least two rows of alternating magnets cause a meander-like shape of the electron trajectory. The deviations from a linear movement are chosen to be small, so that the emitted radiation cones interfere, producing a more narrow beam with a lower bandwidth than for larger oscillations.

The n^{th} maximum wavelength or undulator harmonic is given by[60]

$$\lambda_n = \frac{\lambda_u}{2\,n\,\gamma^2}\left[1 + \left(\frac{e}{2^{3/2}\,\pi\,m_e\,c} B\,\lambda_u\right)^2 + (\gamma\,\theta)^2\right], \tag{3.10}$$

where λ_u is the period length of the magnets, γ is the Lorentz factor, and θ denotes the emission angle. For adjusting the maximum photon energy e.g. in a NEXAFS measurement, the magnetic field B is varied by changing the distance between the magnetic poles (also known as undulator gap).

An interesting aspect of equation 3.10 is that the Lorentz factor is applied twice, allowing an undulator with a period of e.g. $\approx$ 5cm (as used for all publications) to produce X-rays with a wavelength in the order of a few nanometers. This effect can be reasoned by the length contraction of the undulator in the frame of the relativistic electrons and the Doppler shift of the radiation frequency in the frame of the stationary experimental setup[60].

The undulators used for the publications included in this thesis allow to study samples with a variable polarization (as used in publication II, see also section 3.3.3). This is accomplished by four rows of magnets with four magnets per undulator period, which are oriented in different directions – two along and two perpendicular to the electron trajectory. If the rows are not shifted against each other, horizontally polarized light is generated and at a shift of two rows amounting to half of the undulator period vertically polarized light is provided. Other shifts can be used to generate circularly/elliptically polarized X-rays[126].

Even though, the radiation of an undulator is energetically concentrated at the harmonics and has a comparatively low divergence, these two properties need to be further optimized for most experiments including the ones in this thesis. A narrow bandwidth of the X-rays is achieved by a monochromator, which consists of a grating (similar to the one in the EDAX endstation – Fig. 3.2b) and an exit slit. The width of the exit slit allows to adjust the bandwidth at the expense of intensity. Additionally, mirrors are used to direct and focus the beam onto the sample.

The radiation, that is made accessible to a wide range of experiments by the presented instruments, leads to a lowering of the energy of the electrons in the storage ring. This loss is compensated by radio-

frequency cavities. Therein the electrons are accelerated by the potential of a radio wave depending on their timing of entering the cavity. In principle, slower electrons experience a larger acceleration than faster electrons. If the electrons arrive outside of the desired time window, the effect is inverted and the electrons are lost[156]. Therefore the radio-frequency cavities cause a non-constant fill-pattern in the storage ring providing a time structure of the radiation, which can be used for pump-probe experiments (as in publication IV).

X-rays with a higher temporal resolution and brilliance are provided by FELs. In these facilities, electrons are linearly accelerated and finally pass through an undulator, which is typically a few hundred meters long. Therein, the electric field of the emitted radiation interacts with the transversely oscillating electrons. The resulting Lorentz force accelerates or decelerates the electrons depending on their position with respect to the phase of the electromagnetic radiation. As a consequence, the electron beam is divided into microbunches with a distance corresponding to the wavelength of their emitted radiation. Eventually, the emitted X-rays line up in phase (as well as the electrons) maximizing the intensity of the beam at the wavelength given by equation 3.10. When saturation of the self-amplified spontaneous emission (SASE) process is reached, the peak intensity is increased by more than nine orders of magnitude, due to the coherence of the emitted radiation. This enables new opportunities for RIXS and NEXAFS measurements, such as time-resolved studies at the ultrafast timescale thanks to the femtosecond lasting highly-intense microbunches[6].

4

Results

How Hydrogen Bonding Amplifies Isomeric Differences in Pyridones toward Strong Changes in Acidity and Tautomerism

R.Büchner, M. Fondell, E. J. Mascarenhas, A. Pietzsch, V. Vaz da Cruz, and A. Föhlisch

The Journal of Physical Chemistry B 2021, 125, 9, 2372–2379[*]

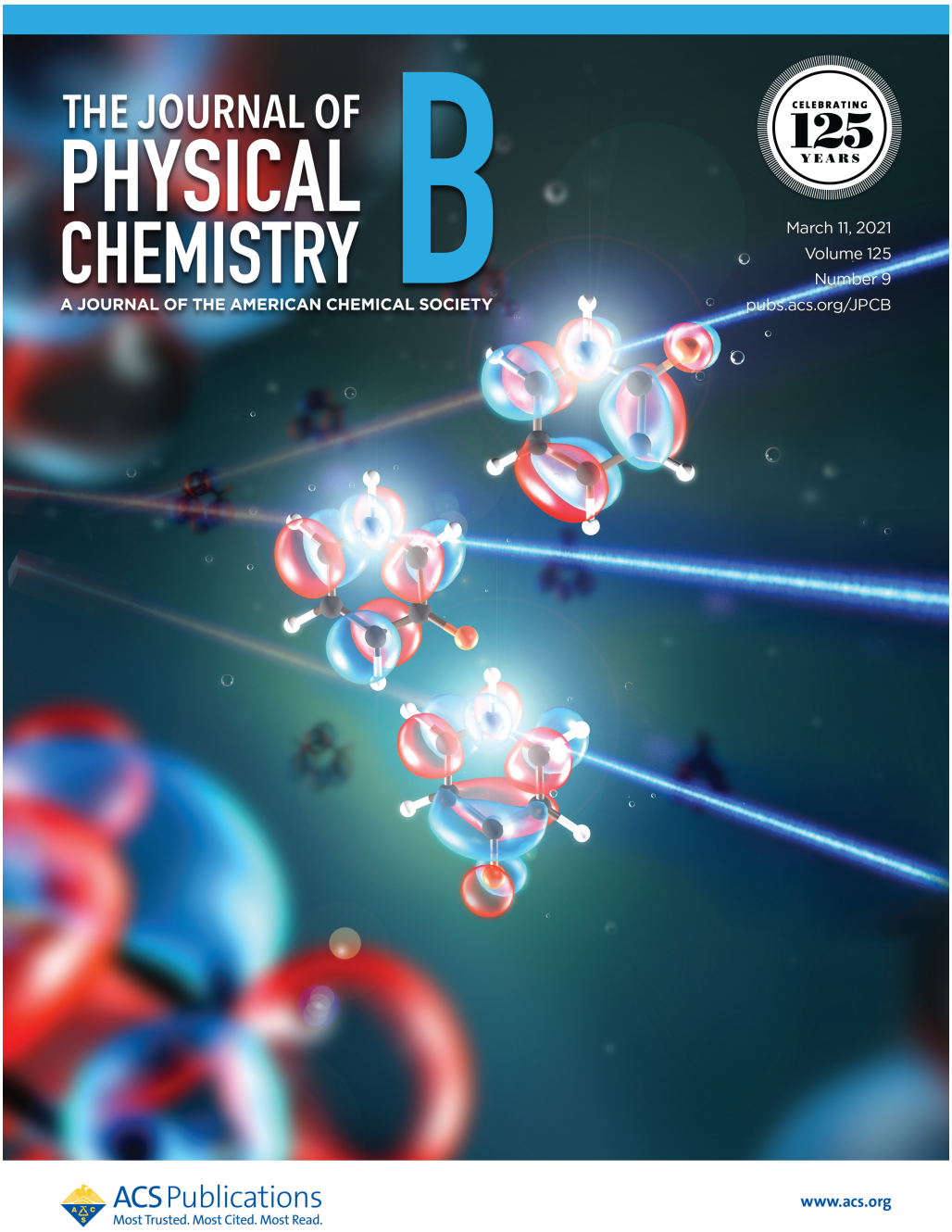

[*]Reprinted with permission from J. Phys. Chem. B 2021, 125, 2372–2379. Copyright 2021 The Authors. Published by American Chemical Society. You can view the full text of this article at http://pubs.acs.org/articlesonrequest/AOR-VEWPNQYEJNZGGVI8NHIJ to download this article. (CC BY-NC-ND 4.0)

THE JOURNAL OF PHYSICAL CHEMISTRY B
A JOURNAL OF THE AMERICAN CHEMICAL SOCIETY

pubs.acs.org/JPCB

Article

How Hydrogen Bonding Amplifies Isomeric Differences in Pyridones toward Strong Changes in Acidity and Tautomerism

Robby Büchner,* Mattis Fondell, Eric J. Mascarenhas, Annette Pietzsch, Vinícius Vaz da Cruz,* and Alexander Föhlisch

Cite This: *J. Phys. Chem. B* 2021, 125, 2372−2379

Read Online

ACCESS | Metrics & More | Article Recommendations | Supporting Information

ABSTRACT: Steric hindrance of hydration and hydrogen bond enhancement by localized charges have been identified as key factors for the massive chemical differences between the hydroxypyridine/pyridone isomers in aqueous solution. While all isomers occur mainly in the hydroxypyridine form in the gas phase, they differ by more than 3 orders of magnitude both in their acidity and tautomeric equilibrium constants upon hydration. By monitoring the electronic and solvation structures as a function of the protonation state and the O^- substitution position on the pyridine ring, the amplification of the isomeric differences in aqueous solution has been investigated. Near-edge X-ray absorption fine structure (NEXAFS) measurements at the N K-edge served as the probe of the chemical state. The combination of molecular dynamics simulations, complete active space self-consistent field (CASSCF), and time-dependent density functional theory (TD-DFT) spectral calculations contributes to unraveling the principles of tautomerism and acidity in multiple biochemical systems based on tautomerism.

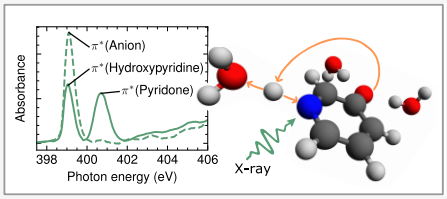

INTRODUCTION

The proton transfer connecting the enolic hydroxypyridines (HPs) and ketonic pyridones (POs) is prototypical for tautomerism in biological systems.[1,2] As seen in Figure 1, both HP and PO occur in three isomeric structures of varying distances between the nitrogen and oxygen functional sites, ranging from ortho (2HP/2PO) to meta (3HP/3PO) to para (4HP/4PO). Due to these geometric differences, the oxygen substituent is conjugated with the pyridine ring in the keto forms of the ortho and para isomers (2PO and 4PO), whereas the meta isomer has no conjugate carbon−oxygen path neither in the 3HP nor the 3PO form.

Independent of these structural variations, the enol form (HP) is favored over the keto tautomer (PO) in the gas phase by all isomers.[1] Upon aqueous solvation, massive differences between the equilibration of the ortho and para versus the meta isomers occur with regard to their tautomeric equilibrium, acidity, and photoreactive properties, with significant implications to their functionalities.

In aqueous solution at room temperature, the ortho and para isomers shift equilibrium away from the gas phase 2HP and 4HP forms to the 2PO and 4PO forms, whereas the meta isomer equilibrates as an equal mixture of the 3HP and 3PO tautomers[3,4] (see Figure 1). These local configurations in aqueous solution are accompanied by a similar acidity of the ortho (mainly 2PO) and para (mainly 4PO) isomers in contrast to the mixed (3HP/3PO) meta isomer. In addition, the meta isomer in aqueous solution contains with its 3HP form an efficient UV chromophore, whereas the ortho 2PO and para 4PO isomers do not act as such.

Since 3HP/3PO constitutes inter alia the core moiety of vitamin B_6,[7,8] i.e., increased photosensitivity is caused upon vitamin B_6 overdosing in humans, related to the enolic 3HP tautomer in aqueous solution.[9]

The ortho tautomer is directly related to multiple nucleobases of DNA and RNA,[10] where tautomerism and acidity can lead to mutations and diseases, i.e., by altering the hydrogen bond patterns in DNA.[11,12] Nevertheless, biological processes such as the removal of damaged nucleobases[2] or the versatile catalysis by RNA enzymes[13] depend on the acidity and tautomerism of nucleobases. Understanding the principles of the HP/PO protonation states sheds light on the evolution of nucleobases as storage for genetic information in all living organisms[13] and helps to design active substances for new medical treatments (e.g., viral lethal mutagenesis[14]).

In this work, it is established, as a function of the protonation state and the position of the O^- substituent on the pyridine ring, how charge differences and the steric hindrance of hydrogen bond coordination to the first aqueous solvation shell drive, on a microscopic level, the amplification

Received: December 4, 2020
Revised: January 11, 2021
Published: February 9, 2021

https://dx.doi.org/10.1021/acs.jpcb.0c10873
J. Phys. Chem. B 2021, 125, 2372−2379

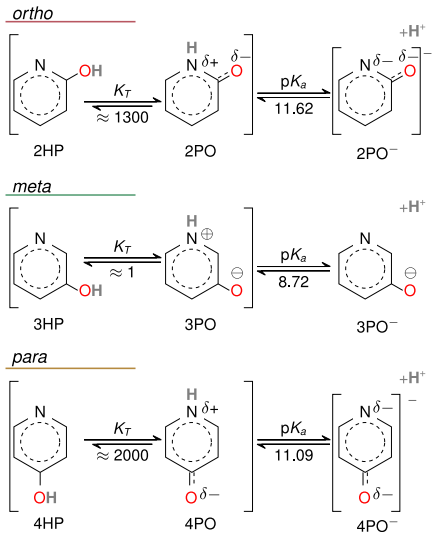

Figure 1. Equilibrium structures in aqueous solution of the hydroxypyridine/pyridone (HP/PO) tautomers for the ortho, meta, and para isomers and their fully deprotonated states. They vary in oxygen conjugation, tautomeric equilibrium (K_T = [PO]/[HP][3,4]), and acidity (pK_a[5,6]). Resonance structures are given in the Supporting Information.

of the initially small molecular differences of the three HP/PO isomers, causing, macroscopically, 3 orders of magnitude variation in tautomeric constants and acidity among the ortho, meta, and para isomers in aqueous solution. The findings are based on the element-specific orbital state populations, chemical sensitivity of near-edge X-ray absorption fine structure (NEXAFS) combined with molecular dynamics (MD) simulations connected to the ab initio X-ray spectrum calculations at the level of complete active space self-consistent field (CASSCF) and time-dependent density functional theory (TD-DFT). In this effort, the ortho, meta, and para pyridone isomers; their fully deprotonated forms, respectively; and the protonated and deprotonated pyridine precursor are investigated in aqueous solution.

METHODS

Experimental Details. All samples were purchased from Sigma-Aldrich with a minimum purity of 95% and dissolved in deionized water to obtain 0.1 M solutions. The protonation (of pyridine) and deprotonation (of pyridones) were established by a 1.2-fold molar excess of HCl and KOH, respectively.

The nmTransmission NEXAFS endstation facilitates the spectroscopic investigation of dissolved organic compounds in the soft X-ray regime.[15] The sample enters the experimental chamber through two nozzles leading to liquid jets, which form a leaf-shaped surface upon collision. The thickness of the liquid sheet can be varied in the region of the penetration depth of soft X-rays so that transmission measurements become feasible. At the same time, radiation-induced sample damage is prevented through continuous sample replenishment. For the present investigation, a flow rate of 2.5−3.0 mL/min was used in combination with 46 μm sized nozzles.

Photons were provided by Bessy II (Helmholtz-Zentrum Berlin) beamlines UE49-SGM[16] for prestudies and UE52-SGM[17] for the quantitative absorption measurements. Bandwidths of 0.16 eV (in the case of 2PO) and 0.11 eV (otherwise) were used. The presented spectra were recorded in 0.05 eV steps with an average acquisition time of 6s per point.

The extinction coefficient (ϵ) was obtained from transmittance (T) and concentration (c) according to Beer−Lambert's law.

$$\epsilon = \frac{-\log_{10} T}{c \times l}$$

The sample thickness (l) was estimated using tabulated values[18] of the water transmittance at 396 eV yielding 9.2 ± 0.9 μm for 2PO and 5.6 ± 0.6 μm for the other samples.

Since the first region of the spectrum is predominantly independent of the dissolved sample, it is not only used for the calculation of the thickness but also to remove the background of the water transmittance by a linear fit.

For the energy calibration of the experimental results, the signature of co-dissolved N_2 at 400.84 eV[19,20] was used. A fit of these features in the spectrum of the pristine solvent was subtracted from the spectra of deprotonated samples to yield the pure NEXAFS of the investigated substances.

Computational Details. All electronic structure calculations were carried out with the Orca package.[21] All geometries were optimized at the RI-MP2 level with the aug-cc-pVTZ using the aug-cc-pVTZ/C auxiliary basis. The RI-JK approximation was used with the aug-cc-pVTZ/JK fitting basis set.

The MD simulations were performed with the Gromacs package. The OPLS-aa force field has been used for parameterization except for the charges for the intermolecular Coulomb interactions, which were derived by the chelpg[22] procedure (based on the relaxed RI-MP2 density). The water molecules were described by the SPC/Fw[23] model. Additional details regarding the MD simulations are available in the Supporting Information.

From the MD simulations, minimally solvated models were constructed, including only the hydrogen bonding interactions with the N:, N−H, O−H, and C=O functional groups. These minimally solvated models were used for the subsequent spectral calculations at the CASSCF and TD-DFT levels of theory.

To model the behavior of the lowest π^* resonance across the systematic series, CASSCF calculations were carried out in the gas phase, as well as explicitly solvated. The aug-cc-pCVTZ basis set was used for all atoms except for the nitrogen, which was described by the larger aug-cc-pCVQZ. In the solvated cases, the explicit water molecules were described by the smaller cc-pCVDZ basis. The bulk-liquid effects were modeled by the conductor-like polarizable continuum model[24] (CPCM). The CASSCF calculations used RI-MP2 natural orbitals as a starting point. The π orbitals of the conjugated ring were included in active space, namely, six active electrons in six orbitals, henceforth called CAS(6,6). This setup excludes only the oxygen lone pair orbital, which is usually poorly correlated in CASSCF calculations. Using this active space, a state-averaged (SA) calculation was carried out for the ground state and the lowest valence-excited state. The valence CASSCF solution was then used as a starting point for the core-state calculation. The N(1s) orbital was rotated into the active space leading to CAS(8,7); then, an SA-CASSCF calculation was carried out including only the ground state and

https://dx.doi.org/10.1021/acs.jpcb.0c10873
J. Phys. Chem. B 2021, 125, 2372−2379

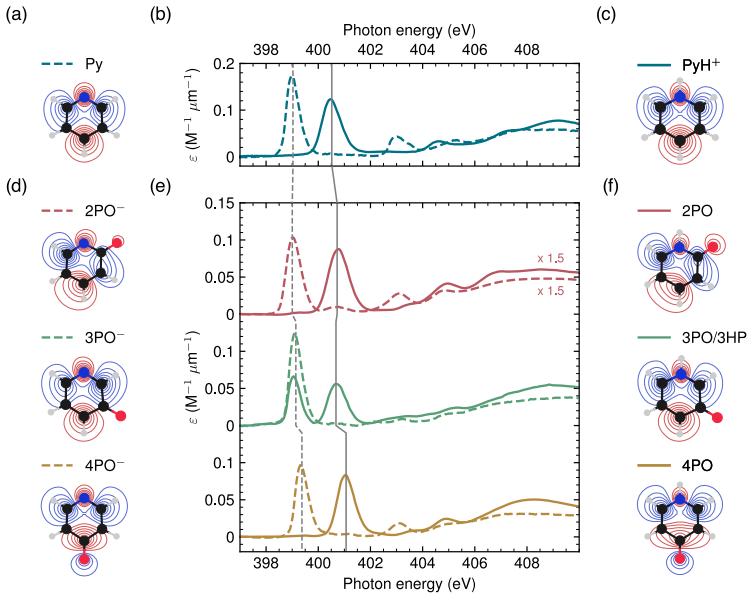

Figure 2. N K-edge NEXAFS spectra of the pyridine precursor (b) and the ortho, meta, para pyridone isomers from top to bottom (e). A protonation shift of the N(1s) → π^* resonance is observed across the series. The energies of these transitions are influenced by the competition for charges between nitrogen and oxygen in the core-excited state, as illustrated by the π^* orbital plots of the fully deprotonated (a, d) and protonated species (c, f).

the lowest core-excited state. This setup is expected to recover the majority of static and dynamic correlations for the π^* transitions.

For Figure 4, the CASSCF transition moments were shifted by −0.75 eV and convoluted with a Voigt profile of 0.13 eV lifetime broadening[25] and 0.51 eV (deprotonated nitrogen) or 0.80 eV (protonated nitrogen) experimental broadening to match the experimental results.

TD-DFT calculations were performed to study the remaining resonances of the X-ray absorption spectra. The PBE0[26] hybrid functional was used in all calculations. Additional details are available in the Supporting Information.

RESULTS AND DISCUSSION

General Protonation Shift. Near-edge X-ray absorption fine structure (NEXAFS) at the nitrogen K-edge allows us to distinguish and quantify the protonation state at the nitrogen atom. Both the directly coordinated hydrogen atom and the hydrogen bond toward coordinated water molecules in the first solvation shell are monitored in this approach.

In Figure 2b,e, the N K-edge NEXAFS of the ortho, meta, and para isomers are presented, as well as their fully deprotonated states in direct comparison to the (pyridine/Py) precursor and its conjugated acid (pyridinium/PyH^+). A characteristic blue shift of the lowest unoccupied molecular orbital (LUMO) π^* state is observed for all molecules upon protonation (depicted in Figure 2b,e) via the one-electron transition (≥72%) of the N(1s) electron elevated to the lowest unoccupied π^* orbital.

The photon energy range of 402−406 eV monitors excitations into higher unoccupied molecular orbitals, mostly of σ^* character. In the region of 403.4−403.8 eV, a shoulder (≈0.01 M^{-1} μm^{-1}) is observed, which is only present in the protonated state. This feature originates from a transition that is mostly localized at the N−H bond. Consequently, it is missing in the spectra of deprotonated species.

The N *K*-edge spectra of the pyridones (see Figure 2e) largely resemble the NEXAFS of $Py(H^+)$. Only the meta isomer exhibits a second π^* resonance closely below the feature of $3PO^-$ due to the presence of the HP tautomer. No indication of the presence of 2HP and 4HP has been found, in agreement with the tautomeric equilibrium constants (see Figure 1).

The shape resonances above 406 eV differ both between the pyridone isomers and in comparison with $Py(H^+)$. These quasi-bound transitions are known to provide information on interatomic distances.[27] The shape resonances are most pronounced in the spectra of PyH^+ and 4PO, where the nitrogen atom has an equal distance to both neighboring carbon atoms. The position of this feature is in qualitative agreement with the calculated C−N bond distances: 408.2 eV for 4PO (1.351 Å) and 409.3 eV for pyridinium (1.342 Å). For 3HP/3PO with 1.341−1.346 Å C−N bond distances, the resonance position is intermediate (409.1 eV) and in 2PO the distances differ so widely (1.356, 1.369 Å) that the shape resonance position cannot be assigned unambiguously.

The shape resonance of the deprotonated species seems to be red-shifted similar to the other features. This effect is not caused by the minor changes of the C−N bond distance upon deprotonation but by a general adjustment of the electronic and solvation structures, as discussed in the following sections.

Isomer Specific Charge Distribution. Even though all pyridones show a protonation shift similar to that of $Py(H^+)$, the exact peak positions differ depending on the position of the O^- substituent. This becomes particularly clear from a

https://dx.doi.org/10.1021/acs.jpcb.0c10873
J. Phys. Chem. B 2021, 125, 2372−2379

comparison of the π^* resonances, which also have been used to investigate tautomerism in the past.[28]

Besides the peak position, the width of the π^* resonance depends on the protonation state (of the nitrogen atom in the respective molecule). The broadening (full width at half-maximum (FWHM) + 0.29 eV) for pyridinium/pyridones results mainly from Franck−Condon vibrational excitations[29] of the N−H bond during the X-ray absorption process, which are absent in the deprotonated species.

The interspecies shift of the π^* resonance, first, depends on the initial electron density at the (nitrogen) atom, which is excited during the X-ray absorption process.[30] The better the core charge is screened, the lower is the ionization energy of N(1s) electrons. As far as resonant absorption features are considered, the core electron is excited into a bound state. Since the transition energy depends, inter alia, on the energy of the initial orbital of this electron, excitation and ionization energies are linked by Koopmans' theorem. Therefore, the NEXAFS peak position contains information on the chemical state of nitrogen in the samples.

$2PO^-$ has the highest charge density at the nitrogen site and the smallest ionization potential, followed by $4PO^-$ where the charge is more distributed over the whole molecule. In $3PO^-$, the electron density is shifted to the oxygen, and in Py, the charge at the nitrogen site is even lower, since the molecule is formally neutral. The same argumentation holds for the protonated case, even though the screening capacity is lower for all species (see Figure 1).

Second, the relaxation of the final state due to the Coulomb attraction between the excited electron and the core-hole influences the excitation energy, especially of the lowest NEXAFS feature. As known from benzene,[31] the higher the contribution of the atomic orbital at the excited atom to the relaxed molecular orbital, the more the red shift of π^* resonances. In other words, the π^* resonance is lowered, if the lowest unoccupied molecular orbital (LUMO) is centered at the nitrogen atom after its relaxation.

The relaxed π^* orbitals are depicted in Figure 2a,c,d,f for the fully deprotonated and protonated Py(H^+) and pyridones. It can be seen that in the PyH^+ case, the probability of the excited electrons to be close to the carbon atoms in the *meta* position is nearly zero. Oppositely, in 4PO, the LUMO is distributed over all carbon atoms and has a strong contribution from the oxygen. Consequently, the excitation energy ($h\nu_{\pi^*}$) of PyH^+ is expected to be strongly red-shifted, whereas only slight deviations are expected for 4PO. The shift of 3PO and 2PO, due to the described final state effect, is intermediate. If single molecules are compared between their protonation states, it is observed that the deprotonated entity has a LUMO, which is more localized at the nitrogen site. Consequently, the blue shift upon protonation is increased by final state effects.

Taking these relaxation effects into account, it can be understood that the initially expected state order $h\nu_{\pi^*}(2PO^-) < h\nu_{\pi^*}(4PO^-) < h\nu_{\pi^*}(3PO^-) < h\nu_{\pi^*}(Py)$ is disturbed by the creation of the core-hole leading to $h\nu_{\pi^*}(2PO^-) < h\nu_{\pi^*}(PyH) < h\nu_{\pi^*}(3PO^-) < h\nu_{\pi^*}(4PO^-)$. In the protonated case, the excitation energy of PyH^+ is lowered to beneath that of $h\nu_{\pi^*}(2PO)$ due to final state effects. This order of resonance energies is observed both experimentally and in the calculations (see Table 1).

By causing the characteristic π^* shifts, the core-hole effect provides detailed information on the isomeric differences in charge distribution. In Py(H^+), nitrogen is the most electronegative element and the excited electron, therefore, remains in close proximity. In the pyridones, nitrogen competes for electron density with oxygen. This effect increases from $3PO^{(-)}$ to $2PO^{(-)}$ to $4PO^{(-)}$. In $3PO^{(-)}$, the oxygen is not part of the conjugated system and is already in a charged state. In $2PO^{(-)}$, both the oxygen and nitrogen atoms are part of the aromatic structure but pull charge in similar directions. In contrast, the conjugated oxygen in $4PO^{(-)}$ withdraws charge from the nitrogen site, as they lie in opposite sites of the ring.

Table 1. Experimental and Calculated (CASSCF) N K-Edge π^* Resonance Positions in eV

	deprotonated			protonated		
molecule	calcd gas	calcd aq.	exptl	calcd gas	calcd aq.	exptl
Py(H^+)	399.68	399.78	399.03	401.78	401.21	400.52
$2PO^{(-)}$	399.34	399.87	399.00	402.10	401.54	400.72
$3PO^{(-)}$	400.04	399.91	399.14	402.14	401.41	400.72
$4PO^{(-)}$	400.25	400.09	399.37	403.15	401.67	401.07

In short, the constitutional differences between the pyridone isomers cause considerable differences in the electronic structure and charge distribution. These variations are already present in the gas phase, as the CASSCF calculations show (see Table 1). Nevertheless, without an aqueous environment, the electronic differences are not mirrored by macroscopic properties, i.e., the tautomeric equilibrium constants. To gain an insight into the microscopic amplification of the isomeric differences by solvent−solute effects, the solvation structure is analyzed in the following section.

Hydrogen Bonding Interactions. Figure 3 shows how the heteroatoms govern the solvent−solute interactions of Py and the pyridone isomers. In Py, the nitrogen atom accepts on average 0.9 hydrogen bonds (HBs) from water, whereby the bonds are mostly localized out of plane.[32,33] If the nitrogen atom is protonated, it naturally cannot accept HBs and,

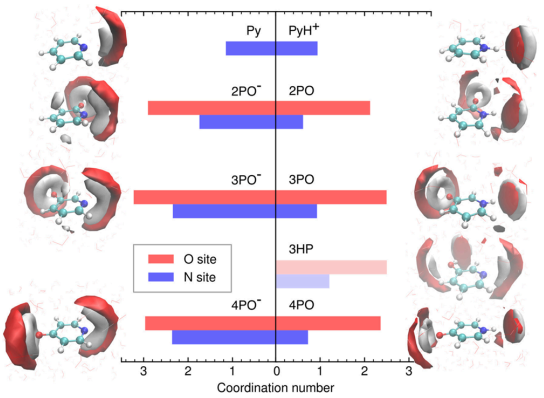

Figure 3. Competition of hydrogen bond coordination to the first aqueous solvation shell between the nitrogen and oxygen heteroatom as a function of distance between these functional sites. Solvent O and H densities are depicted for isovalues of 0.68 and 0.09, respectively. The additional heteroatom of the pyridones (compared to pyridine) enhances the total coordination number, even though the hydration of the nitrogen site is sterically hindered if the heteroatoms are in close proximity. The nonconjugate O^- substituent in $3PO^{(-)}$ leads to additional coordination.

https://dx.doi.org/10.1021/acs.jpcb.0c10873
J. Phys. Chem. B 2021, 125, 2372−2379

instead, the NH group donates approximately 0.7 HB to the solvent.

The second heteroatom in PO/HP leads to an increase of solvent density in the first solvation shell compared to Py(H^+). The solvent structure around the oxygen has the same donutlike shape for all pyridones, and the solvent arrangement at the nitrogen site is similar to that of Py(H^+). The coordination numbers[a] and hydrogen bonding properties, however, differ drastically between the isomers and their protonation states. The comparison of protonated and deprotonated species demonstrates that higher charges always lead to stronger hydrogen bonding interactions.

Within the deprotonated pyridones, the averaged number of accepted hydrogen bonds at the nitrogen site increases with the distance to the oxygen atom, thus from 2PO$^-$ (1.6 HB) to 3PO$^-$ (1.9 HB) to 4PO$^-$ (2.1 HB). The N···H distance is almost constant at 1.8 Å. These observations reveal that the hydration is sterically hindered in the case of close proximity of the two heteroatoms. This finding is in agreement with the enhanced hydration of the oxygen site in 4PO$^-$ compared to that in 2PO$^-$. The coordination number at the oxygen site reaches its maximum for 3PO$^-$ due to the concentration of charge at the O$^-$ substituent, which is not conjugated to the aromatic ring in this isomer. The localized charge enhances hydrogen bond acceptance (3.1 HB) compared to the *para* (2.9 HB) and the sterically disadvantaged ortho isomers (2.8 HB).

Steric hindrance between the two hydrogen bonding sites and the lack of oxygen conjugation in 3PO are the dominating factors for the hydration of the protonated pyridones as well. 3PO exhibits the highest coordination number both at the oxygen and nitrogen sites, followed by 4PO and 2PO. While hydrogen bond donation by the protonated nitrogen site is similar for all isomers (0.6 HB, 1.9 Å; see the Supporting Information), the number of hydrogen bonds that are accepted by the oxygen atom increase from 2PO (1.6) to 4PO (1.7) to 3PO (2.0) with a common distance of 1.7 Å.

Due to the positive charge of PyH$^+$, HBs are more likely (0.7 HB) and contracted (1.8 Å) at the nitrogen site of this molecule. Analogously, HB acceptance by the deprotonated nitrogen atom is reduced in 3HP and Py (0.9 HB, 1.9 Å) compared to that in the anions.

For 3HP, the probability of accepting HBs at the oxygen is reduced to 0.7 due to the bound proton. The hydrogen atom, however, donates approximately 1.5 HBs to water (1.8 Å). The reason for the additionally donated hydrogen bond compared to the N−H case is the more polar O−H bond, as a result of the higher electronegativity of oxygen. The combination of HB donation and acceptance leads to a coordination number at the oxygen site similar to that at 3PO.

The intensity of the solvent−solute interaction as a function of the O$^-$ substitution position can be summarized as follows: the steric hindrance of the solvation increases from the para to the meta to the ortho isomer. 3PO$^{(-)}$ forms additional hydrogen bonds as a result of the nonconjugate C−O$^-$ bond. Thereby, the solvation structure underlines the special significance of 3PO, whose acidity and tautomeric equilibrium differ largely from those of the other isomers.

Solvent Influence on Acidity and Tautomerism. Based on the observations of HB formation and the arrangement of water molecules around the pyridones and Py(H^+), information on the interactions of hydration and the electronic structure can be gained from the NEXAFS. As seen in the CASSCF calculations (see Figure 4b), the π^* resonance position can shift by up to 1.48 eV in the presence of a protic solvent like water.

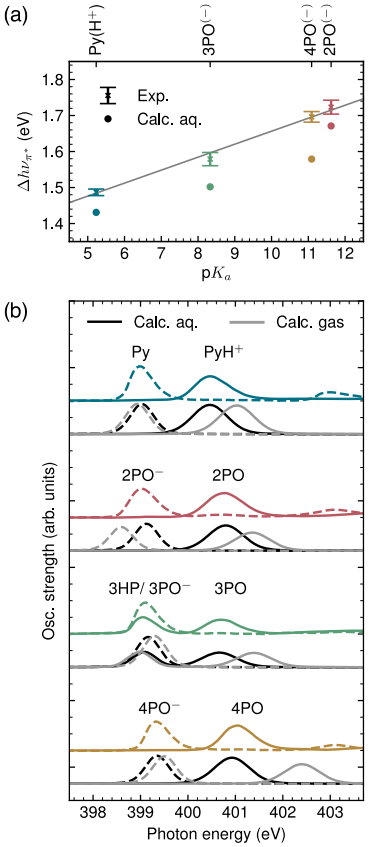

Figure 4. (a) Linear trend of the protonation shift ($\Delta h\nu_{\pi^*}$) and the pyridone acidity (pK_a[6,7]). (b) Comparison of the experimental NEXAFS with the CASSCF spectra for the gas phase and with explicit solvation (details are given in the Methods section) demonstrating that the magnitude of this shift is governed by solvent−solute interactions.

As it is known from the sulfur derivative of 2PO (2-thiopyridone),[34] the core-excitation distorts the solvent−solute interactions, which explains the solvation shifts. According to the equivalent core principle, the effect of a core-hole can be approximated by an increase of the nuclear charge by 1; e.g., core-excited nitrogen (N*) largely behaves like oxygen. Consequently, the polarity of the N*−H bond is increased compared to that of N−H, which strengthens the HB in N−H···OH_2. Therefore, the excitation energy is lowered for the protonated species. The magnitude of the red shift is the smallest for 2PO and the largest for 4PO. These differences are mainly caused by the steric hindrance of hydration if $NH^{\delta+}$ and $O^{\delta-}$ are close together, as observed in the MD simulation of the ground state.

The solvation shifts of the deprotonated species are comparatively small, because the solvent−solute interactions are already strong in the ground state. The additional charge in

https://dx.doi.org/10.1021/acs.jpcb.0c10873
J. Phys. Chem. B 2021, 125, 2372−2379

the excited state destabilizes the hydrogen bonding structure, especially in $2PO^-$, where the LUMO has large contributions at the close-lying $N^{\delta-}$ and $O^{\delta-}$ sites.

Taken together, the response of the solvent−solute interaction to the core-excitation leads to a reduction of the protonation shift $\Delta h\nu_{\pi^*}$ for all species. This shift correlates (within the errors of the measurement) entirely with the acidity of the keto tautomers[b]. The experimentally observed trend is well reproduced by the CASSCF calculations with explicit solvation. Thereby, the computational findings support the abovementioned reasoning that the smaller $\Delta h\nu_{\pi^*}$ is, the stronger the solvent−solute interactions are. Based on the general relation of hydrogen bonding and acidity,[35] it can be stated that the stronger the stabilization of the pyridones by the solvent, the weaker the N−H bond.

It is known from the MD simulations that 3PO has the largest coordination number of all keto forms and that this species also shows a −0.73 eV calculated π^* shift upon solvation (see Figure 4). From this, it becomes apparent why $3PO(^-)$ has the lowest $\Delta h\nu_{\pi^*}$ gap of all pyridones. The strong stabilization of 3PO by the solvent is in agreement with the general assumption that the more polar (keto) tautomer is energetically preferable in aqueous solutions.[36] However, this effect is not only mediated by the macroscopic dielectricity of water, as initially assumed in multiple studies,[7,8,37] but also by hydrogen bonding interactions. Since these interactions diminish for higher temperatures, it can be expected that the equilibrium shifts to the enol form upon heating as observed for 3HP/3PO.[38]

For 2HP/2PO and 4HP/4PO, the higher polarity of the keto form explains why the tautomeric equilibrium is inverted between the gas phase and aqueous solution. In contrast, 3PO does not seem to obey this rule, as it is the most polar form, but coexists with its enol tautomer in water. In fact, due to missing resonance stabilization of the charges in 3PO, it is severely disadvantaged to the point of not being energetically preferable in an aqueous solution even though it is highly stabilized. This interpretation is in agreement with the rule of Zilberg and Dick that the less stable tautomer receives higher stabilization by the aqueous environment.[39] Additionally, the instability of the zwitterionic 3PO explains the higher acidity of 3HP/3PO compared to the other pyridones.

The acidity difference between 2PO and 4PO can be understood, now, as a result of the higher interaction of 4PO with water. The additional stabilization of 4PO agrees with the inverted order of equilibrium constants between vapor $\left(\frac{[4PO]}{[4HP]} < \frac{[2PO]}{[2HP]}\right)$ and aqueous solution $\left(\frac{[4PO]}{[4HP]} > \frac{[2PO]}{[2HP]}\right)$.[36] Analogous to the 3PO case, the more intense 4PO water interactions stabilize this tautomer but cause its protonation state to be more dependent on the solvent. In other words, the abovementioned finding applies: the higher the stabilization by the solvent, the weaker the N−H bond. Since the solvation, in turn, is dependent on the steric hindrance of the hydration and its enhancement by localized charges, it can be stated that these factors control the acidity and tautomerism of pyridones at the same time.

CONCLUSIONS

The amplification of isomeric differences of HP/PO by aqueous hydrogen bonding has been investigated using N K-edge NEXAFS spectroscopy accompanied by systematic CASSCF calculations, distinguishing inherent molecular properties and solvation effects: the dominance of the enol form for all HP/PO isomers in the gas phase is mirrored by minor differences in the electronic structure, especially of the ortho and para isomers in the ground state. The core-excited state reveals first differences dependent on the O^- substitution position and conjugation to the pyridine ring. In aqueous solution, the keto tautomers of 2HP/2PO and 4HP/4PO have been spectroscopically identified as dominating entities, whereas 3PO coexists with the enol form. This is consistent with previous studies in the ultraviolet range of light.

The HP/PO solvation structure has been investigated in detail by MD simulations. The common theme among all molecules considered in this study is their ability to form strong hydrogen bonds with the solvent, both by donating a hydrogen bond to water or by accepting it, and thus stabilizing the molecule. However, in 2PO, a steric hindrance of the hydration reduces the solvent stabilization. In contrast, 3PO receives the highest stabilization due to its zwitterionic character.

The strong interaction between the electronic structure of the pyridones and the surrounding water molecules shows that the increase of solvent stabilization of the keto tautomer from 2PO to 4PO to 3PO, being expressed by the N(1s) → π^* protonation shift, directly correlates with an increase in acidity. It also explains that the tautomeric equilibrium is not only inverted but that the HP form exists as a miniscule fraction for 2HP/2PO and 4HP/4PO upon solvation. 3PO, which does not contain a neutral resonance structure, is energetically so unfavorable that solvent stabilization, even though it is comparatively high, only increases the share of 3PO in aqueous solution to 50%.

The water environment amplifies the tautomeric differences of the pyridone isomers because the intensity of the HB interaction depends both on the localization of charges as a result of the oxygen conjugation and the proximity of the heteroatoms leading to sterical hindrance. Hydrogen bonding not only stabilizes the keto tautomers but also weakens the covalent bond of the proton at the nitrogen site by the same ratio.

These findings clarify the principles of the HP/PO tautomerism and acidity, which have been under investigation for more than 100 years now,[40] and they help to unravel the biological function of nucleobases, vitamin B6, and the pathways of the natural remediation of pyridine.[41]

ASSOCIATED CONTENT

Supporting Information

The Supporting Information is available free of charge at https://pubs.acs.org/doi/10.1021/acs.jpcb.0c10873.

Resonance structures of the pyridone isomers; details of the molecular dynamics simulation (including radial distribution functions, chelpg charges, and hydrogen bonding properties); and TD-DFT calculations (PDF)

Optimized geometries of all discussed species in the gas phase and with explicit solvation in Cartesian coordinates (ZIP)

AUTHOR INFORMATION

Corresponding Authors

Robby Büchner − *Institute of Physics and Astronomy, University of Potsdam, 14476 Potsdam, Germany;*

https://dx.doi.org/10.1021/acs.jpcb.0c10873
J. Phys. Chem. B 2021, 125, 2372−2379

orcid.org/0000-0001-7077-4640;
Email: robby.buechner@helmholtz-berlin.de

Vinícius Vaz da Cruz − *Institute for Methods and Instrumentation for Synchrotron Radiation Research, Helmholtz-Zentrum Berlin für Materialien und Energie, 12489 Berlin, Germany*; Email: vinicius.vaz_da_cruz@helmholtz-berlin.de

Authors

Mattis Fondell − *Institute for Methods and Instrumentation for Synchrotron Radiation Research, Helmholtz-Zentrum Berlin für Materialien und Energie, 12489 Berlin, Germany*

Eric J. Mascarenhas − *Institute of Physics and Astronomy, University of Potsdam, 14476 Potsdam, Germany; Institute for Methods and Instrumentation for Synchrotron Radiation Research, Helmholtz-Zentrum Berlin für Materialien und Energie, 12489 Berlin, Germany*

Annette Pietzsch − *Institute for Methods and Instrumentation for Synchrotron Radiation Research, Helmholtz-Zentrum Berlin für Materialien und Energie, 12489 Berlin, Germany*

Alexander Föhlisch − *Institute of Physics and Astronomy, University of Potsdam, 14476 Potsdam, Germany; Institute for Methods and Instrumentation for Synchrotron Radiation Research, Helmholtz-Zentrum Berlin für Materialien und Energie, 12489 Berlin, Germany*

Complete contact information is available at: https://pubs.acs.org/10.1021/acs.jpcb.0c10873

Notes

The authors declare no competing financial interest.

■ ACKNOWLEDGMENTS

R.B. and A.F. acknowledge funding from the ERC-ADG-2014, Advanced Investigator Grant No. 669531 EDAX under the Horizon 2020 EU Framework Program for Research and Innovation. The authors thank the Helmholtz-Zentrum Berlin for the allocation of synchrotron radiation beamtime. V.V.C acknowledges Sebastian Eckert for fruitful discussions.

■ ADDITIONAL NOTES

[a]The coordination numbers are given with respect to the oxygen atoms of water. The underlying radial distribution functions and more details of the MD simulation (including hydrogen bonding analysis) are provided in the Supporting Information.

[b]Since the π^* shift was calculated for the keto tautomers, the pK_a value of the keto tautomers only has been chosen as a measure for the acidity.

■ REFERENCES

(1) Stanovnik, B.; Tišler, M.; Katritzky, A. R.; Denisko, O. V. *Advances in Heterocyclic Chemistry*, Katritzky, A. R., Ed.; Academic Press: New York, 2006; Vol. *91*, pp 1−134.

(2) Michelson, A. Z.; Petronico, A.; Lee, J. K. 2-Pyridone and derivatives: Gas-phase acidity, proton affinity, tautomer preference, and leaving group ability. *J. Org. Chem.* **2012**, *77*, 1623−1631.

(3) Karelson, M. M.; Katritzky, A. R.; Szafran, M.; Zerner, M. C. Quantitative predictions of tautomeric equilibria for 2-, 3-, and 4-substituted Pyridines in both the gas phase and aqueous solution: Combination of AM1 with reaction field theory. *J. Org. Chem.* **1989**, *54*, 6030−6034.

(4) Beak, P. Energies and alkylations of tautomeric heterocyclic compounds: Old problems−new answers. *Acc. Chem. Res.* **1977**, *10*, 186−192.

(5) Albert, A.; Phillips, J. N. 264. Ionization constants of heterocyclic substances. Part II. Hydroxy-derivatives of nitrogenous six-membered ring-compounds. *J. Chem. Soc.* **1956**, 1294−1304.

(6) Barlin, G. B.; Pfleiderer, W. Ionization constants of heterocyclic substances. Part IX. Protonation of aminopyridones and amino-pyrimidones. *J. Chem. Soc. B* **1971**, 1425−1432.

(7) Metzler, D. E.; Snell, E. E. Spectra and ionization constants of the vitamin B6 group and related 3-Hydroxypyridine derivatives. *J. Am. Chem. Soc.* **1955**, *77*, 2431−2437.

(8) Sánchez-Ruiz, J. M.; Llor, J.; Cortijo, M. Thermodynamic constants for tautomerism and ionization of pyridoxine and 3-Hydroxypyridine in water−dioxane. *J. Chem. Soc., Perkin Trans. 2* **1984**, 2047−2051.

(9) Wondrak, G. T.; Roberts, M. J.; Jacobson, M. K.; Jacobson, E. L. 3-Hydroxypyridine chromophores are endogenous sensitizers of photooxidative stress in human skin cells. *J. Biol. Chem.* **2004**, *279*, 30009−30020.

(10) Kwiatkowski, J.; Pullman, B. *Advances in Heterocyclic Chemistry*, Katritzky, A.; Boulton, A., Eds.; Academic Press: New York, 1975; Vol. *18*, pp 199−335.

(11) Pullman, B.; Pullman, A. *Advances in Heterocyclic Chemistry*, Katritzky, A.; Boulton, A., Eds.; Academic Press: New York, 1971; Vol. *13*, pp 77−159.

(12) Löwdin, P.-O. Proton tunneling in DNA and its biological implications. *Rev. Mod. Phys.* **1963**, *35*, 724−732.

(13) Singh, V.; Fedeles, B. I.; Essigmann, J. M. Role of tautomerism in RNA biochemistry. *RNA* **2015**, *21*, 1−13.

(14) Li, D.; Fedeles, B. I.; Singh, V.; Peng, C. S.; Silvestre, K. J.; Simi, A. K.; Simpson, J. H.; Tokmakoff, A.; Essigmann, J. M. Tautomerism provides a molecular explanation for the mutagenic properties of the anti-HIV nucleoside 5-aza-5,6-dihydro-2'-deoxycytidine. *Proc. Natl. Acad. Sci. U.S.A.* **2014**, *111*, E3252−E3259.

(15) Fondell, M.; Eckert, S.; Jay, R. M.; Weniger, C.; Quevedo, W.; Niskanen, J.; Kennedy, B.; Sorgenfrei, F.; Schick, D.; Giangrisostomi, E.; et al. Time-resolved soft X-ray absorption spectroscopy in transmission mode on liquids at MHz repetition rates. *Struct. Dyn.* **2017**, *4*, No. 054902.

(16) Pietzsch, A.; Eisebitt, S. The UE49 SGM RICXS beamline at BESSY II. *J. Large-Scale Res. Facil.* **2016**, *2*, A54.

(17) Miedema, P. S.; Quevedo, W.; Fondell, M. The variable polarization undulator beamline UE52 SGM at BESSY II. *J. Large-Scale Res. Facil.* **2016**, *2*, A27.

(18) Henke, B. L.; Gullikson, E. M.; Davis, J. C. X-ray interactions: Photoabsorption, scattering, transmission, and reflection at E = 50-30, 000 eV, Z = 1-92. *At. Data Nucl. Data Tables* **1993**, *54*, 181−342.

(19) Flesch, R.; Pavlychev, A. A.; Neville, J. J.; Blumberg, J.; Kuhlmann, M.; Tappe, W.; Senf, F.; Schwarzkopf, O.; Hitchcock, A. P.; Rühl, E. Dynamic stabilization in $1\sigma_u \rightarrow 1\pi_g$ excited nitrogen clusters. *Phys. Rev. Lett.* **2001**, *86*, 3767−3770.

(20) Gillespie, A. W.; Walley, F. L.; Farrell, R. E.; Regier, T. Z.; Blyth, R. I. R. Calibration method at the N *K*-edge using interstitial nitrogen gas in solid-state nitrogen-containing inorganic compounds. *J. Synchrotron Radiat.* **2008**, *15*, 532−534.

(21) Neese, F. The ORCA program system. *Wiley Interdiscip. Rev.: Comput. Mol. Sci.* **2012**, *2*, 73−78.

(22) Breneman, C. M.; Wiberg, K. B. Determining atom-centered monopoles from molecular electrostatic potentials. The need for high sampling density in formamide conformational analysis. *J. Comput. Chem.* **1990**, *11*, 361−373.

(23) Wu, Y.; Tepper, H. L.; Voth, G. A. Flexible simple point-charge water model with improved liquid-state properties. *J. Chem. Phys.* **2006**, *124*, No. 024503.

(24) Barone, V.; Cossi, M. Quantum calculation of molecular energies and energy gradients in solution by a conductor solvent model. *J. Phys. Chem. A* **1998**, *102*, 1995−2001.

(25) Nicolas, C.; Miron, C. Lifetime broadening of core-excited and -ionized states. *J. Electron Spectrosc. Relat. Phenom.* **2012**, *185*, 267−272.

(26) Adamo, C.; Barone, V. Toward reliable density functional methods without adjustable parameters: The PBE0 model. *J. Chem. Phys.* **1999**, *110*, 6158−6170.
(27) Sette, F.; Stöhr, J.; Hitchcock, A. P. Determination of intramolecular bond lengths in gas phase molecules from K shell shape resonances. *J. Chem. Phys.* **1984**, *81*, 4906−4914.
(28) Ito, E.; Oji, H.; Araki, T.; Oichi, K.; Ishii, H.; Ouchi, Y.; Ohta, T.; Kosugi, N.; Maruyama, Y.; Naito, T.; et al. Soft X-ray absorption and X-ray photoelectron spectroscopic study of tautomerism in intramolecular hydrogen bonds of n-Salicylideneaniline derivatives. *J. Am. Chem. Soc.* **1997**, *119*, 6336−6344.
(29) Vaz da Cruz, V.; Ignatova, N.; Couto, R. C.; Fedotov, D. A.; Rehn, D. R.; Savchenko, V.; Norman, P.; Ågren, H.; Polyutov, S.; Niskanen, J.; et al. Nuclear dynamics in resonant inelastic X-ray scattering and X-ray absorption of methanol. *J. Chem. Phys.* **2019**, *150*, No. 234301.
(30) Oji, H.; Mitsumoto, R.; Ito, E.; Ishii, H.; Ouchi, Y.; Seki, K.; Yokoyama, T.; Ohta, T.; Kosugi, N. Core hole effect in NEXAFS spectroscopy of polycyclic aromatic hydrocarbons: Benzene, chrysene, perylene, and coronene. *J. Chem. Phys.* **1998**, *109*, 10409−10418.
(31) Klues, M.; Hermann, K.; Witte, G. Analysis of the near-edge X-ray-absorption fine-structure of anthracene: A combined theoretical and experimental study. *J. Chem. Phys.* **2014**, *140*, No. 014302.
(32) Pagliai, M.; Mancini, G.; Carnimeo, I.; De Mitri, N.; Barone, V. Electronic absorption spectra of pyridine and nicotine in aqueous solution with a combined molecular dynamics and polarizable QM/MM approach. *J. Comput. Chem.* **2017**, *38*, 319−335.
(33) Fileti, E. E.; Coutinho, K.; Malaspina, T.; Canuto, S. Electronic changes due to thermal disorder of hydrogen bonds in liquids: Pyridine in an aqueous environment. *Phys. Rev. E* **2003**, *67*, No. 061504.
(34) Norell, J.; Eckert, S.; Van Kuiken, B. E.; Föhlisch, A.; Odelius, M. Ab initio simulations of complementary K-edges and solvatization effects for detection of proton transfer in aqueous 2-thiopyridone. *J. Chem. Phys.* **2019**, *151*, No. 114117.
(35) Reichardt, C. *Solvents and Solvent Effects in Organic Chemistry*; John Wiley & Sons, Ltd: Weinheim, 2004; pp 5−56; Chapter 2.
(36) Beak, P.; Fry, F. S.; Lee, J.; Steele, F. Equilibration studies. Protomeric equilibria of 2- and 4-hydroxypyridines, 2- and 4-hydroxypyrimidines, 2- and 4-mercaptopyridines, and structurally related compounds in the gas phase. *J. Am. Chem. Soc* **1976**, *98*, 171−179.
(37) Wang, J.; Boyd, R. J. Tautomeric equilibria of Hydroxypyridines in different solvents: An ab initio study. *J. Phys. Chem. A* **1996**, *100*, 16141−16146.
(38) Llor, J.; Asensio, S. B. Thermodynamics of the solution equilibria of 3-hydroxypyridine and pyridoxine in water-dioxane mixtures. *J. Solution Chem.* **1995**, *24*, 1293−1305.
(39) Zilberg, S.; Dick, B. Less stable tautomers form stronger hydrogen bonds: the case of water complexes. *Phys. Chem. Chem. Phys.* **2017**, *19*, 25086−25094.
(40) Baker, F.; Baly, E. C. C. CVI.—The relation between absorption spectra and chemical constitution. Part VII. Pyridine and some of its derivatives. *J. Chem. Soc., Trans.* **1907**, *91*, 1122−1132.
(41) Gupta, N.; O'Loughlin, E. J.; Sims, G. K. *Microbial Metabolism of Xenobiotic Compounds*, Arora, P. K., Ed.; Springer: Singapore, 2019; pp 1−31.

https://dx.doi.org/10.1021/acs.jpcb.0c10873
J. Phys. Chem. B 2021, 125, 2372−2379

Targeting Individual Tautomers in Equilibrium by Resonant Inelastic X-ray Scattering

V. Vaz da Cruz, R. Büchner, M. Fondell, A. Pietzsch, S. Eckert, and A. Föhlisch

Accepted by The Journal of Physical Chemistry Letters (19.01.2022)[†]

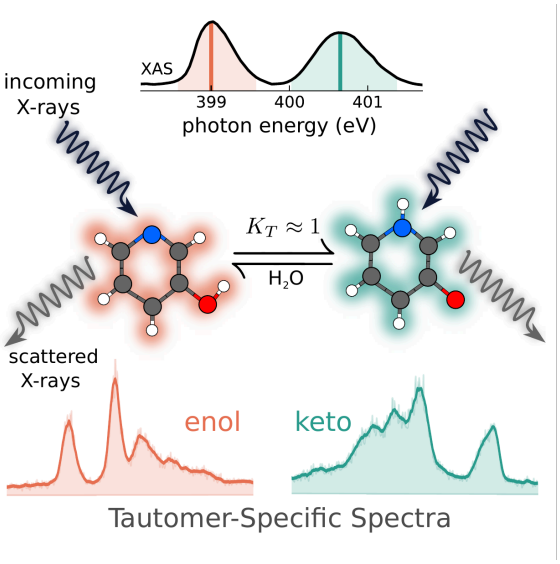

Targeting Individual Tautomers in Equilibrium by Resonant Inelastic X-ray Scattering

Vinícius Vaz da Cruz,*,† Robby Büchner,† Mattis Fondell,† Annette Pietzsch,† Sebastian Eckert,† and Alexander Föhlisch†

†*Helmholtz-Zentrum Berlin für Materialien und Energie GmbH, Institute for Methods and Instrumentation for Synchrotron Radiation Research, 12489 Berlin, Germany.*

‡*Universität Potsdam, Institut für Physik und Astronomie, 14476 Potsdam, Germany.*

Received December 15, 2021; E-mail: vinicius.vaz_da_cruz@helmholtz-berlin.de

Abstract: Tautomerism is one of the most important forms of isomerism, owing to the facile interconversion between species and the large differences in chemical properties introduced by the proton transfer connecting the tautomers. Spectroscopic techniques are often used for characterization of tautomers. In this context, separating the overlapping spectral response of coexisting tautomers is a long standing challenge in chemistry. Here, we demonstrate that by using Resonant Inelastic X-ray Scattering tuned to the core-excited states at the site of proton exchange between tautomers one is able to experimentally disentangle the manifold of valence excited states of each tautomer in a mixture. The technique is applied to the prototypical keto-enol equilibrium of 3-hydroxypyridine in aqueous solution. We detect transitions from the occupied orbitals into the LUMO for each tautomer in solution, which report on intrinsic and hydrogen-bond-induced orbital polarization within the π and σ manifolds at the proton transfer site.

Tautomerism constitutes a form of isomerization involving species that readily interconvert. The most prevalent manifestation of tautomerism is caused by a change in the position of a proton within a molecule, denoted prototropic tautomerism. Although a seemingly subtle change, it imparts decisive modifications in chemical bonding and polarity, consequently defining molecular property and functionality. Tautomerization plays decisive roles in many chemical processes, such as determining the mechanisms of chemical reactions.[1] Its biological importance is reflected in the tautomerism of amino-acids[2,3] that affect the folding of proteins[4] as well as their pocket-binding properties.[5]

Molecules exhibiting tautomerism readily inter-convert, co-existing at a ratio dictated by the tautomeric constant K_T, which depends on a number of parameters, *e.g.* environment polarity and intra- and inter-molecular hydrogen bonding. Apt manipulation of these chemical parameters enables biasing the equilibrium in favour of a given tautomer and, hence, to learn about the properties of each individual species. However, tautomers can also be inseparable, or also exist only as short-lived intermediates, which preclude isolation and a detailed investigation of their properties.

Accessing the electronic structure of individual tautomers in equilibrium has been a long-standing challenge in chemical spectroscopy. Considering traditional UV-Vis absorption spectroscopy, one is often faced with the problem that the lowest $\pi \rightarrow \pi^*$ absorption bands of individual tautomers overlap strongly. Meaning that obtaining their individual spectra experimentally is unfeasible as a rule. In this context, the equilibrium has to be perturbed by creating solvent mixtures, or manipulating the pH so as to detect variations in the spectra, which in turn need to be decomposed by assuming band-shapes and using statistical methods.[6,7]

Here, we propose resonant inelastic X-ray scattering[8] (RIXS) as an elegant solution to this problem. In the RIXS process, the valence electronic excited states of a molecule are reached indirectly, following decay from a resonantly excited intermediate state, in close analogy to resonant Raman spectroscopy. In RIXS, however, the intermediate states are core-excited states which are element specific and highly sensitive to the local chemical environment of individual atoms in a molecule. These attributes have led to insight into the bonding in transition metal complexes,[9] proton-transfer dynamics in organics[10] and hydrogen bonding in liquid water.[11]

We demonstrate the unique capability of RIXS to investigate tautomeric equilibria using the prototypical keto-enol equilibrium of 3-hydroxypyridine (3HP) as a show case. In aqueous solution 3HP exists as a 1:1 mixture of the enol form and the zwitterionic keto form ($K_T = 1.17$[12]). Using RIXS we are able to disentangle the excited state manifold of each individual tautomer, detecting excited states into the XUV region, associated with deep-lying bonding orbitals which shed light on the bonding differences between the species, as well as on the interactions with the solvent, and address the origin of tautomerism at the molecular orbital level.

In Fig. 1a, the keto-enol equilibrium of 3HP is displayed. Although in gas-phase the enolic form is greatly favoured, in aqueous solution the zwitterionic keto form is highly stabilized by hydrogen bonds[13–15] to the point where both structures co-exist in nearly equal proportion.[12] Panel (b) of the same figure, displays the UV-Vis absorption spectrum of the 3HP tautomeric mixture. It can be clearly seen that we have strong overlap between the bands of each species. Underneath the experimental spectra we display a decomposition of the spectrum into components, as proposed in the seminal work of Metzler and Snell.[12]

This decomposition relied on the comparison of the spectra in different solvents, allowing to assign the first and third peaks to the keto form, and the second one to the enol. Although the analysis of the lowest absorption bands allowed for the determination of the equilibrium constant, it bears only limited information on the full electronic structure of the individual tautomeric species. Moreover, the energy range of a typical UV-Vis spectrum is limited both by experimental constraints as well as by the strong solvent absorption background for higher photon energies.

The limitations outlined above may be overcome by utilizing the core-excited states of the system. We shall focus at the N K-edge, specifically, on excitations from the N 1s or-

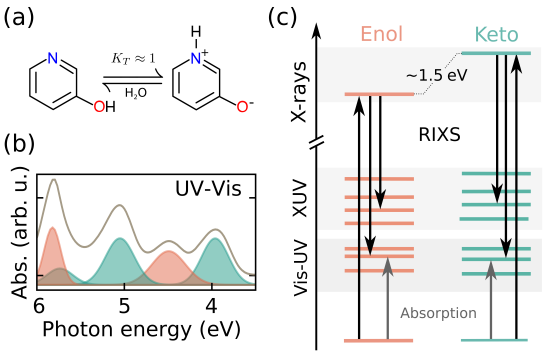

Figure 1. Tautomeric equilibrium in 3-hydroxypyridine and the overlapping spectral response problem. (a) Chemical structure of the species involved in the tautomeric equilibrium of 3-hydroxipyridine (3HP) in aqueous solution ($K_T = 1.17$[12]). (b) UV-Vis absorption spectrum of aqueous 3HP (solid line) and the respective band decomposition scheme[12] shown by shaded areas for the keto (green) and enol (red) forms. (c) Diagram of electronic transitions underlying the UV-Vis absorption and RIXS spectra of 3HP. While the $\pi \rightarrow \pi^*$ energetically overlap, the $1s_N \rightarrow \pi^*$ levels are shifted by about 1.5 eV, allowing to separate the species through resonant excitation.

bital into the LUMO π^* orbital. Such highly excited states, with a hole localized on the nitrogen atom, show a high sensitivity on the chemical environment. Hence, the presence or absence of a proton bound to the nitrogen atom introduces a large chemical shift between the core-excited states of each tautomer.[15] Indeed, the literature abounds with examples discussing the protonation shift of X-ray absorption resonances between species in solution.[10,15–18]

Fig. 1c shows how we use RIXS to exploit the chemical shift of the π^* resonance upon proton transfer between tautomers to yield an experimentally pure spectrum for each species. As shown in the diagram, by tuning the X-ray excitation to each of the well separated core-excited resonances we can detect the emitted photons upon decay to the manifold of final states, which in turn are states with valence excitation character. In this specific case, the RIXS spectrum of each tautomer will contain transitions from the occupied orbital manifold into the LUMO, provided the states have significant N 2p character. Thus we can also observe the electronic changes in the bonding orbitals of the system, and are not limited to only the frontier orbitals. Therefore, we expect to map the local electronic structure of each tautomer at the nitrogen atom, which is one of the proton transfer sites in the hetero-cycle.

The basic experimental framework is depicted in Fig. 2a. The tautomeric mixture in a liquid jet is exposed to an X-ray beam with narrow energy bandwidth as well as a well defined polarization vector. The intensity and energy of the respective scattered photons are subsequently detected. Scanning the incident photon energy across the π^* resonances of each tautomer leads to the two-dimensional map presented in Fig. 2b.

From the 2D RIXS map, it can be clearly seen that we have well defined regions associated with each tautomer. On the top axis of the map, we see the X-ray absorption spectrum showing the two π^* resonances, where the energetically lower one is associated with the enol species and the higher one with the keto species. Since the absorption and emission steps are coupled in RIXS, the same selectivity holds for the scattered photons. It should be noted that such differentiation between species would be absent for other core-level methods *e.g.* non resonant X-ray emission or photo-electron spectroscopy. The resonant emission spectra for each of the tautomers are vertically plotted on the sides of the 2D map in Fig. 2b. These spectra contain information on transitions between occupied molecular orbitals and the LUMO in the energy range up to 20 eV.

We elucidate the electronic differences introduced by the proton transfer connecting both species based on the recorded spectra of each tautomer. The first step is to assign the detected transitions in the spectra to electronic final states reached in the RIXS process. We do so based on two tools: the scattering anisotropy of the RIXS process and time-dependent density functional theory calculations within the restricted subspace approximation[19] (RSA-TD-DFT). The inherent anisotropy of RIXS[20] allows to determine the symmetry of the states present in the spectrum. Considering our experiment, excitation from a 1s orbital into an orbital of π symmetry with a vertically polarized photon leads to enhanced emission intensity from occupied

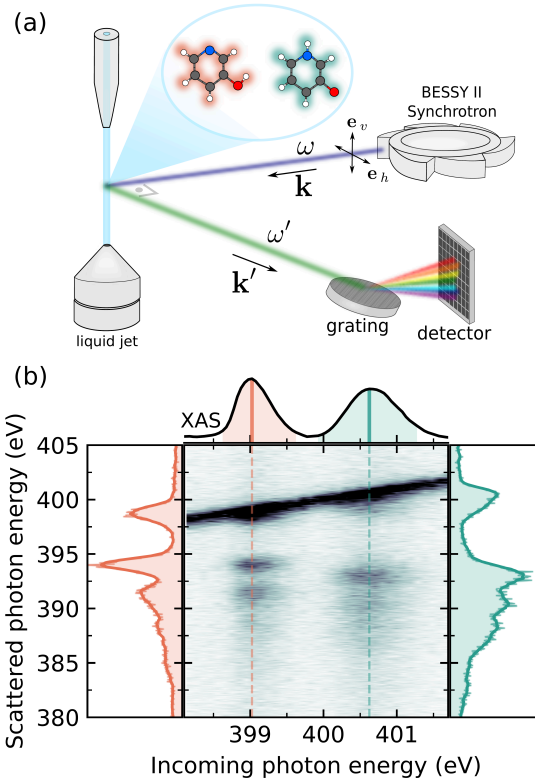

Figure 2. Experimental framework and 2D RIXS map of the tautomeric mixture. (a) Schematic of the experimental framework. (b) Measured RIXS map of aqueous 3-hydroxypyridine. On top the X-ray absorption spectrum showing the separated resonances of each tautomer is shown. The individual spectrum of the enol is shown vertically on the left (399.0 eV excitation energy) and the spectrum of the keto (400.6 eV excitation energy) is shown vertically on the right.

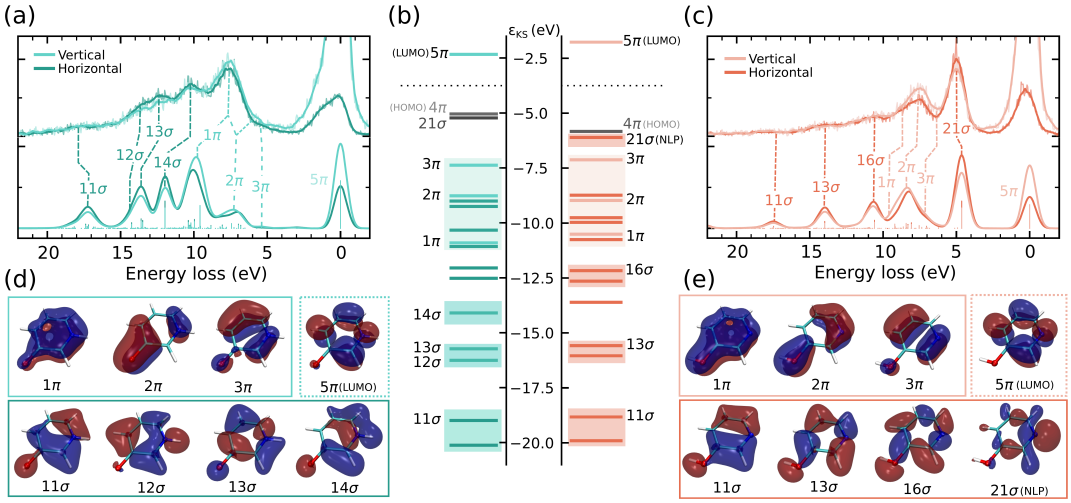

Figure 3. Scattering anisotropy and state assignment of the RIXS spectra of individual tautomers. The experimental and theoretical RIXS spectra of the keto (a) and enol (c) forms of 3-hydroxypyridine for both vertically and horizontally polarized excitation. (b) Kohn-Sham orbital energy diagram highlighting significant orbitals. Relevant orbitals, grouped according to π and σ symmetry, used for assigning the RIXS spectra of the keto (d) and enol (e) forms.

π orbitals. The opposite being true for horizontally polarized excitation, where emission from σ orbitals is enhanced. This allows to assign regions of the RIXS spectrum associated with the π and σ bonding manifolds in a robust way. The experimental and theoretical RIXS spectra for horizontally and vertically polarized X-ray excitation are shown in Fig. 3a,c for each tautomer.

The most prominent difference seen at the N K-edge RIXS spectra of the tautomers is the presence of the intense nitrogen lone-pair (21σ) peak at around 5 eV energy loss, for the enol tautomer as seen in Fig. 3c. This feature is absent in the spectrum of the keto species (Fig. 3a) as in this case the corresponding orbital re-hybridizes and binds covalently to the hydrogen 1s orbital to form the NH bond, which leads to a stabilization of the sigma orbitals. This stabilization is consistent with the fact that 3HP is a weak acid (pK_a = 8.3[21]) with a strong N−H bond. Such an unambiguous signature of the lone-pair orbital has also been observed for deprotonated hetero-cycles.[10,22–24]

The position of the proton induces further effects on the electronic structure of each tautomer, beyond the replacement of a lone-pair by a N−H bond. More precisely, a strong polarization of the occupied orbitals of each tautomer takes place. In general terms, the molecular orbitals in the keto form are polarized towards the nitrogen site, while in the enol form the orbitals are biased towards the oxygen atom. This is a reflection of the intuitive notion that protonation of a given atom increases its ability to accommodate electron density.

Such polarization effects are very evident considering the π manifold of each system, in the energy loss range of 6-10 eV. Specifically, the fully bonding 1π orbital of each system (Fig. 3d,e) shows a clear inversion of polarity between the nitrogen to oxygen atoms. This polarization is directly seen in the RIXS spectra (Fig. 3a,c) where the keto species displays an intense peak associated with the 1π orbital, while the intensity of the same orbital is much smaller in the enolic form, in which the 2π orbital carries most intensity in the π manifold detected in the spectrum.

Analysing the energy loss features beyond 10 eV, we identify transitions associated with the σ bonding manifold, as also evidenced by the scattering anisotropy in both experiment and theory. For the keto form, four features can be distinguished in this region, associated with the delocalized ring orbitals with significant contribution from the N−H moiety. Specifically, orbitals 14σ, 13σ and 12σ in region below 15 eV loss, see Fig. 3a,d. In the range between 15 and 20 eV a weaker feature associated with the deep lying 11σ orbital can be identified. Focusing now on the enol, we observe a considerably weaker intensity associated with the bonding σ peaks. This is further indication of the polarization of these orbitals towards the O−H moiety, and away from the nitrogen atom. Here, transitions from the 16σ and 13σ orbitals are detected in the 10-15 eV range, see Fig. 3c,e. Analagously to the spectrum of the keto, a weaker feature associated with the 11σ orbital is seen in the 15-20 eV energy loss range.

Lastly, it remains to address the role of the solvent on the equilibrium constant and on the electronic structure of each tautomer. The general class of hydroxypyridines exhibit an inversion of the tautomeric equilibrium when substituting an apolar solvent for a polar one.[13,25,26] To further elucidate the role of the solvent we performed QM/MM molecular dynamics simulations. Each tautomeric form of 3HP interacts strongly with the water molecules of the solvent via hydrogen bonds, leading to a manifold of configurations explored by each tautomer within its potential energy basin. Vibrational motion, both thermal and X-ray induced,[27] also plays a role in the formation of the spectrum. These aspects are not easily separable in the experimental data, therefore we need to investigate how each mechanism affects the peak positions, lineshapes, and intensity ratios in the spectra.

Starting with the XAS, Fig. 4 compares the effect of the core-hole lifetime broadening, the vibronic substructure, and the impact of solvation and thermal vibrations on peak width and position. As it can be seen, the width of the XAS

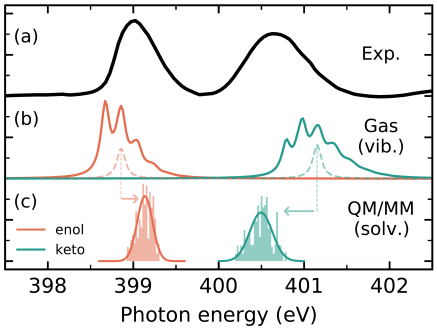

Figure 4. Effect of vibrational motion and solvation on the XAS spectral lineshape. (a) The experimental XAS spectrum. (b) Calculated Franck-Condon profiles, in the gas-phase, for each tautomer. The dashed lines show the absorption resonances including only the core-hole lifetime broadening ($\Gamma_N = 0.12$ eV, FWHM). (c) Calculated histograms of transition energies, weighted by their respective absorption intensity, sampled from the QM/MM MD simulations. From this analysis we extract a tautomeric constant of $K_T = 1.08$.

resonances is dominated by the Franck-Condon progression of the modes active upon core-excitation. However, no fine-structure is seen in the experimental data due to the effect of solvation, which induces an additional broadening of the lines. We determined the solvation broadenings to be 0.21 eV (enol) and 0.31 eV (keto) from the histograms of transition energies, weighted by the absorption intensities, as shown in Fig. 4c. In contrast, the vibrational broadenings (including the core-hole lifetime broadening) are estimated to be 0.96 eV (enol) and 1.10 eV (keto). Broadenings are given as full-width at half-maximum values. Using the computed lineshapes, we extracted the tautomerization constant of 3HP from the ratio of the XAS peaks to be $K_T = 1.08 \pm 0.02$ (see Supporting Information), which is in good agreement with the values of Metzler and Snell [12] ($K_T = 1.17$), Sánchez-Ruiz et al. [25] ($K_T = 1.10$) and Llor and Asensio [26] ($K_T = 1.06$).

In our case, the tautomers are in chemical equilibrium. Hence, we observe a signal arising from the statistical distribution of proton positions around the potential energy basin minimum of each system, as consequence of the fluctuations of the hydrogen bond network around the nitrogen and oxygen sites. In cases of photo-induced tautomerism, the molecular vibrations can be mapped in real time, through the oscillation of the position of the X-ray absorption lines, as demonstrated by Loe et al.. [28]

Although the XAS lines are only modestly broadened by solvation, they are substantially shifted from the gas-phase resonance positions. [15] The shift is inverse for the two tautomers, namely a blue shift is seen for the enol form and a red shift for the keto form. Indicating that hydrogen bonding reduces electron density at the nitrogen site for the enol, and increases it for the keto form. However, XAS is only an indirect measure of this effect, since we probe unoccupied states. Hence, by turning to the RIXS transitions we may disentangle the origins of the changes in electron density distribution induced by solute-solvent interactions with molecular orbital specificity.

We can begin to uncover the detailed effects of hydrogen bonding by looking at the solvent distribution density plots in Fig. 5a,b. As expected, an inversion of polarity in the solvation shell of each tautomer at the nitrogen site takes place. Moreover, it can be seen that solvation at the oxo site of the keto form is largely enhanced when compared to the hydroxyl group in the enol tautomer. This helps to explain the drastic stabilization of the keto form of the pyridones in aqueous solution. [13,15]

To clearly identify the effect of hydrogen bonding on the spectral observables, we calculated average RIXS spectra for each tautomer based on sampled configurations from the QM/MM MD trajectory. The spectra are shown in Fig. 5c,d, where they are also compared to calculations in gas-phase. To link the observed changes in peak positions and intensity ratios seen in the theoretical simulations to the experimental RIXS spectra, we analysed the charge density difference plots considering an idealized solvated cluster for each tautomer, based on the microsolvation structures derived from the MD. The plots are shown in Fig. 5e,f.

For the keto, σ density increases at the nitrogen while it decreases at the hydrogen. This is caused by the donated hydrogen bond to the water molecule, which increases the polarity of the N−H bond by decreasing electron density at the hydrogen. In contrast, π electron density is lost at

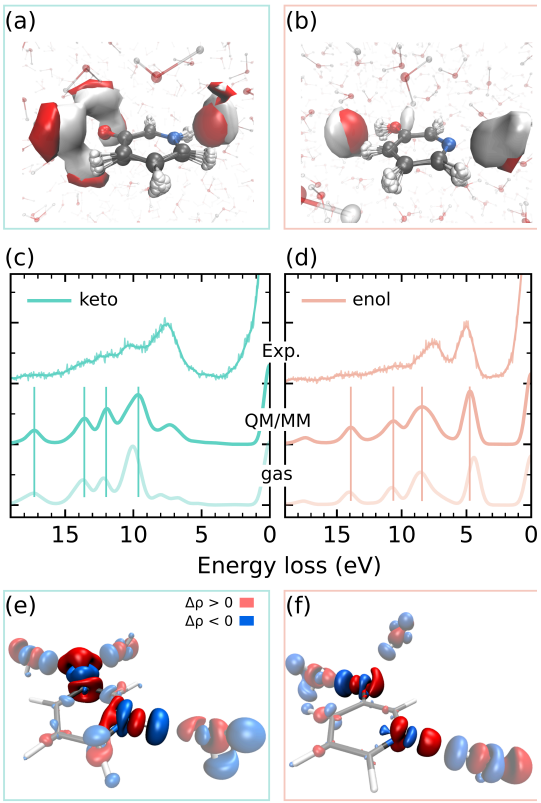

Figure 5. Hydrogen bonding effects on orbital polarization seen in the RIXS spectra. Solvent oxygen (red) and hydrogen (gray) mass-density distributions along with solute geometric distortions sampled from the QM/MM MD simulatons for the keto (a) and enol (b) tautomers. Comparison between experiment and theoretical RIXS spectra, for vertically polarized excitation, computed from sampled snapshots from the MD as well as for the molecules in gas-phase (c, d). Electron density difference ($\Delta\rho$) for an idealized solvated cluster with respect to the molecule in vaccum for the keto (e) and enol (f) tautomers.

the nitrogen site, while it is accumulated at the C=O bond (Fig. 5e). This solvent-induced orbital polarization is nicely reflected on the spectral simulations, which show that the relative intensity between the peak of the π manifold and the σ is reduced when comparing the gas-phase and the explicitly solvated spectra in Fig. 5c. The intensity difference is also accompanied by a 0.38 eV red shift of the π peak with respect to the gas-phase.

For the enol, we observe opposite trends. Specifically, a decrease of σ density at the nitrogen takes place due to the accepted hydrogen bond from a water molecule (Fig. 5f). Synergetically, an increase in π density occurs. Moreover, the solvation at the oxygen site creates a much less pronounced electron density reorganization in the enol tautomer, when compared to the keto form. The shifts in electron density in the π and σ manifold are also well captured in the RIXS spectra in Fig. 5d, where we see an increase of the π peak with respect to the nitrogen lone-pair peak. We also see a 0.30 eV blue shift of the lone pair peak with respect to the gas-phase.

Molecular polarity and tautomerism are inextricably linked, as pointed out very early on by Lewis.[29] Polar chemical bonds result from the imbalance in the capacity of different atoms to attract the electrons in the molecule to their vicinity. The very fundamental reason for the existence of multiple tautomeric species of a given chemical compound stems from the shifts in polarity in the molecule, which in turn directly affects their relative thermodynamic stability. This is further evidenced by the extreme influence of solvent polarity on tautomeric equilibria. Hence, the ability to experimentally dissect molecular polarity in terms of the concept of molecular orbitals is extremely powerful.

The example case of 3HP demonstrates how a technique capable of separating the overlapping spectral response of the tautomers yield new insights into electronic structure changes and orbital re-hybridization introduced by the change in proton position. The association of RIXS intensities with the amplitude of bonding orbitals at a given the elemental site is an inherent feature of X-ray spectroscopy, as a projected density of states is probed. Such projection of molecular orbitals on atomic sites, by element specific X-ray excitation, has been used, for instance, to quantify covalent interactions in transition metal complexes.[30,31] In the specific case discussed here, the projection of the orbitals on the nitrogen site, one of the proton center sites, we are able to experimentally derive the change in electron density upon tautomerization and solvation.

The ability to assess the nitrogen 2p character of the bonding orbitals, combined with the symmetry assignment provided by the scattering anisotropy, enabled several interesting insights to be extracted. Notably, the lowest bonding π orbital which although fully delocalized in both tautomers, in the keto form is heavily biased to the nitrogen, while it is biased towards the oxygen in the enol form. A similar trend is seen for the σ bonding orbitals, the RIXS intensity of such states is higher for the keto form, indicating large amplitude at the nitrogen. They are, however, weaker in the enol form, indicating a polarity towards the oxygen. Such observation is consistent with the fact that the enol form is dominant in gas-phase, since electron density accumulates at the more electro-negative oxygen atom. This inherent picture is distorted once hydrogen bonding is accounted for. In this case, the considerably stronger interactions with the keto form lead to significant rehybridization at the nitrogen site, while the enol form is only modestly affected.

The effects discussed above have only been indirectly derived[1] or theoretically discussed.[32–35] The comprehensive review of Raczyńska et al.[1] extensively highlights the link between electron delocalization and polarization and the position of the tautomeric equilibrium. Notably, Sato et al.[34] discussed the concept of "electronic structure distortion" by solvation, to explain the inversion of the tautomeric equilibrium in 2-Pyridone when going from gas-phase to aqueous solution. In that study, it was found by energy decomposition that the stabilization of the ketone is due to strong rehybridization of the orbitals at the hydrogen bonding sites. Our analysis for the 3HP isomer, supports their notion with the added sensitivity of being able to experimentally disentangle the σ and π bonding manifolds of each system. Here, it becomes clear that future studies where an experimental comparison of the same equilibrium in gas-phase, apolar solvents and polar ones will be able to track the electronic changes induced by the medium.

Generally, the large chemical shift of the XAS associated with proton transfer provides great selectivity in the RIXS spectra of prototropic tautomeric mixtures. Hence, we expect applicability to a wide range of systems, beyond the showcase of 3HP. Nevertheless, it should be noted that difficulties can arise on a system-specific basis. Explicitly, in the case where XAS resonances overlap, either completely or partially. In the less likely case of complete overlap, happening when the different tautomers exhibit chemically equivalent sites, selectivity would be drastically reduced. Here, the RIXS signal of the individual species would also overlap, requiring decomposition schemes to be applied. In the more probable case of only partial overlap, the concept of excitation energy detuning can be used to alter the relative contribution of the underlying species to the total signal by exciting on the blue or red flanks of the absorption resonances. Thereby enabling at least partial recovery of the selectivity. Alternatively, even if the resonances overlap at a given elemental edge, the use of complementary elemental edges[28] provides further options to target the individual tautomeric forms.

In conclusion, we have established resonant inelastic X-ray scattering as a technique to separate the overlapping electronic structure of tautomers in equilibrium. The large protonation shift associated with the proton transfer at the isomerization site leads to well separated resonances that can be excited selectively. The resulting spectra on the energy loss scale contain information on excitations from the occupied manifold into the LUMO of each system, all the while the intensities of each band report on the atomic character of a given occupied orbital, in the case presented here at the nitrogen site. The symmetry of the states could be experimentally determined via the scattering anisotropy. Combining the experimental results with QM/MM MD simulations and RSA-TD-DFT spectral calculations, we were able to asses the intrinsic orbital polarization of the occupied manifold of each tautomer, as well as the additional polarization induced by hydrogen bonding. The experimental scheme described here can be expected to be applicable to a wide range of systems, and could lead to deeper insights into how the orbital polarization introduced by the proton transfer as well as interactions with the solvent determines the position of the equilibrium between tautomers.

Experiment Methods The experiments were carried out

at the the BESSY II Synchrotron facility. The X-ray absorption measurements were carried out using the nmTransmission NEXAFS endstation[36] at the UE52-SGM,[37] and the X-ray absorption spectra have been originally published by Büchner et al..[15] The RIXS measurements were performed at the UE49-SGM[38] beamline using the EDAX[39] endstation. The 3-hydroxypyridine (3HP) sample was purchased from Sigma-Aldrich with a minimum purity of 95% and dissolved in de-ionized water to yield a 75 mM solution. The experimental RIXS endstation is discussed in detail by Kunnus et al..[39] In short, the sample was delivered into the experimental vacuum chamber using a round liquid jet system of 20 - 30 μm diameter. The solution was refreshed at a rate of 1.3 mL/min. It was excited using horizontally and vertically polarized synchrotron radiation at the nitrogen 1s absorption resonances of the two tautomers with a bandwidth of 0.2 eV. The scattered photons were dispersed with respect to their energy and detected under a 90° angle using a modified Scienta XES 350 Rowland type spectrometer.

Computational Methods All electronic structure calculations were carried out with the ORCA package.[40] The RIXS scattering amplitudes were computed within the RSA-TD-DFT method described by Vaz da Cruz et al..[19] Transition moments were computed based on the linear response amplitudes,[41] using the Multiwfn[42] program. Spectral calculations used the PBE exchange and correlation functional and the def2-TZVP(-f) basis set.[43]

To model the micro-solvation of each tautomer Quantum Mechanics/Molecular Mechanics Molecular Dynamics (QM/MM MD) simulations were performed. The simulations used the NAMD/ORCA interface[44] where ORCA[40] was used to compute the quantum mechanical forces of the solute molecules and NAMD[45,46] was used for the time propagation of the classical water molecules. The quantum-mechanical region was comprised of only the solute molecule, treated at the B3LYP/def2-TZVP(-f) level using the RIJ-COSX approximation,[47] while the solvent molecules were modelled via the classical TIP3P force field. From the simulations uncorrelated snapshots were taken for analysis of the solvation via radial distribution functions and to compute the XAS and RIXS spectra. Further details are available in the Supporting Information.

Acknowledgement We thank the Helmholtz-Zentrum Berlin for the allocation of synchrotron radiation beamtime. A.F. acknowledges funding from the ERC-ADG-2014 Advanced Investigator Grant no. 669531 EDAX under the Horizon 2020 EU Framework, Programme for Research and Innovation.

Supporting Information Available Details of the theoretical spectral calculations, details of the molecular dynamics simulations, tautomeric constant extraction.

References

(1) Raczyńska, E. D.; Kosińska, W.; Ośmiałowski, B.; Gawinecki, R. Tautomeric Equilibria in Relation to Pi-Electron Delocalization. *Chem. Rev.* **2005**, *105*, 3561–3612.
(2) Munowitz, M.; Bachovchin, W.; Herzfeld, J.; Dobson, C.; Griffin, R. Acid-Base and Tautomeric Equilibria in the Solid State: Nitrogen-15 NMR Spectroscopy of Histidine and Imidazole. *J. Am. Chem. Soc.* **1982**, *104*, 1192–1196.
(3) Li, S.; Hong, M. Protonation, Tautomerization, and Rotameric Structure of Histidine: A Comprehensive Study by Magic-Angle-Spinning Solid-State NMR. *J. Am. Chem. Soc.* **2011**, *133*, 1534–1544.
(4) Hansen, A. L.; Kay, L. E. Measurement of Histidine pKa Values and Tautomer Populations in Invisible Protein States. *Proc. Natl. Acad. Sci. U.S.A.* **2014**, *111*, E1705–E1712.
(5) Weinstein, H.; Chou, D.; Johnson, C. L.; Kang, S.; Green, J. P. Tautomerism and the Receptor Action of Histamine: A Mechanistic Model. *Mol. Pharmacol.* **1976**, *12*, 738–745.
(6) Antonov, L.; Nedeltcheva, D. Resolution of Overlapping UV–Vis Absorption Bands and Quantitative Analysis. *Chem. Soc. Rev.* **2000**, *29*, 217–227.
(7) Antonov, L. *Tautomerism: Methods and Theories*; John Wiley & Sons, 2013.
(8) Gel'mukhanov, F.; Odelius, M.; Polyutov, S. P.; Föhlisch, A.; Kimberg, V. Dynamics of Resonant X-ray and Auger Scattering. *Rev. Mod. Phys.* **2021**, *93*, 035001.
(9) Biasin, E.; Nascimento, D. R.; Poulter, B. I.; Abraham, B.; Kunnus, K.; Garcia-Esparza, A. T.; Nowak, S. H.; Kroll, T.; Schoenlein, R. W.; Alonso-Mori, R.; Khalil, M.; Govind, N.; Sokaras, D. Revealing the Bonding of Solvated Ru Complexes with Valence-to-Core Resonant Inelastic X-ray Scattering. *Chem. Sci.* **2021**, *12*, 3713–3725.
(10) Eckert, S. et al. Ultrafast Independent NH and NC Bond Deformation Investigated with Resonant Inelastic X-Ray Scattering. *Angew. Chem., Int. Ed.* **2017**, *56*, 6088–6092.
(11) Vaz da Cruz, V. et al. Probing Hydrogen Bond Strength in Liquid Water by Resonant Inelastic X-ray Scattering. *Nat. Commun.* **2019**, *10*, 1013.
(12) Metzler, D. E.; Snell, E. E. Spectra and Ionization Constants of the Vitamin B6 Group and Related 3-Hydroxypyridine Derivatives. *J. Am. Chem. Soc.* **1955**, *77*, 2431–2437.
(13) Beak, P.; Fry, F. S.; Lee, J.; Steele, F. Equilibration Studies. Protomeric Equilibria of 2- and 4-Hydroxypyridines, 2- and 4-Hydroxypyrimidines, 2- and 4-Mercaptopyridines, and Structurally Related Compounds in the Gas Phase. *J. Am. Chem. Soc.* **1976**, *98*, 171–179.
(14) Beak, P. Energies and Alkylations of Tautomeric Heterocyclic Compounds: Old Problems–New Answers. *Acc. Chem. Res.* **1977**, *10*, 186–192.
(15) Büchner, R.; Fondell, M.; Mascarenhas, E. J.; Pietzsch, A.; Vaz da Cruz, V.; Föhlisch, A. How Hydrogen Bonding Amplifies Isomeric Differences in Pyridones toward Strong Changes in Acidity and Tautomerism. *J. Phys. Chem. B* **2021**, *125*, 2372–2379.
(16) Eckert, S.; Miedema, P.; Quevedo, W.; O'Cinneide, B.; Fondell, M.; Beye, M.; Pietzsch, A.; Ross, M.; Khalil, M.; Föhlisch, A. Molecular Structures and Protonation State of 2-Mercaptopyridine in Aqueous Solution. *Chem. Phys. Lett.* **2016**, *647*, 103 – 106.
(17) Nolting, D.; Aziz, E. F.; Ottosson, N.; Faubel, M.; Hertel, I. V.; Winter, B. pH-Induced Protonation of Lysine in Aqueous Solution Causes Chemical Shifts in X-ray Photoelectron Spectroscopy. *J. Am. Chem. Soc.* **2007**, *129*, 14068–14073.
(18) Ekimova, M.; Quevedo, W.; Szyc, ; Iannuzzi, M.; Wernet, P.; Odelius, M.; Nibbering, E. T. J. Aqueous Solvation of Ammonia and Ammonium: Probing Hydrogen Bond Motifs with FT-IR and Soft X-ray Spectroscopy. *J. Am. Chem. Soc.* **2017**, *139*, 12773–12783.
(19) Vaz da Cruz, V.; Eckert, S.; Föhlisch, A. TD-DFT Simulations of K-edge Resonant Inelastic X-ray Scattering Within the Restricted Subspace Approximation. *Phys. Chem. Chem. Phys.* **2021**, *23*, 1835–1848.
(20) Gel'mukhanov, F.; Ågren, H. Resonant Inelastic X-ray Scattering with Symmetry-Selective Excitation. *Phys. Rev. A* **1994**, *49*, 4378–4389.
(21) Barlin, G. B.; Pfleiderer, W. Ionization Constants of Heterocyclic Substances. Part IX. Protonation of Aminopyridones and Aminopyrimidones. *J. Chem. Soc. B* **1971**, 1425–1432.
(22) Eckert, S.; Vaz da Cruz, V.; Ochmann, M.; von Ahnen, I.; Föhlisch, A.; Huse, N. Breaking the Symmetry of Pyrimidine: Solvent Effects and Core-Excited State Dynamics. *J. Phys. Chem. Lett.* **2021**, *12*, 8637–8643.
(23) Eckert, S.; Niskanen, J.; Jay, R. M.; Miedema, P. S.; Fondell, M.; Kennedy, B.; Quevedo, W.; Iannuzzi, M.; Föhlisch, A. Valence Orbitals and Local Bond Dynamics around N Atoms of Histidine under X-ray Irradiation. *Phys. Chem. Chem. Phys.* **2017**, *19*, 32091–32098.
(24) Meyer, F.; Blum, M.; Benkert, A.; Hauschild, D.; Jeyachandran, Y. L.; Wilks, R. G.; Yang, W.; Bär, M.; Reinert, F.; Heske, C.; Zharnikov, M.; Weinhardt, L. Site-Specific Electronic Structure of Imidazole and Imidazolium in Aqueous Solutions. *Phys. Chem. Chem. Phys.* **2018**, *20*, 8302–8310.
(25) Sánchez-Ruiz, J. M.; Llor, J.; Cortijo, M. Thermodynamic constants for tautomerism and ionization of pyridoxine and 3-Hydroxypyridine in water–dioxane. *J. Chem. Soc., Perkin Trans. 2* **1984**, 2047–2051.
(26) Llor, J.; Asensio, S. B. Thermodynamics of the Solution Equilibria of 3-Hydroxypyridine and Pyridoxine in Water-Dioxane Mixtures. *J. Sol. Chem.* **1995**, *24*, 1293–1305.
(27) Vaz da Cruz, V. et al. Nuclear Dynamics in Resonant Inelastic X-ray Scattering and X-ray Absorption of Methanol. *J. Chem. Phys.* **2019**, *150*, 234301.
(28) Loe, C. M.; Liekhus-Schmaltz, C.; Govind, N.; Khalil, M. Spectral Signatures of Ultrafast Excited-State Intramolecular Proton Transfer from Computational Multi-edge Transient X-ray Absorption Spectroscopy. *J. Phys. Chem. Lett.* **2021**, *12*, 9840–

9847.
(29) Lewis, G. N. Valence and Tautomerism. *J. Am. Chem. Soc.* **1913**, *35*, 1448–1455.
(30) Kroll, T.; Baker, M. L.; Wilson, S. A.; Lundberg, M.; Juhin, A.; Arrio, M.-A.; Yan, J. J.; Gee, L. B.; Braun, A.; Weng, T.-C.; Sokaras, D.; Hedman, B.; Hodgson, K. O.; Solomon, E. I. Effect of 3d/4p Mixing on 1s2p Resonant Inelastic X-ray Scattering: Electronic Structure of Oxo-Bridged Iron Dimers. *J. Am. Chem. Soc.* **2021**, *143*, 4569–4584.
(31) Baker, M. L.; Mara, M. W.; Yan, J. J.; Hodgson, K. O.; Hedman, B.; Solomon, E. I. K- and L-edge X-ray Absorption Spectroscopy (XAS) and Resonant Inelastic X-ray Scattering (RIXS) Determination of Differential Orbital Covalency (DOC) of Transition Metal Sites. *Coord. Chem. Rev.* **2017**, *345*, 182–208.
(32) Wong, M. W.; Wiberg, K. B.; Frisch, M. J. Solvent Effects. 3. Tautomeric Equilibria of Formamide and 2-Pyridone in the Gas Phase and Solution: an ab initio SCRF Study. *J. Am. Chem. Soc.* **1992**, *114*, 1645–1652.
(33) Barone, V.; Adamo, C. Density Functional Study of Intrinsic and Environmental Effects in the Tautomeric Equilibrium of 2-Pyridone. *J. Phys. Chem.* **1995**, *99*, 15062–15068.
(34) Sato, H.; Hirata, F.; Sakaki, S. Distortion of Electronic Structure in Solvated Molecules: Tautomeric Equilibrium of 2-Pyridone and 2-Hydroxypridine in Water Studied by the RISM-SCF Method. *J. Phys. Chem. A* **2004**, *108*, 2097–2102.
(35) Zilberg, S.; Dick, B. Less Stable Tautomers Form Stronger Hydrogen Bonds: The Case of Water Complexes. *Phys. Chem. Chem. Phys.* **2017**, *19*, 25086–25094.
(36) Fondell, M. et al. Time-Resolved Soft X-ray Absorption Spectroscopy in Transmission Mode on Liquids at MHz Repetition Rates. *Struct. Dyn.* **2017**, *4*, 054902.
(37) Miedema, P. S.; Quevedo, W.; Fondell, M. The Variable Polarization Undulator Beamline UE52 SGM at BESSY II. *Journal of Large-Scale Research Facilities* **2016**, *2*, A27.
(38) Pietzsch, A.; Eisebitt, S. The UE49 SGM RICXS Beamline at BESSY II. *Journal of Large-Scale Research Facilities* **2016**, *2*, A54.
(39) Kunnus, K. et al. A Setup for Resonant Inelastic Soft X-ray Scattering on Liquids at Free Electron Laser Light Sources. *Rev. Sci. Instrum.* **2012**, *83*, 123109.
(40) Neese, F. The ORCA Program System. *Wiley Interdiscip. Rev. Comput. Mol. Sci.* **2012**, *2*, 73–78.
(41) Nascimento, D. R.; Biasin, E.; Poulter, B. I.; Khalil, M.; Sokaras, D.; Govind, N. Resonant Inelastic X-ray Scattering Calculations of Transition Metal Complexes Within a Simplified Time-Dependent Density Functional Theory Framework. *J. Chem. Theory Comput.* **2021**, *17*, 3031–3038.
(42) Lu, T.; Chen, F. Multiwfn: A Multifunctional Wavefunction Analyzer. *J. Comput. Chem.* **2012**, *33*, 580–592.
(43) Weigend, F.; Ahlrichs, R. Balanced Basis Sets of Split Valence, Triple Zeta Valence and Quadruple Zeta Valence Quality for H to Rn: Design and Assessment of Accuracy. *Phys. Chem. Chem. Phys.* **2005**, *7*, 3297–3305.
(44) Melo, M. C.; Bernardi, R. C.; Rudack, T.; Scheurer, M.; Riplinger, C.; Phillips, J. C.; Maia, J. D.; Rocha, G. B.; Ribeiro, J. V.; Stone, J. E., et al. NAMD Goes Quantum: An Integrative Suite for Hybrid Simulations. *Nat. Methods* **2018**, *15*, 351–354.
(45) Phillips, J. C. et al. Scalable Molecular Dynamics on CPU and GPU Architectures with NAMD. *J. Chem. Phys.* **2020**, *153*, 044130.
(46) Ribeiro, J. V.; Bernardi, R. C.; Rudack, T.; Stone, J. E.; Phillips, J. C.; Freddolino, P. L.; Schulten, K. QwikMD — Integrative Molecular Dynamics Toolkit for Novices and Experts. *Sci. Rep.* **2016**, *6*, 1–14.
(47) Neese, F.; Wennmohs, F.; Hansen, A.; Becker, U. Efficient, Approximate and Parallel Hartree-Fock and Hybrid DFT Calculations. A Chain-of-Spheres-Algorithm for the Hartree-Fock Exchange. *Chem. Phys.* **2009**, *356*, 98 – 109.

The porphyrin center as a regulator for metal–ligand covalency and π hybridization in the entire molecule

R. Büchner, M. Fondell, R. Haverkamp, A. Pietzsch, V. Vaz da Cruz, and A. Föhlisch

Phys. Chem. Chem. Phys., 2021,23, 24765-24772[‡]

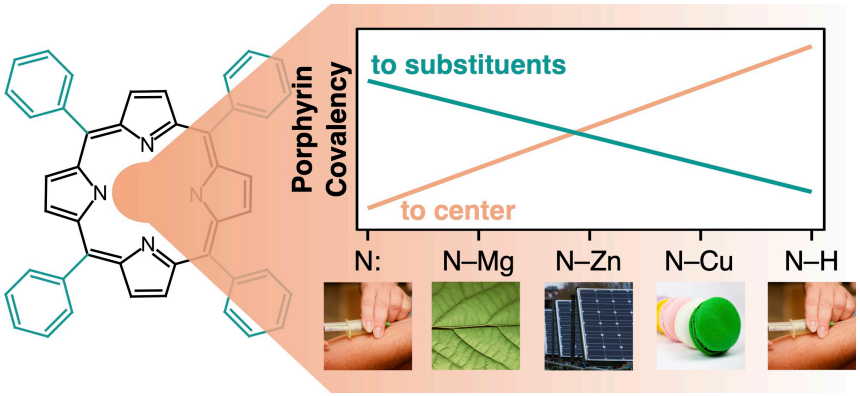

The porphyrin center is shown to control both the covalency of the central complex and π hybridization with peripheral substituents.

[‡]Reproduced from ***Phys. Chem. Chem. Phys.***, 2021,**23**, 24765-24772 with permission from the PCCP Owner Societies. (CC BY 3.0)

PCCP

ROYAL SOCIETY OF CHEMISTRY

PAPER

View Article Online
View Journal | View Issue

Cite this: *Phys. Chem. Chem. Phys.*, 2021, **23**, 24765

The porphyrin center as a regulator for metal–ligand covalency and π hybridization in the entire molecule†

Robby Büchner, *[a] Mattis Fondell, [b] Robert Haverkamp, [b] Annette Pietzsch, [b] Vinícius Vaz da Cruz *[b] and Alexander Föhlisch [ab]

Received 27th August 2021,
Accepted 5th October 2021

DOI: 10.1039/d1cp03944j

rsc.li/pccp

The central moiety of porphyrins is shown to control the charge state of the inner complex and links it by covalent interaction to the peripheral substituents. This link, which enables the versatile functions of porphyrins, is not picked up in the established, reduced four orbital picture [Gouterman, *J. Mol. Spectrosc.*, 1961, **6**, 138]. X-ray absorption spectroscopy at the N K-edge with density functional theory approaches gives access to the full electronic structure, in particular the π* manifold beyond the Gouterman orbitals. Systematic variation of the central moiety highlights two linked, governing trends: The ionicity of the porphyrin center increases from the aminic N–H to N–Cu to N–Zn to N–Mg to the iminic N:. At the same time covalency with peripheral substituents increases and compensates the buildup of high charge density at the coordinated nitrogen sites.

1 Introduction

While the class of porphyrins and derivatives is of versatile use and of significant importance both in nature and technology, each function is fulfilled by a porphyrin with particular constitution: protoporphyrin IX, for instance, contains a center of two hydrogen atoms, which are replaced by magnesium in plants to form chlorophyll or iron in vertebrates to form haeme. Upon iron deficiency zinc protoporphyrin is synthesized by the body, instead, leading to anemia.[1] If the human porphyrin metabolism is substantially impaired, protoporphyrin IX accumulates in the body causing photoallergy and hepatic disease.[2] Analogously to the necessity for an iron center in heame, the magnesium center of chlorophyll is essential for light-harvesting in plants. For the technical imitation of photosynthesis, however, copper[3] or zinc[4] are used as central atoms, since isolated chlorophyll easily disintegrates.[5] In contrast, the high stability of copper chlorophyllins allows their application in the food industry,[6] catalysis,[7] and medicine.[8] The use of chlorophyllins is also supported by their high aqueous solubility. The ability of porphyrins and derivatives to dissolve in polar solvents, bind to synthetic surfaces or proteins in a specific geometric arrangement are governed by the peripheral substituents which differ for each before mentioned application in addition to the central moiety.

Considering the vast variety of porphyrins, it is remarkable that all of them show similar optical properties (see UV/VIS spectra in the ESI†). The strong UV (Soret or B band) and weaker visible (Q) bands of all porphyrins have been explained by π–π* transitions from the two highest occupied molecular orbitals (HOMO, HOMO−1 – see Fig. 1a) to the two lowest unoccupied molecular orbitals (LUMO, LUMO+1) by Gouterman in Gouterman 1961.[9] This four orbital model explains the intensity differences and the splitting of the visible bands in H_2TPP by assuming the HOMO(+1) to be accidentally degenerate. This condition can be weakened by mixing of metal p_z atomic orbitals with the HOMO or electron donating/accepting side chains. However, optical spectroscopy of porphyrins is rather insensitive to electronic structure changes upon peripheral substitution or exchange of the central moiety. Since past experimental electronic structure studies were focused on the Gouterman orbitals, theoretical approaches lack precision on the π manifold[10] and the description of differences between the porphyrin species.

In this work, we investigate the influence of a $2H^+$ (Fig. 1b), Mg^{2+} (Fig. 1c), Zn^{2+} (Fig. 1d), and Cu^{2+} center (Fig. 1e) on the electronic structure of tetraphenylporphyrins (TPPs) and their carboxylated derivatives (TCPPs) in comparison to the parent, unsubstituted porphyrins (Ps). For this purpose, we exploit the

[a] *Institute of Physics and Astronomy, University of Potsdam, Karl-Liebknecht-Str. 24-25, 14476 Potsdam, Germany. E-mail: rbuechner@uni-potsdam.de; Tel: +49 30 806213967*

[b] *Institute for Methods and Instrumentation for Synchrotron Radiation Research, Helmholtz-Zentrum Berlin für Materialien und Energie, Albert-Einstein-Str. 15, 12489 Berlin, Germany. E-mail: vinicius.vaz_da_cruz@helmholtz-berlin.de; Tel: +49 30 806214987*

† Electronic supplementary information (ESI) available: UV/VIS spectra, NEXAFS decomposition, Molecular geometries, and DFT benchmark. See DOI: 10.1039/d1cp03944j

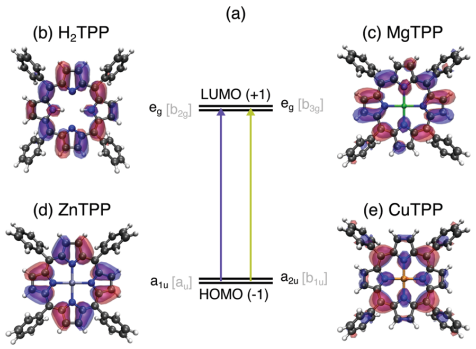

Fig. 1 Frontier orbitals of the series of tetraphenylporphyrin (TPP) cores in relation to optical properties: (a) optical transitions between the near-degenerate LUMO/LUMO+1 (b and c) and HOMO−1/HOMO (d and e) orbitals of all porphyrins give rise to the common UV/VIS absorption bands – the foundation for the Gouterman model. Illustrations of these Gouterman orbitals (named after their symmetry in the D_{4h} [D_{2h}] point group) in the TPPs: (b) e_g [b_{2g}] of H_2TPP, (c) e_g [b_{3g}] of MgTTP, (d) a_{1u} [a_u] of ZnTTP, (e) a_{2u} [b_{1u}] of CuTTP.

element selectivity of Near-Edge X-ray Absorption Spectroscopy (NEXAFS) at the nitrogen atoms, which link the porphyrin macrocycle to the central moiety. To uncover the nature of the porphyrin transition beyond the Gouterman orbitals, density functional theory calculations are carried out for a range of functionals both with the transition potential (TP-DFT) and time dependent approach (TD-DFT). Thereby we establish the porphyrin center as a regulator for the hybridization in the entire molecule controlling both the ionicity of the metal–ligand bond and the π covalency of the macrocycle with peripheral substituents.

2 Methods

2.1 Experimental details

For the experimental investigation 5,10,15,20-tetrakis(4-carboxyphenyl)porphyrins (TCPPs) have been selected, since the carboxyl groups in the *para* position of each phenyl substituent drastically increase the solubility of the *per se* mostly nonpolar porphyrins in aqueous solution. These TPP derivatives were synthesized by Por-Lab (Scharbeutz, Germany) with a minimum purity of 95%. To ensure a maximum concentration of the investigated solutions, the powder samples were dissolved in a 0.01 N NaOH solution. After one hour of ultrasonic treatment, they were filtered through a 25–50 μm filter. The final concentrations were determined by UV/VIS absorption measurements (Shimadzu UV-2700) yielding approximately 3.0 mM for H_2TCPP, 3.6 mM for MgTCPP, 4.6 mM for ZnTCPP, and 2.9 mM for CuTPP.

In order to directly access the absorbance of soft X-rays by transmission measurements, the thickness of the sample needs to be in the order of a few μm. Such a condition is provided by the nmTransmission NEXAFS endstation,[11] where the liquid is pushed into the vacuum chamber through two 30 μm sized nozzles. Upon collision, the two jets form a liquid sheet, whose thickness can be adjusted to suit the penetration depth of soft X-rays. In the present study, a flow rate of 1.6 ml min^{-1} was used resulting in thicknesses of approximately 4 μm. The continuous replenishment of the solutions also prevents radiation induced sample damage.

The experiment was prepared at beamline UE49-SGM[12] (Bessy II, Helmholtz-Zentrum Berlin) with the EDAX endstation[13] and finally conducted at the neighboring beamline UE52-SGM.[14] The spectra were on average acquired for 22 s for each 0.05 eV step. The bandwidth of the incoming X-rays was 0.13 eV.

The resulting spectra were calibrated by the NEXAFS signature of co-dissolved N_2 at 400.84 eV.[15,16] The solvent background including the N_2 features has been measured separately, fitted and subtracted from the sample spectra yielding the pure NEXAFS of aqueous carboxylated TPPs.

2.2 Computational details

Both 5,10,15,20-tetraphenylporphyrins (TPPs, as shown in Fig. 1) and the parent Ps, in which four hydrogen atoms replace the phenyl groups, were investigated by electronic structure calculations to distinguish the effects of substitution and different central atoms.

All geometry optimizations and TD-DFT calculations were carried out with the Orca package.[17] Molecular geometries were optimized with the PBE0[18] functional and def2-TZVP(-f)[19] basis set without symmetry constraints to account for the tilt of the phenyl substituents (see Section 3.3). The RIJCOSX approximation[20] was used with the def2/J[21] auxiliary basis set. Becke–Johnson damping[22,23] was used for dispersion correction. For the TD-DFT X-ray absorption spectrum calculations the def2-TZVP basis was used for all atoms except for the central metal atom and the nitrogen atoms, on which the diffuse def2-TZVPD basis set was adopted. In the calculations, the near-degenerate core-orbitals were localized and the multiplicity of the states involved has been restricted to doublet–doublet (CuTPP) and singlet–singlet excitations (H_2TPP, MgTPP, ZnTPP). For the simulation of the aqueous environment (resulting in the spectra shown in Fig. 4a) the conductor-like polarizable continuum model[24] (CPCM) has been used both in the geometry optimization and TD-DFT calculations.

The choice of the density functional kernel for porphyrins poses a difficult task, specially concerning the X-ray absorption spectrum simulations. Although, the lowest π* resonance is typically well described by global hybrids[25] and consequently all functionals tested here were able to correctly describe the transition from the N 1s orbital to the e_g Gouterman orbitals. For large conjugated systems, such as porphyrins, additional π* resonances occur below the ionization threshold, which might not be properly described by a functional with large exact exchange fraction. On the one hand, the description of higher lying π* orbitals is worse for global hybrids with a high fraction of exact exchange (see DFT benchmark in the ESI†). On the other hand, the description of metal–ligand charge transfer states requires hybrid functionals, including large fractions of Hartree–Fock exchange (HFX).[10,26,27] Since no clear single

compromise could be reached we have used the BLYP[28,29] functional for analyzing the transitions of π character, while the transitions affected by metal–ligand interactions were studied by the BHandHLYP[30] functional.

To assess the role of core–hole relaxation, additional spectral calculations based on the transition potential (TP-DFT) method were carried out. The PSIXAS[31] plugin for PSI4[32] was used and the same basis sets used for the TD-DFT calculations described above to enable comparability. The excited state was calculated in the presence of a half core hole.

The resulting transition energies were shifted according to the first experimental resonance of MgTCPP (−1.96 eV for TP-DFT BLYP, +20.29 eV for TD-DFT BLYP, +1.26 eV for TD-DFT BHandHLYP) or the respective resonance for which interspecies shifts are plotted (−0.21 eV for the second resonance in Fig. 4b). The final spectra were obtained by convolution with a Voigt profile of 0.13 eV[33] (Lorentzian FWHM) and 0.20 eV (Gaussian FWHM) broadening.

Isosurface plots are displayed for the virtual Kohn–Sham orbitals obtained by ground state calculation of CuTPP with an isovalue of 0.02. The orbitals for the remaining systems are visually analogous.

3 Results and discussion

In Fig. 2(a) the N K-edge NEXAFS of carboxylated TPPs with $2H^+$, Mg^{2+}, Zn^{2+}, and Cu^{2+} as central moiety are shown. It can be seen that three resonances appear for each nitrogen atom in a specific chemical environment. The decomposition of the H_2TPP spectrum in transitions of the aminic (N–H, solid lines) and iminic nitrogen atoms (N:, dashed lines) was firstly proposed by Narioka *et al.*[34] and is confirmed by our calculations. The interpretation of the experimental features, which will be discussed below, is summarized in Fig. 2(b). In short, the $1e_g$ (blue), b_{2u} (pink), and $3e_g$ (dark green) resonances are observed for each sample and nitrogen site. To enable comparability to past studies with symmetry restriction or different substituents, (instead of N(1s) → HOMO, N(1s) →...) the transitions are classified by the symmetry of the vacant orbital in the idealized D_{4h} point group of the porphyrin macrocycle and numbered by the respective occurrence above the Fermi level. The nomenclature for the Gouterman orbitals in the reduced idealized symmetry of H_2TPP (D_{2h}) is given in Fig. 1.

It should be noted, that the electronic transitions observed in the X-ray absorption spectrum at typical light element K-edges are dressed by sizable Franck–Condon progressions, which combined with the electronic transition dipole moment determine the intensity ratios.[35–37] The role of vibrational excitations is also evidenced by the large width of the observed near-edge resonances.

The detailed assignment of the experimental features is based on the DFT calculations being shown in Fig. 3. As explained above, the BLYP functional is expected to yield reasonable results for the delocalized π* states of the electron-rich porphyrin macrocycle. The comparison of TD-DFT and TP-DFT calculations allows to assess the role of

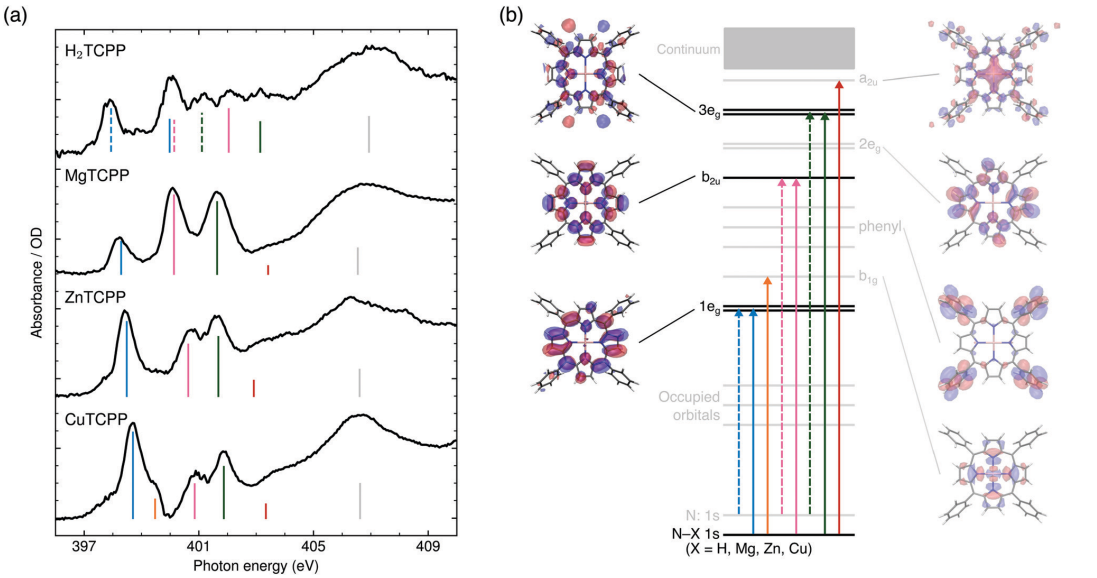

Fig. 2 (a) Experimental N K-edge NEXAFS of carboxylated TPPs. The interpretation of the main resonances (see ESI† for spectral decomposition) is indicated by the color of the dashed (excitation from an iminic nitrogen atom) and solid vertical lines (other nitrogen environments): $1e_g$ (blue), b_{1g} (orange), b_{2u} (pink), $3e_g$ (dark green), a_{2u} (red), shape resonance (gray). (b) Schematic representation of the transitions with equivalent line styles. The orbitals which are involved in the NEXAFS of all investigated species are illustrated in opaque colors.

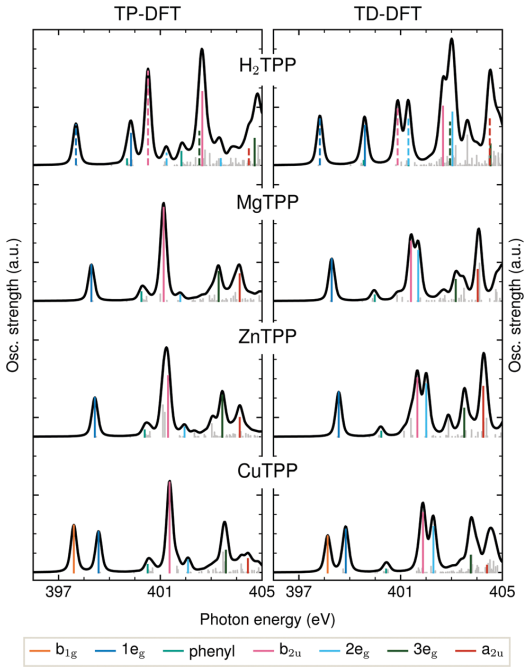

Fig. 3 Transition potential and time dependent DFT calculations of the TPP N K-edge with the BLYP functional. Dashed transition result from the excitation of a core electron of an iminic nitrogen atom.

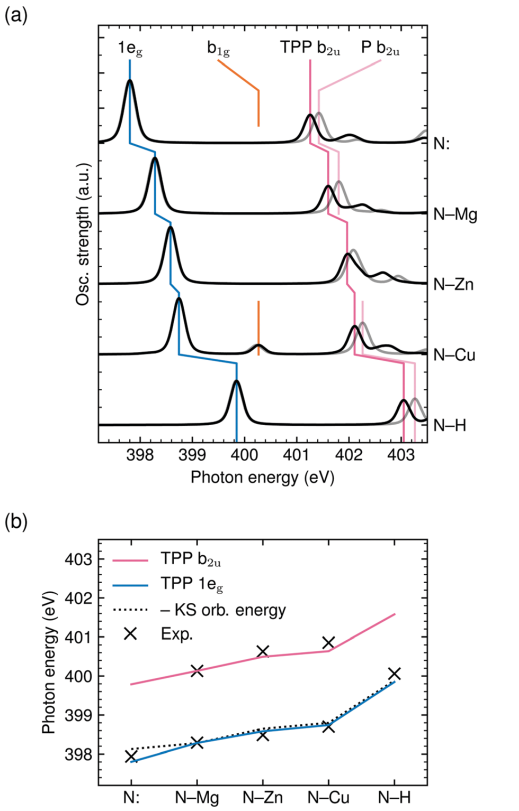

Fig. 4 Blue-shift of the $1e_g$ and b_{2u} transition energies from iminic nitrogen (N:) in H_2TPP, MgTPP, ZnTPP, CuTPP to aminic nitrogen (N–H) in H_2TPP: (a) TD-DFT BHandHLYP spectral simulations with implicit solvation for the TPP series (black) and their phenyl-free P equivalents (gray). (b) Comparison of the calculated, experimental and negative Kohn–Sham orbital energy shifts.

both configuration interactions (CI) and relaxation effects. For investigating the metal–ligand interactions and substituent effects in aqueous solution we refer to Fig. 4(a), where the TD-DFT BHandHLYP spectrum simulations are shown for all investigated TPPs and their phenyl-free P analogs.

3.1 Spectral interpretation

The first peak in all experimental spectra (397.9–400.1 eV, blue in Fig. 2a) is the $1e_g(\pi^*)$ resonance. The vacant orbitals of the underlying transition are the Gouterman LUMO and LUMO+1, which also participate in the UV/VIS transitions (see Fig. 1). There is general consensus in literature about the assignment of this feature,[34,38–43] which is not the case for the subsequent resonances.

The narrow $1e_g$ shoulder (399.5 eV, orange), that is only observed for a Cu^{2+} center, results from the half occupied Cu $3d_{x^2-y^2}$ orbital which mixes with the porphyrin σ-type b_{1g} orbital in D_{4h} symmetry. Early solid state measurements of copper porphyrins[39,40,44] have not been able to resolve this feature. Mangione *et al.*[43] assigned the b_{1g} resonance to an $1e_g$ shoulder to lower energies – similar to the one which we observe for all samples around 398 eV. Since radiation damage can be excluded for the setup used (see section 2.1) and this shoulder is also visible for the closed-shell ZnTCPP we attribute this feature to thermal geometric distortions. For CuTCPP we interpret the 399.5 eV shoulder on the opposite side of the $1e_g$ peak as σ* resonance. This relative position is in agreement with linear dichroism measurements at the N K-edge of copper phthalocyanine,[45] explains the existence of a similar shoulder in iron porphyrin in solution,[46] and is theoretically backed up by our spectrum calculations and the ones by Schmidt *et al.*[47] for another transition metal TPP.[47] For CuTPP, the transition appears in both DFT BLYP calculations (see Fig. 3) below the $1e_g$ resonance similar to the calculations done by Mangione *et al.*[43] The energetic position above the $1e_g$ resonance, being proposed in this work, is based on the benchmarked functionals with a large fraction of HFX as BHandHLYP (see Fig. 4a). This behavior is expected, as hybrid functionals describe charge transfer states more precisely than pure functionals.[10]

The second intense peak in the experimental spectra (400.1–402.0 eV, pink) has been interpreted as b_{1g}[47] or substituent feature[46,48] in the past. The strong intensity of this peak in all carboxylated metal TPP spectra and the $1e_g$ shoulder, which is only observed for CuTCPP, speak against the former assignment. A substituent transition – in our case

phenyl(π*) – is indeed observed in this energy range for TD-DFT based calculations with low or no HFX (cyan in Fig. 3). However, the comparison with experimental octaethylporphyrin[40] and especially metal P NEXAFS spectra[41,44,49] (without any outer substituent) make clear that this peak belongs to the π* signature of the porphyrin macrocycle. The second porphyrin peak (P b_{2u} in Fig. 4a) results from the b_{2u}(π*) transition. This feature is prominent in all calculations shown. When the TP-DFT and TD-DFT calculations are compared, it can be noted that the b_{2u} resonance is lowered in energy yielding a better agreement with the experimental positions for TP-DFT. At the same time, the $2e_g$ transition is quenched following the general pattern of the core–hole effect to concentrate the excitation intensity on the energetically lower transitions.[50]

The quenching of the $2e_g$ peak by core–hole relaxation is in agreement with results found in literature.[34,44] Nevertheless, the partial density of unoccupied states has been used to explain the next experimental feature around 401.7 eV (dark green).[38,39,44] As the $3e_g$ feature has a strong intensity for all calculations with low HFX (see Fig. 3 and ESI†), we assign the third prominent feature to the $3e_g$(π*) transition.

In agreement with previous calculations,[34] the experimental shoulder around the ionization potential of the metal (M) porphyrins (402.9–403.4 eV, red) can be interpreted as a_{2u} transition. This molecular orbital is formed by hybridization of the porphyrin a_{2u}(π*) with M p_z orbitals.

Above 405 eV, shape resonances can be identified in all experimental spectra (gray). Noticeable is the small blue-shift from MgTCPP to ZnTCPP to CuTCPP indicating a steady contraction of the M–N bond.[51] This interpretation agrees with the calculated [and experimentally determined[52]] TPP bond length of 2.06 Å for Mg–N, 2.04 Å [2.04 Å] for Zn–N, 2.01 Å [1.98 Å] for Cu–N.

3.2 Covalency of the central metal complex

As shown in Fig. 4(b), the experimental $1e_g$ resonance energy increases from N: in H_2TCPP (397.9 eV) to MgTCPP (398.3 eV) to ZnTCPP (398.5 eV) to CuTCPP (398.7 eV) to N–H in H_2TCPP (400.1 eV), which is well reproduced by TD-DFT BHandHLYP calculations for the TPP core with implicit solvation. This observation might be surprising, as the $1e_g$ Gouterman orbital is known to be little influenced by the choice of the central moiety.[10,53] Also differences in the electron–hole interaction between the TPPs and derivatives are expected to be marginal, as the large conjugate system leads to an equally low contribution of the highly delocalized π* orbital at the excited nitrogen atom for all investigated species.[50]

As pointed out by García-Lastra *et al.*,[40] the energy of the $1e_g$ near-edge resonances mainly depends on the electron density at the nitrogen atoms. This is in line with our calculations as far as the negative Kohn–Sham orbital energies (with 50% HFX) are comparable with ionization potentials. Since a higher electron density at the nitrogen site leads to better screening of the core–hole and thereby lowers the $1e_g$ excitation energy, the negative charge at the nitrogen atoms must decrease in the order: N: in H_2TPP, MgTPP, ZnTPP, CuTPP, N–H in H_2TPP (and equally for the TCPPs). Accordingly, the covalency of the N–X (X = Mg, Zn, Cu, H) bond increases. This finding is also in line with the more contracted N–X bond in CuTPP compared to ZnTPP and ZnTPP compared to MgTPP (as discussed above).

The Löwdin orbital populations of the BHandHLYP calculations with implicit solvation reveal an evolution of the complex covalent bond along the series: The N–Mg interaction is mainly characterized by the overlap of magnesium and nitrogen s and p_x/p_y orbitals (in the porphyrin plane). For the other metal porphyrins, an increased hybridization with metal $d_{x^2-y^2}$ and d_{z^2} atomic orbitals is noticeable. From zinc to copper, π bonding to metal d_{xz}/d_{yz} orbitals gains in importance. That is in line with the established strong mixing of unoccupied metal d and porphyrin π orbitals for open shell transition metals.[53] In the NEXAFS spectra, the high covalency of the copper complex becomes apparent by the b_{1g} ligand-to-metal charge transfer state, which is missing for the other porphyrins.

Hence, the systematic shift of the $1e_g$ X-ray absorption resonance is a measure of the charge transfer from the porphyrin macrocycle to the metal center. MgTCPP is the most ionic species with an electron density at the nitrogen sites close to the iminic nitrogen atoms in H_2TCPP. By orbital re-hybridization the ionicity is reduced for ZnTCPP. The strongest metal–porphyrin interactions are observed in CuTCPP where charge delocalization over both the porphyrin macrocycle and the central complex causes a decrease of the nitrogen charge density, which is lower only for N–H in H_2TCPP.

3.3 Covalency to peripheral substituents

As seen in Fig. 4, the central metal atom within the porphyrin ring not only affects the $1e_g$ resonance position but also the energy of the b_{2u} feature. Especially from the comparison of MgTCPP and ZnTCPP (see Fig. 4b) it becomes clear that the interspecies shift of the b_{2u} resonance exceeds the chemical shift of the N 1s core level discussed above.

A shift of the b_{2u} resonance has been experimentally established upon substitution of NiP forming NiTPP.[41] The observed shift is well reproduced by our TD-DFT calculations with BHandHLYP (see ESI†). Analogously, the calculated spectra of P and TPP are compared for the iminic, magnesium, zinc, copper, and aminic center in Fig. 4(a). It can be seen that the enhanced experimental red-shift of MgTPP is reflected in a larger calculated MgP → MgTPP shift compared to CuP → CuTPP‡.

The experimental evidence for the red-shift upon P substitution with phenyl groups is mirrored in the calculations by CI mixing of the b_{2u} transition with those to covalent porphyrin–phenyl orbitals (see phenyl orbital plot in Fig. 2b). In other words, the rehybridization and mixing of porphyrin and phenyl orbitals and their contribution in the CI expansion continuously decreases from MgTPP to ZnTPP to CuTPP.

‡ The b_{2u} feature of ZnP cannot be unambiguously assigned in the TD-DFT BHandHLYP calculation, but seems to be lowered in energy due to strong CI with transitions to mixed zinc atomic and porphyrin π* orbitals.

The influence of peripheral substituents on the porphyrin electronic structure has rarely been discussed[42,43,53] or explicitly excluded[40] in literature. For TPPs this simplification has been justified by the assumption that the phenyl groups are oriented perpendicular (90°) to the porphyrin macrocycle.[34] However, in practice there is a competition between steric repulsion and π overlap.[54] Together with geometric distortions induced by the environment this competition leads to phenyl tilts down to 20° on surfaces.[44] In our calculations, the phenyl tilt amounts to approximately 66°, which is in agreement with X-ray crystallographic data.[55] In accordance with the assumed increase of phenyl-macrocycle π overlap the calculated phenyl tilt slightly decreases from CuTPP to ZnTPP to MgTPP (see ESI†).

The rise in intensity from CuTCPP to ZnTCPP to MgTCPP around 400 eV (see Fig. 2) can be interpreted as an indicator for increasing covalency leading to the formation of a N(1s) → phenyl(π*) feature in this energy region. This effect would be governed by mixing of the N $2p_z$ orbital with the phenyl π* one. However, due to strong vibrational broadening of the intense π* resonances the identification of the phenyl/substituent peak is problematic, nevertheless, its indirect presence can be seen in the shift of the b_{2u} resonance.

Experimental evidence for a change in absorbance around 400 eV in connection to a variation of the substituents is provided by Mangione *et al.*[43] In their calculations the authors find an increased mixing between porphyrin and substituent orbitals upon fluorine decoration of the phenyl groups in CuTPP opposed to H_2TPP.

In our series the macrocycle-substituent covalency is increased for a more ionic porphyrin center. That way, the lack of charge transfer with the metal for ZnTPP/ZnTCPP and especially MgTPP/MgTCPP is compensated by an increased charge delocalization onto the substituents. This observation matches with the behaviour of haem, that reduction of the system leads to a global increase of the porphyrin charge density including non-conjugate substituents.[56]

4 Conclusions

By the experimental determination and theoretical description of the N K-edge NEXAFS of a series of porphyrins, we have been able to clarify the interpretation of higher π* resonances beyond those of the well-known Gouterman orbitals. We find that even though the electron–hole interaction is of minor importance for relative excitation energies (due to the highly delocalized π system), relaxation effects are crucial for the estimation of excitation intensities. The TP-DFT method is therefore well suited for the description of porphyrin core-excited states. Charge transfer states, however, are only correctly described by hybrid functionals with high HFX, which currently yield theoretically sound results only for TD-DFT.

The experimental and theoretical analysis of systematic interspecies shifts uncovered two trends: The ionicity of the porphyrin center increases from N–H to N–Cu to N–Zn to N–Mg to N:. At the same time the covalency with peripheral substituents increases to compensate for the high charge density at the nitrogen sites.

These findings directly relate to the different functions of metal porphyrins and derivatives. While the ionic character of Mg^{2+}macrocycle^{2-} is essential for the charge transfer from negatively charged chlorophyll radicals during photosynthesis, it also gives rise to the low stability of the isolated molecule.[5] The substitution of magnesium by copper increases the stability of the complex enabling the human utilization beyond its photochemical properties. In the context of technical light-harvesting the observed metal controlled π hybridization of porphyrin and phenyl orbitals are of great interest. Cordones *et al.*[48] raised the importance of electron localization in the excited state for the efficiency of dye-sensitized solar cells. Zinc porphyrins, which can – based on our results – be seen as a tradeoff between stability and low mixing of metal and porphyrin states, serve as excellent electron acceptors.[48]

Taken together, the investigation of TPP/TCPP orbitals beyond the Gouterman picture revealed the porphyrin center as a regulator for covalency in the entire molecule. In MgTPP/MgTCPP the central N–Mg bond is most ionic so that π hybridization with peripheral substituents is enhanced in compensation. CuTPP/CuTCPP is a counter example with a rather covalent metal–ligand interaction and low π hybridization to the phenyl substituents. Thereby we uncovered the connection between porphyrin constitution and resulting chemical properties which enables the versatile use of porphyrins and derivatives in general.

Author contributions

R. B.: data curation, investigation, project administration, visualization, writing – original draft; M. F.: resources, investigation; R. H.: investigation; A. P.: supervision; V. V. C.: formal analysis, investigation, supervision; A. F.: conceptualization, funding acquisition, supervision; all: writing – review & editing.

Conflicts of interest

There are no conflicts to declare.

Acknowledgements

The authors acknowledge Mathias Senge for sharing his expertise on the chemistry of porphyrins. A. F. and R. B. acknowledge funding from the ERC-ADG-2014 – Advanced Investigator Grant No. 669531 EDAX under the Horizon 2020 EU Framework Program for Research and Innovation. The authors thank the Helmholtz-Zentrum Berlin for the allocation of synchrotron radiation beamtime.

References

1 A. A. Lamola and T. Yamane, *Science*, 1974, **186**, 936–938.

2 D. Todd, *Br. J. Dermatol.*, 1994, **131**, 751–766.
3 G. Calogero, G. Di Marco, S. Caramori, S. Cazzanti, R. Argazzi and C. A. Bignozzi, *Energy Environ. Sci.*, 2009, **2**, 1162–1172.
4 M. Urbani, M. Grätzel, M. K. Nazeeruddin and T. Torres, *Chem. Rev.*, 2014, **114**, 12330–12396.
5 W. Kaim, B. Schwederski and A. Klein, *Bioinorganic Chemistry – Inorganic Elements in the Chemistry of Life: An Introduction and Guide*, Wiley, Chichester, 2013.
6 A. A. Ryan and M. O. Senge, *Photochem. Photobiol. Sci.*, 2015, **14**, 638–660.
7 B. Gajewska, S. Raccio, K. J. Rodriguez and N. Bruns, *Polym. Chem.*, 2019, **10**, 125–135.
8 R. Dashwood, *Int. J. Oncol.*, 1997, **10**, 721–727.
9 M. Gouterman, *J. Mol. Spectrosc.*, 1961, **6**, 138–163.
10 J. R. de Souza, M. M. F. de Moraes, Y. A. Aoto and P. Homem-de Mello, *Phys. Chem. Chem. Phys.*, 2020, **22**, 23886–23898.
11 M. Fondell, S. Eckert, R. M. Jay, C. Weniger, W. Quevedo, J. Niskanen, B. Kennedy, F. Sorgenfrei, D. Schick, E. Giangrisostomi, R. Ovsyannikov, K. Adamczyk, N. Huse, P. Wernet, R. Mitzner and A. Föhlisch, *Struct. Dyn.*, 2017, **4**, 054902.
12 A. Pietzsch and S. Eisebitt, *J. Large-Scale Res. Facil.*, 2016, **2**, A54.
13 K. Kunnus, I. Rajkovic, S. Schreck, W. Quevedo, S. Eckert, M. Beye, E. Suljoti, C. Weniger, C. Kalus, S. Grübel, M. Scholz, D. Nordlund, W. Zhang, R. W. Hartsock, K. J. Gaffney, W. F. Schlotter, J. J. Turner, B. Kennedy, F. Hennies, S. Techert, P. Wernet and A. Föhlisch, *Rev. Sci. Instrum.*, 2012, **83**, 123109.
14 P. S. Miedema, W. Quevedo and M. Fondell, *J. Large-Scale Res. Facil.*, 2016, **2**, A27.
15 R. Flesch, A. A. Pavlychev, J. J. Neville, J. Blumberg, M. Kuhlmann, W. Tappe, F. Senf, O. Schwarzkopf, A. P. Hitchcock and E. Rühl, *Phys. Rev. Lett.*, 2001, **86**, 3767–3770.
16 A. W. Gillespie, F. L. Walley, R. E. Farrell, T. Z. Regier and R. I. R. Blyth, *J. Synchrotron Radiat.*, 2008, **15**, 532–534.
17 F. Neese, *Wiley Interdiscip. Rev.: Comput. Mol. Sci.*, 2012, **2**, 73–78.
18 C. Adamo and V. Barone, *J. Chem. Phys.*, 1999, **110**, 6158–6170.
19 F. Weigend and R. Ahlrichs, *Phys. Chem. Chem. Phys.*, 2005, **7**, 3297–3305.
20 F. Neese, F. Wennmohs, A. Hansen and U. Becker, *Chem. Phys.*, 2009, **356**, 98–109.
21 F. Weigend, *Phys. Chem. Chem. Phys.*, 2006, **8**, 1057–1065.
22 S. Grimme, J. Antony, S. Ehrlich and H. Krieg, *J. Chem. Phys.*, 2010, **132**, 154104.
23 S. Grimme, S. Ehrlich and L. Goerigk, *J. Comput. Chem.*, 2011, **32**, 1456–1465.
24 V. Barone and M. Cossi, *J. Phys. Chem. A*, 1998, **102**, 1995–2001.
25 T. Fransson, I. E. Brumboiu, M. L. Vidal, P. Norman, S. Coriani and A. Dreuw, *J. Chem. Theory Comput.*, 2021, **17**, 1618–1637.
26 Z.-L. Cai, M. J. Crossley, J. R. Reimers, R. Kobayashi and R. D. Amos, *J. Phys. Chem. B*, 2006, **110**, 15624–15632.
27 I. E. Brumboiu, G. Prokopiou, L. Kronik and B. Brena, *J. Chem. Phys.*, 2017, **147**, 044301.
28 A. D. Becke, *Phys. Rev. A: At., Mol., Opt. Phys.*, 1988, **38**, 3098–3100.
29 C. Lee, W. Yang and R. G. Parr, *Phys. Rev. B: Condens. Matter Mater. Phys.*, 1988, **37**, 785–789.
30 A. D. Becke, *J. Chem. Phys.*, 1993, **98**, 1372–1377.
31 C. Ehlert and T. Klamroth, *J. Comput. Chem.*, 2020, **41**, 1781–1789.
32 J. M. Turney, A. C. Simmonett, R. M. Parrish, E. G. Hohenstein, F. A. Evangelista, J. T. Fermann, B. J. Mintz, L. A. Burns, J. J. Wilke, M. L. Abrams, N. J. Russ, M. L. Leininger, C. L. Janssen, E. T. Seidl, W. D. Allen, H. F. Schaefer, R. A. King, E. F. Valeev, C. D. Sherrill and T. D. Crawford, *Wiley Interdiscip. Rev.: Comput. Mol. Sci.*, 2012, **2**, 556–565.
33 C. Nicolas and C. Miron, *J. Electron Spectrosc. Relat. Phenom.*, 2012, **185**, 267–272.
34 S. Narioka, H. Ishii, Y. Ouchi, T. Yokoyama, T. Ohta and K. Seki, *J. Phys. Chem.*, 1995, **99**, 1332–1337.
35 F. K. Gel'Mukhanov, L. Mazalov and A. Kondratenko, *Chem. Phys. Lett.*, 1977, **46**, 133–137.
36 J. Stöhr, *NEXAFS Spectroscopy*, Springer, San Jose, 1992.
37 V. Vaz da Cruz, N. Ignatova, R. C. Couto, D. A. Fedotov, D. R. Rehn, V. Savchenko, P. Norman, H. Ågren, S. Polyutov, J. Niskanen, S. Eckert, R. M. Jay, M. Fondell, T. Schmitt, A. Pietzsch, A. Föhlisch, F. Gel'mukhanov, M. Odelius and V. Kimberg, *J. Chem. Phys.*, 2019, **150**, 234301.
38 T. Okajima, Y. Yamamoto, Y. Ouchi and K. Seki, *J. Electron Spectrosc. Relat. Phenom.*, 2001, **114-116**, 849–854.
39 I. Reid, Y. Zhang, A. Demasi, A. Blueser, L. Piper, J. E. Downes, A. Matsuura, G. Hughes and K. E. Smith, *Appl. Surf. Sci.*, 2009, **256**, 720–725.
40 J. M. García-Lastra, P. L. Cook, F. J. Himpsel and A. Rubio, *J. Chem. Phys.*, 2010, **133**, 151103.
41 G. I. Svirskiy, A. V. Generalov, A. Y. Klyushin, K. A. Simonov, S. A. Krasnikov, N. A. Vinogradov, A. L. Trigub, Y. V. Zubavichus, A. B. Preobrazhenski and A. S. Vinogradov, *Phys. Solid State*, 2018, **60**, 581–591.
42 M. V. Nardi, R. Verucchi, L. Pasquali, A. Giglia, G. Fronzoni, M. Sambi, G. Mangione and M. Casarin, *Phys. Chem. Chem. Phys.*, 2015, **17**, 2001–2011.
43 G. Mangione, M. Sambi, S. Carlotto, A. Vittadini, G. Ligorio, M. Timpel, L. Pasquali, A. Giglia, M. V. Nardi and M. Casarin, *Phys. Chem. Chem. Phys.*, 2016, **18**, 24890–24904.
44 K. Diller, F. Klappenberger, M. Marschall, K. Hermann, A. Nefedov, C. Wöll and J. V. Barth, *J. Chem. Phys.*, 2012, **136**, 014705.
45 L. Floreano, A. Cossaro, R. Gotter, A. Verdini, G. Bavdek, F. Evangelista, A. Ruocco, A. Morgante and D. Cvetko, *J. Phys. Chem. C*, 2008, **112**, 10794–10802.
46 R. Golnak, J. Xiao, K. Atak, J. S. Stevens, A. Gainar, S. L. M. Schroeder and E. F. Aziz, *Phys. Chem. Chem. Phys.*, 2015, **17**, 29000–29006.

47 N. Schmidt, R. Fink and W. Hieringer, *J. Chem. Phys.*, 2010, **133**, 054703.
48 A. A. Cordones, C. D. Pemmaraju, J. H. Lee, I. Zegkinoglou, M.-E. Ragoussi, F. J. Himpsel, G. de la Torre and R. W. Schoenlein, *J. Phys. Chem. Lett.*, 2021, **12**, 1182–1188.
49 K. Diller, F. Klappenberger, F. Allegretti, A. C. Papageorgiou, S. Fischer, A. Wiengarten, S. Joshi, K. Seufert, D. Écija, W. Auwärter and J. V. Barth, *J. Chem. Phys.*, 2013, **138**, 154710.
50 H. Oji, R. Mitsumoto, E. Ito, H. Ishii, Y. Ouchi, K. Seki, T. Yokoyama, T. Ohta and N. Kosugi, *J. Chem. Phys.*, 1998, **109**, 10409–10418.
51 F. W. Lytle, R. B. Greegor and A. J. Panson, *Phys. Rev. B: Condens. Matter Mater. Phys.*, 1988, **37**, 1550–1562.
52 E. B. Fleischer, C. K. Miller and L. E. Webb, *J. Am. Chem. Soc.*, 1964, **86**, 2342–2347.
53 M.-S. Liao and S. Scheiner, *J. Chem. Phys.*, 2002, **117**, 205–219.
54 T. A. Jung, R. R. Schlittler and J. K. Gimzewski, *Nature*, 1997, **386**, 696–698.
55 S. J. Silvers and A. Tulinsky, *J. Am. Chem. Soc.*, 1967, **89**, 3331–3337.
56 M. P. Johansson, M. R. Blomberg, D. Sundholm and M. Wikström, *Biochim. Biophys. Acta, Gen. Subj.*, 2002, **1553**, 183–187.

Fundamental electronic changes upon intersystem crossing in large aromatic photosensitizers: free base 5,10,15,20-tetrakis(4-carboxylatophenyl)porphyrin

R. Büchner, V. Vaz da Cruz, N. Grover, A. Charisiadis, M. Fondell, R. Haverkamp, M. O. Senge, and A. Föhlisch

Accepted by Phys. Chem. Chem. Phys. (19.01.2022)[§]

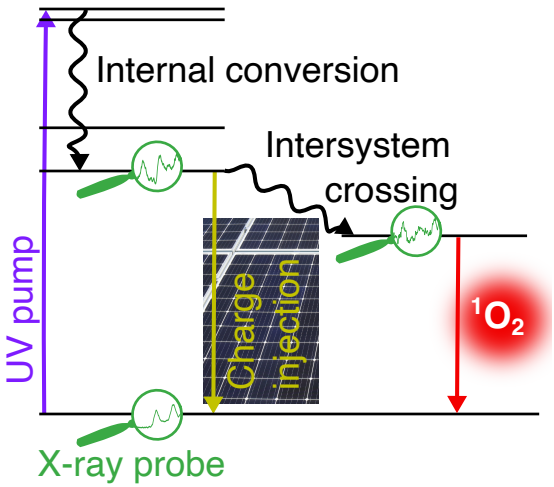

The crucial transient states of free-base porphyrins are characterized by time-resolved X-ray absorption spectroscopy unraveling their unusual relaxation pathway.

[§]Reproduced from ***Phys. Chem. Chem. Phys.***, 2022,**24**, 7505-7511 with permission from the PCCP Owner Societies. (CC BY 3.0)

PCCP

ROYAL SOCIETY OF CHEMISTRY

PAPER

Fundamental electronic changes upon intersystem crossing in large aromatic photosensitizers: free base 5,10,15,20-tetrakis(4-carboxylatophenyl)porphyrin†

Cite this: DOI: 10.1039/d1cp05420a

Robby Büchner, *[ab] Vinícius Vaz da Cruz, *[b] Nitika Grover, [c] Asterios Charisiadis, [c] Mattis Fondell, [b] Robert Haverkamp, [ab] Mathias O. Senge *[d] and Alexander Föhlisch [ab]

Received 26th November 2021,
Accepted 19th January 2022

DOI: 10.1039/d1cp05420a

rsc.li/pccp

Free base 5,10,15,20-tetrakis(4-carboxylatophenyl)porphyrin stands for the class of powerful porphyrin photosensitizers for singlet oxygen generation and light-harvesting. The atomic level selectivity of dynamic UV pump – N K-edge probe X-ray absorption spectroscopy in combination with time-dependent density functional theory (TD-DFT) gives direct access to the crucial excited molecular states within the unusual relaxation pathway. The efficient intersystem crossing, that is El-Sayed forbidden and not facilitated by a heavy atom is confirmed to be the result of the long singlet excited state lifetime (Q_x 4.9 ns) and thermal effects. Overall, the interplay of stabilization by conservation of angular momenta and vibronic relaxation drive the de-excitation in these chromophores.

1 Introduction

Apart from the potential in future photovoltaics,[1] free base porphyrins are efficient photosensitizers for the generation of singlet oxygen – a highly reactive oxidizing agent.[2] As a consequence, the accumulation of free base porphyrins in plants and vertebrates such as humans leads to pathological photosensitivity.[3–5] On the other hand, the high singlet oxygen yield of free base porphyrins in a wide spectral range is employed in the treatment of tumors,[6,7] atherosclerosis,[8] skin diseases,[9] and microbia[10] by photodynamic therapy (PDT), for sustainable chemistry,[11,12] and photocatalysis.[13,14]

In all these cases, free base porphyrins are excited by ultraviolet or visible light (UV/VIS) to one of the singlet excited states (Fig. 1a). Higher excited states (Q_y, B) are transformed to the lowest singlet excited state (Q_x) by ultrafast internal conversion.[15] The nanosecond lifetime of Q_x in combination with vibronic coupling were predicted to facilitate the efficient intersystem crossing to the lowest triplet state (T_1).[9,16] In the presence of oxygen, triplet free base porphyrin decays to the singlet ground state (S_0) by triplet energy transfer raising ground state oxygen ($^3\Sigma_g^-$ O_2) to its first singlet excited state ($^1\Delta_g$ O_2).[17] While there is a general agreement in the literature about this abstract deactivation path, the exact electronic structure of the involved states is debated especially regarding the energetic order of the frontier orbitals in T_1.[18]

Free base 5,10,15,20-tetrakis(4-carboxylatophenyl)porphyrin ($TCPP^{4-}$, Fig. 1b) is the parent compound of novel agents for photodynamic diagnosis and PDT of breast and skin cancer with singlet oxygen quantum yields up to $\Phi_\Delta = 0.61$.[19] Compared to previous studies on lipophilic porphyrins, such as free base 5,10,15,20-tetraphenylporphyrin (TPP), this water-soluble porphyrin allows the investigation in aqueous solution mimicking the water-containing environment in a biological cell.[20] Considering the light-harvesting applications, carboxylate moieties of $TCPP^{4-}$ are typical anchoring groups in dye-sensitized solar cells.[14] Therefore this molecule is an ideal candidate for transient electronic structure investigation of solar cell chromophores subsequent to the existing work on zinc porphyrins.[21]

In this work, we monitor the relaxation of photoexcited $TCPP^{4-}$ on an atomic level with focus on the configurations and lifetimes of the long-lived lowest singlet and triplet excited

[a] Institute of Physics and Astronomy, University of Potsdam, Karl-Liebknecht-Str. 24-25, 14476 Potsdam, Germany. E-mail: rbuechner@uni-potsdam.de
[b] Institute for Methods and Instrumentation for Synchrotron Radiation Research, Helmholtz-Zentrum Berlin für Materialien und Energie, Albert-Einstein-Str. 15, 12489, Berlin, Germany. E-mail: vinicius.vaz_da_cruz@helmholtz-berlin.de
[c] School of Chemistry, Chair of Organic Chemistry, Trinity College Dublin, The University of Dublin, Trinity Biomedical Sciences Institute, 152-160 Pearse Street, Dublin 2, Ireland
[d] Institute for Advanced Study, Technical University of Munich, Lichtenbergstrasse 2a, 85748 Munchen Garching, Germany. E-mail: mathias.senge@tum.de

† Electronic supplementary information (ESI) available: Details on synthesis, full ground state and transient spectra, reconstruction of excited state spectra, optimized geometries and application of the restricted subspace approximation. See DOI: 10.1039/d1cp05420a

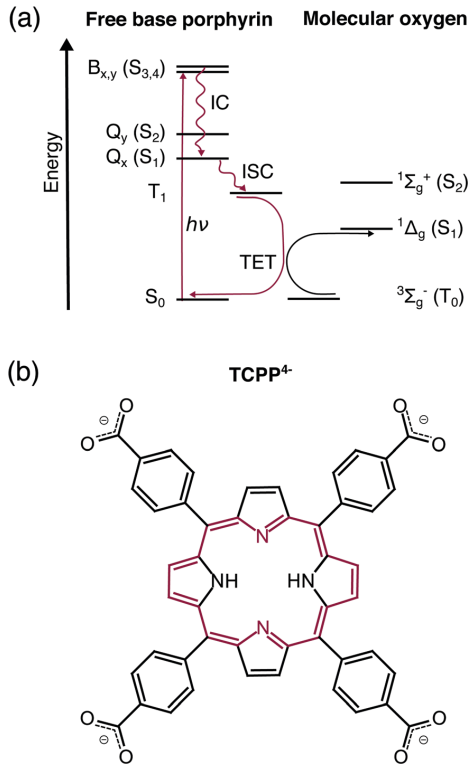

Fig. 1 (a) Dominant relaxation pathway of optically exited free base porphyrins in the presence of molecular oxygen: IC – internal conversion, ISC – intersystem crossing, TET – triplet energy transfer. (b) Structural formula of free base 5,10,15,20-tetrakis(4-carboxylatophenyl)porphyrin ($TCPP^{4-}$). The 18 π-electron aromatic system is highlighted in red.

states. Therefore UV pump – N K-edge probe spectroscopy is employed yielding the evolution of the near-edge X-ray absorption fine structure (NEXAFS) after the photoexcitation. The spectra are interpreted with the aid of TD-DFT calculations within the restricted subspace approximation (RSA)[22] providing detailed information on the electronic structure before and after the intersystem crossing, as well as evidence for the theoretically proposed vibronic deactivation channels.

2 Methods

The precursor 5,10,15,20-tetrakis(4-methoxycarbonylphenyl) porphyrin (TCOOMePP) and desired TCPP compounds were synthesized following previously reported procedures[23,24] (see Synthesis for details, ESI†). The final 3 mM $TCPP^{4-}$ solution (pH ≈ 12) was prepared with deionized water and NaOH. The solute is expected to be fourfold deprotonated since all carboxyl groups independently deprotonate with $pK_a \approx 6$.[25]

Preparatory measurements were carried out at beamline UE49-SGM[26] with the EDAX endstation[27] (Bessy II, Berlin). The static and transient data has been acquired with the nmTransmission NEXAFS[28] endstation at UE52-SGM.[29] In this setup a thin leaf, that is formed upon the collision of two liquid jets, is used to directly determine the X-ray transmission of the sample solution. The liquid jets enter the vacuum chamber *via* a pair of 30 μm sized nozzles with a combined flow rate of 1.4 mL min^{-1}.

The sample was excited at 343 nm with a pulse energy of 7 μJ and a spot size of (80 × 80) μm^2. A repetition rate of 208 kHz was chosen, to allow full sample replenishment between the UV pulses. The X-ray probe had a bandwidth of 0.13 eV and spot size of (55 × 140) μm^2. The temporal resolution of the experiment is limited by the length and jitter of the synchrotron bunches and amounts to 0.14 ± 0.01 ns according to the fit of the delay traces. The static, 0.1 ns, 5.0 ns, and 40.0 ns delayed transient spectra were in total acquired for 30 s, 13 s, 6 s, and 3 s per 0.05 eV step, respectively. Keeping the X-ray photon energy fixed and varying the pump–probe delay from −0.5 ns to 1.0 ns and 1.0 ns to 40.0 ns yielded the time traces, each with 61 steps and a net acquisition time of 11 minutes.

All photon energies were calibrated by the signature of co-dissolved N_2 in the ground state spectrum.[30,31] The shown static spectrum was yielded by subtracting the fitted N_2 signature and solvent background.

For the theoretical description, the parent carboxylate-free TPP was considered. The influence of the weakly electron donating carboxylate groups for the probe of the local electronic structure at the nitrogen sites is expected to be small. This assumption is based on the high similarity in the experimental N K-edge spectra of TCPP and TPP.[32,33] The ORCA package[34] was used for all electronic structure calculations. The aqueous environment of the experimentally investigated molecules was modeled by the conductor-like polarizable continuum model (CPCM).[35] The B3LYP[36,37] functional was used with the def2-TZVP(-f)[38] basis set, def2/J[39] auxiliary basis set, and Becke–Johnson damping.[40,41] The choice of these parameters is based on our past benchmark[32] and the computational efficiency needed for the simulation of multiple core- and valence-excited states. The geometry optimization was carried out for the S_0, T_1, and Q_x state without symmetry restrictions to yield more accurate geometries regarding the tilt of the phenyl groups[32] and deformations of the porphyrin macrocycle in the excited states. The given configuration interaction coefficients are the result of ground state TD-DFT calculations.

To compute the transient signals, we employed the restricted subspace approximation[22] in the TD-DFT spectrum calculations using Multiwfn[42] to compute the transition dipole moments between the involved states (see Application of the restricted subspace approximation for details, ESI†). The lowest excitations from the localized –N═ and –NH– 1s orbitals have been determined for the minimum geometry of the respective electronic state. The resulting spectra were shifted by 12.5 eV and broadened by 0.13 eV (Gaussian FWHM) and 0.5 eV (Lorentzian FWHM[43]) according to the lowest experimental ground state transition.

3 Results and discussion

The first model of the porphyrin electronic structure, that successfully explains the UV/VIS spectra (Fig. 2a), was proposed by Gouterman in 1959[44,45] and is used to the present day. According to this model and our calculations, all bands in the optical spectrum of $TCPP^{4-}$ (Fig. 2a) are related to transitions between the two highest occupied (HOMOs) and lowest unoccupied (LUMOs) molecular orbitals and hence of $\pi \rightarrow \pi^*$ character. We use the irreducible representations to describe these orbitals throughout this work to account for the D_{2h} symmetry of the free base porphyrin macrocycle (oriented as shown in Fig. 2b). From group theory, it can be deduced that the optical transitions are either x ($b_{1u} \rightarrow b_{2g}$, $a_u \rightarrow b_{3g}$) or y ($b_{1u} \rightarrow b_{3g}$, $a_u \rightarrow b_{2g}$) polarized, as shown in Fig. 2b. Transitions of the same polarization (x or y) are expected to mix according to their proximity in energy.

While the two lowest unoccupied orbitals are degenerate in metalloporphyrins (where the central protons are replaced by a divalent metal ion) the b_{2g} orbital is lowered in energy for ground state free base porphyrins due to the electron density on the aminic nitrogen atoms.[46] The order of the HOMOs depends on the peripheral substituents. If they are linked to the bridging (*meso*) carbon atoms, the b_{1u} orbital is slightly higher in energy than the a_u orbital[47] (see Fig. 2b).

Even though, the frontier orbitals are not completely pairwise degenerate, the aromatic porphyrin macrocycle can be approximated by a free electron ring[48] to explain the absorption spectrum (Fig. 2a). From the nodes of the wavefunctions (depicted in Fig. 2b) the orbital angular momentum normal to the porphyrin plane can be derived: $l_z^{\mathrm{HOMOs}} \approx \pm 4\hbar$ and $l_z^{\mathrm{LUMOs}} \approx \pm 5\hbar$. According to the ground state of total angular momentum $L_z^{S_0} = 0$ and the selection rule $\Delta L_z = \pm 1\hbar$, transitions to the B_x/B_y state ($L_z^{B} \approx \pm 1\hbar$) are high in energy and allowed, while the opposite applies to transitions to the Q_x/Q_y states ($L_z^{Q} \approx \pm 9\hbar$).[48] The quasi-forbidden character of the Q_x/Q_y transition can be lifted by in-plane deformations, giving rise to the lower intensity of $Q_x(0, 0)/Q_y(0, 0)$ compared to $Q_x(1, 0)/Q_y(1, 0)$ denoting transitions to vibrationally excited modes.[9,49] If the near-degeneracy of B_x and B_y is considered, the UV/VIS spectrum of $TCPP^{4-}$ is fully understood.

With X-ray absorption spectroscopy, we are able to probe the electronic structure with atomic precision, enabling a detailed picture of energies and occupancies of the $TCPP^{4-}$ frontier orbitals (Fig. 2c). Opposed to the near-degenerate HOMOs/LUMOs, the aminic and iminic pairs of nitrogen core levels are shifted by as much as 2 eV,[50,51] since the higher electron density at the iminic nitrogens screens the core charge more efficiently.[52] Consequently, the energetically lowest resonance (397.9 eV) in the experimental and calculated ground state N K-edge NEXAFS (Fig. 3a) is of 1s(=N–) $\rightarrow \pi^*$ character. Since only the b_{3g} unoccupied orbital has amplitude at the iminic nitrogens, it is populated by the core electron in this transition. For the same reasons, the 400.0 eV resonance corresponds to the 1s(–NH–) $\rightarrow b_{2g}$ transition. At higher excitation energies less prominent features with only small transient changes are observed (see full spectrum in Fig. S1, ESI†). A detailed interpretation of the ground state spectrum is given elsewhere.[32]

The first $TCPP^{4-}$ transient signal that is probed with the temporal resolution of our setup (0.1 ns in Fig. 3b) is expected to probe the lowest singlet excited state (Q_x). From the parent TPP it is known, that this state is electronically populated and thermally equilibrated in less than 100 fs and 20 ps, respectively, after optical or UV excitation under ambient conditions.[15] The $\pi \rightarrow \pi^*$ transition, leading to the Q_x, opens a new channel for the core excitation, *viz.* the 1s(N) $\rightarrow b_{1u}$ transition, which is equally probable for both iminic and aminic nitrogen sites (Fig. 2c). The former lead to a new feature below the edge of the ground state (396.0 eV). The second feature, corresponding to 1s(–NH–) $\rightarrow b_{1u}$ transitions, overlaps with other transient features (gray bar around 398 eV in Fig. 3b). Potential transitions to a_u are not observed, as this π orbital does not have any amplitude at any nitrogen site. The depletion of the ground state (red bars in Fig. 3b) gives rise to the remaining strong transient features.

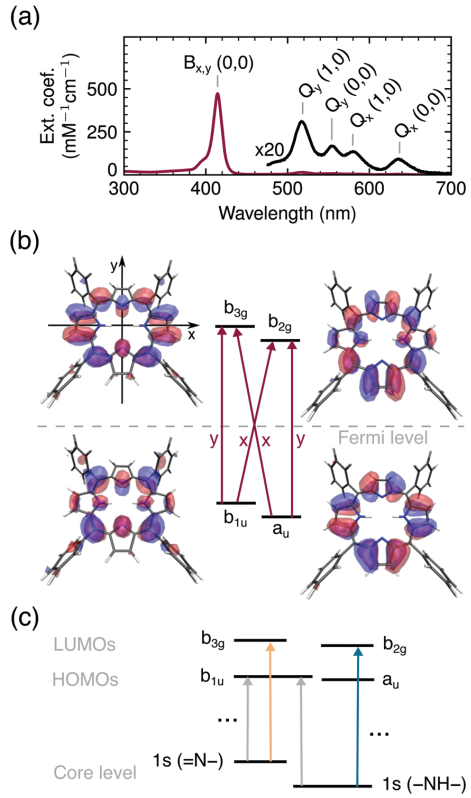

Fig. 2 (a) UV/VIS spectrum of $TCPP^{4-}$. (b) Frontier orbitals with the porphyrin macrocycle in the *xy*-plane and polarization of optical transitions in red. (c) Schematic representation of X-ray induced transitions.

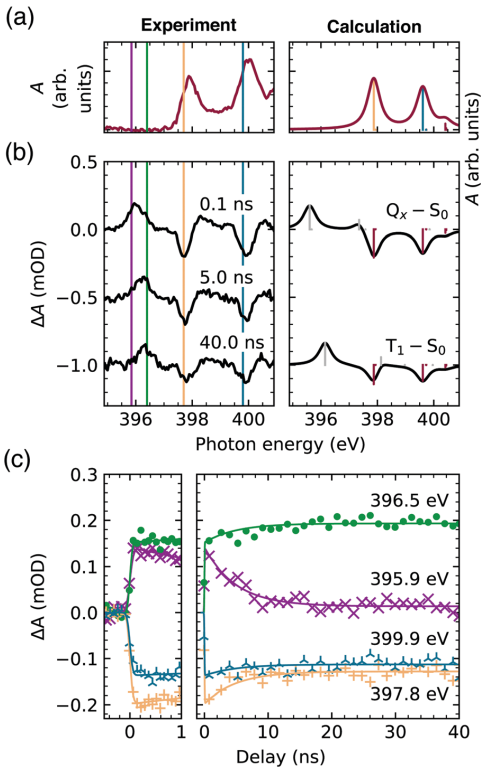

Fig. 3 (a) Ground state $TCPP^{4-}$ N K-edge NEXAFS spectrum. (b) Transient spectra 0.1 ns, 5.0 ns and 40.0 ns after the laser excitation (left) in comparison to the calculated spectra (right). (c) Experimental time traces at the resonance energies.

For increasing delay times of the X-ray probe to the UV excitation (5.0 ns and 40.0 ns in Fig. 3b) the 1s(=N–) → b_{1u} transient feature shifts to higher energies (396.4 eV). This shift is reproduced by the calculations when comparing the lowest singlet (Q_x–S_0) and triplet transient (T_1–S_0) evidencing the direct observation of an intersystem crossing.

Fig. 3c shows the continuous temporal evolution of the transient features until 40 ns after laser excitation. The time traces were fitted by an exponentially modified Gaussian distribution (with an identical lifetime) and a step function being convoluted with the same Gaussian broadening, since a second, slower decay cannot be unambiguously identified within the 40 ns time window. The short-lived component is most prominent in the time evolution of the 396.0 eV feature (probed by the time trace at 395.9 eV, magenta), verifying that this feature is the signature of the lowest singlet excited state. The equivalent feature of the triplet state (probed at 396.5 eV, green) shows a clear delay of the initial increase in absorbance even though it energetically overlaps with the just discussed peak at 396.0 eV. In the case of the two depletions, of which the temporal evolution has been captured at 397.8 eV (orange) and 399.9 eV (blue), the reduction of the absorbance compared to the ground state is observed both in the lowest singlet and triplet excited state.

The global fit of the singlet lifetime yields $\tau_F = 4.9 \pm 0.5$ ns, which is in the range of known TCPP fluorescence lifetimes, *i.e.* from 4.0 ns in organic solvents to 10.4 ns in basic aqueous solution.[19,20,25,53] Our result rather corresponds to the lifetimes in less polar solutions agreeing with the negligible influence of the solvent on the Q_x lifetime, which has recently been established in a review of TPP (and ZnTPP) photophysical properties.[54] Instead, the O_2 saturation of the solution has been considered as the dominant factor – leading to a 23% decrease – of the lifetime of the lowest singlet excited state. However, one of the shorter TCPP lifetimes[19] has been determined in de-aerated solutions, while one of the longer ones in air-equilibrated solution.[53] Also, the influence of aggregation on the Q_x lifetime in our concentrated aqueous solution can be excluded, as TCPP aggregates show fluorescence lifetimes below 1 ns.[53] The large variation indicates that temperature should be considered as the main parameter determining the singlet state lifetime. This supports the proposed vibronic nature of the intersystem crossing in free base porphyrins.[9]

From the time traces, a lower limit for the lifetime of the triplet state can be inferred: $\tau_T > 200$ ns. This agrees with previously observed triplet state lifetimes of $\tau_T > 1$ μs dependent on the oxygen concentration[11,15,55] and triplet–triplet annihilation in concentrated solutions.[56] All determined lifetimes are summarized in Fig. 4a.

For closer analysis of the electronic structure in the two observed excited states, the Q_x and T_1 absorption spectra have been approximated by adding the S_0 spectrum to the transient ones so that the ground state depletion is compensated (see Fig. S2, ESI†). The resulting spectra should be viewed with caution as the spectral intensities depend on Franck–Condon progressions[57–59] and the exact fraction of excited molecules. However, the results gained by this naive approach (Fig. 4b) agree with the calculated electronic configurations (Fig. 4c) and are therefore used as illustration.

From the earlier discussion on the UV/VIS spectrum, the calculated mixture of $^1(b_{1u}\ b_{2g})$ and $^1(a_u\ b_{3g})$ configurations in the Q_x state is expected. The dominance of the former by 27% (Fig. 4c) is supported by the Q_x absorbance in the 1s(N) → b_{3g}/b_{1u} and 1s(N) → b_{2g} energy regions compared to the other states (Fig. 4b). The deviation from the 50 : 50 mixture, being expected in an idealized free electron ring, is a result of the deviations from the pairwise degeneracy of the frontier orbitals.[46] However, as seen from the UV/VIS spectrum, electric dipole transitions between the ground and lowest singlet excited state are still quasi-forbidden. Therefore also fluorescence from this state is unfavorable with a fluorescence quantum yield $\Phi_F \leq 0.25$[11,19,20,25] as supported by the similar intensity of our transient spectra at short and long delays (Fig. 3b and c).

The long lifetime of the singlet state gives rise to the high triplet yield ($\Phi_T = 0.78$[11]) despite the lack of both a heavy atom and close-lying non-ππ* intermediate states which would

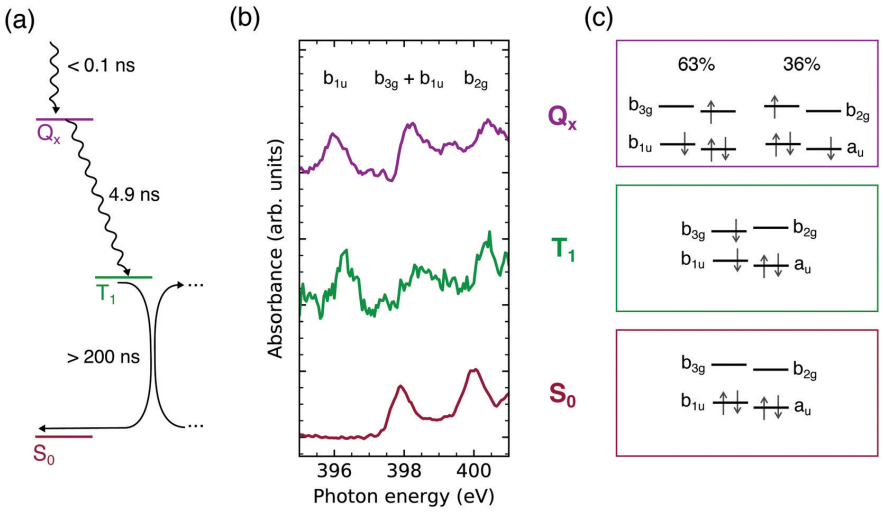

Fig. 4 (a) Jablonski diagram of the $TCPP^{4-}$ deactivation pathway in the nanosecond regime. (b) Approximated X-ray absorption spectra probing the $TCPP^{4-}$ frontier orbital occupation in the lowest singlet excited (Q_x), triplet (T_1), and ground state (S_0). (c) Calculated configurations in these states.

facilitate the process according to El-Sayed's rule.[9,60] Instead, a crossing of the Q_x and $T_{1,2}$ potential energy surfaces along the central proton transfer reaction path was proposed[16] and experimental evidence for the tautomerism has recently been found.[61] Since the spin–orbit coupling matrix element increases to an amount that makes the transition competitive with fluorescence only for out-of plane distortions, thermal activation and a long-lived singlet state are prerequisites for the intersystem crossing.

An intermediate, higher triplet state as a result of the intersystem crossing[16] is not visible within our temporal resolution. Instead, a pure one electron excited state is obtained, as mixing with other configurations is restricted by symmetry in the lowest triplet states.[48,62]

The approximated T_1 spectrum suggests a $^3(b_{1u}\ b_{3g})$ configuration. This is in agreement with studies on TPP[47] and free base 5,10,15,20-tetrakis(4-sulfonatophenyl)porphyrin.[61] For $TCPP^{4-}$ a contraction of the solvation shell upon triplet state formation has been observed,[25] which can be explained by the charge density difference of $^3(b_{1u}\ b_{3g})$ compared to the ground state: b_{1u} (fully occupied in S_0) has equal amplitudes at all nitrogen sites, but b_{3g} (unoccupied in S_0) only at the iminic ones (Fig. 2b). When both molecular orbitals are singly occupied, the charge at the aminic sites decreases. As this strengthens the hydrogen bond between water and the amino group ($H_2O\cdots HN^{\delta+}$), the solvation shell is contracted in the lowest triplet state. This supports the presence of the $^3(b_{1u}\ b_{3g})$ configuration for $TCPP^{4-}$.

It should be noted that the triplet state in non-*meso*-substituted porphyrins is expected to be of $^3(a_u\ b_{3g})$ character, due to the different order of the HOMOs.[47,63,64] In contrast, Kay proposed a $^3(a_u\ b_{3g})$ configuration both for TPP and the parent, unsubstituted porphyrin.[18] Since we only probe the b_{1u} orbital and detect an intense transient feature, this work provides experimental evidence, that the b_{1u} orbital is singly occupied in the lowest triplet state of $TCPP^{4-}$, which also applies to TPP as shown by our calculations. These predict that the $^3(b_{1u}\ b_{3g})$ state is energetically below $^3(b_{1u}\ b_{2g})$ both in the ground state and triplet state geometry, but only in the latter one the order of the LUMOs is inverted.

A reduction of the free base porphyrin symmetry upon intersystem crossing[47] and the resulting exchange of the LUMOs[18] has been discussed in literature. However, out-of-plane distortions in the triplet state compared to the ground state as yielded by our calculations (see Fig. S3, ESI†) have rarely been addressed. Only recently, the importance of such distortions from the planar structure have been shown to be an essential factor for the triplet energy transfer to oxygen:[17] while the porphyrin T_1 vibrational ground state energy is close to the one needed for the excitation of ground state to singlet oxygen, the electron-exchange mechanism is most efficient if this deviation is minimized (resonance condition) by out-of-plane distortions.

In contrast, the electronic structure of the lowest singlet excited state is barley affected by small geometric distortions ensuring that fluorescence is quasi-forbidden. The resulting long lifetime is essential for the application in dye-sensitized solar cells. The charge injection into the conduction band of typically used semiconductors is energetically most favorable from the lowest singlet excited state. Since the decay of that state and charge injection are competing processes, a low decay rate is preferable.[65] On the one hand, this competition can be steered by metal insertion leading to an increase of the electron injection rate. On the other hand, it has been shown that the

main absorption band of free base porphyrins can be tuned to the ''green gap'' between the typical porphyrin absorption bands, to increase the overall efficiency of a solar cell.[1] This feature might be of significant importance for future organic photovoltaics, where the energy of the triplet state can be harnessed.[66] In that case – similar to the application as singlet oxygen photosensitizers – free base porphyrins are advantageous due to their long triplet state lifetimes.[67]

4 Conclusions

The relaxation of aqueous $TCPP^{4-}$ after UV excitation has been observed by N K-edge NEXAFS spectroscopy. The lowest singlet excited state (Q_x) is populated in less than 140 ps after the excitation. Despite of deviations from an ideal square planar porphyrin macrocycle, the 63 : 36 mixture of the $^1(a_u\ b_{3g})$ and $^1(b_{1u}\ b_{2g})$ configurations evidences that the free electron model is applicable. Therefore, fluorescence is forbidden by angular momentum conservation, which gives rise to the long lifetime of this state (4.9 ns).

In dye-sensitized solar cells, the low Q_x decay rate is a prerequisite for the electron injection. In isolated molecules, it enables the high yield of vibronic intersystem crossing by out-of-plane vibrational modes, whose thermal character has been confirmed by the variation of the Q_x lifetimes. The resulting long-lived triplet state ($\tau_T > 200$ ns) is concomitant with a degree of structural bending. As a result the charge density is decreased at the aminic and increased at the iminic nitrogens. Further bending eases the triplet energy transfer to molecular oxygen. The resulting high quantum yield of this process is the basis for the various applications of free base porphyrins as photosensitizers for singlet oxygen generation.

Author contributions

R. B.: data curation, investigation, project administration, visualization, original draft; V. V. C.: calculations; N. G. and A. C.: synthesis, M. F. and R. H.: investigation; M. O. S. and A. F.: conceptualization, funding acquisition, supervision.

Conflicts of interest

There are no conflicts to declare.

Acknowledgements

The authors acknowledge Rolf Mitzner for supporting the MHz laser operation. A. F. and R. B. acknowledge funding from the ERC-ADG-2014 – Advanced Investigator Grant No. 669531 EDAX under the Horizon 2020 EU Framework Program for Research and Innovation. N. G., A. C. and M. O. S. acknowledge support from the Higher Education Authority and the Department of Further and Higher Education, Research, Innovation and Science (Ireland) and the Technical University of Munich – Institute for Advanced Study through a Hans Fischer Senior Fellowship (M. O. S.). The authors thank the Helmholtz-Zentrum Berlin for the allocation of synchrotron radiation beamtime.

References

1 R. Haldar, K. Batra, S. M. Marschner, A. B. Kuc, S. Zahn, R. A. Fischer, S. Bräse, T. Heine and C. Wöll, *Chem. – Eur. J.*, 2019, **25**, 7847–7851.
2 S. Callaghan and M. O. Senge, *Photochem. Photobiol. Sci.*, 2018, **17**, 1490–1514.
3 A. A. Ryan and M. O. Senge, *Photochem. Photobiol. Sci.*, 2015, **14**, 638–660.
4 G. Hu, N. Yalpani, S. P. Briggs and G. S. Johal, *Plant Cell*, 1998, **10**, 1095–1105.
5 D. Todd, *Br. J. Dermatol.*, 1994, **131**, 751–766.
6 R. Bonnett, *Chem. Soc. Rev.*, 1995, **24**, 19–33.
7 E. F. F. Silva, C. Serpa, J. M. Dabrowski, C. J. P. Monteiro, S. J. Formosinho, G. Stochel, K. Urbanska, S. Simões, M. M. Pereira and L. G. Arnaut, *Chem. – Eur. J.*, 2010, **16**, 9273–9286.
8 Y. N. Hsiang, M. T. Crespo, A. M. Richter, A. K. Jain, M. Fragoso and J. G. Levy, *Photochem. Photobiol.*, 1993, **57**, 670–674.
9 T. J. Penfold, E. Gindensperger, C. Daniel and C. M. Marian, *Chem. Rev.*, 2018, **118**, 6975–7025.
10 S. A. G. Lambrechts, M. C. G. Aalders and J. V. Marle, *Antimicrob. Agents Chemother.*, 2005, **49**, 2026–2034.
11 J. Mosinger, V. Kliment, J. Sejbal, P. Kubát and K. Lang, *J. Porphyrins Phthalocyanines*, 2002, **06**, 514–526.
12 D. Malara, C. Mielke, M. Oelgemöller, M. O. Senge and K. Heimann, *Aquacult. Res.*, 2017, **48**, 2954–2962.
13 R. Gerdes, D. Wöhrle, W. Spiller, G. Schneider, G. Schnurpfeil and G. Schulz-Ekloff, *J. Photochem. Photobiol., A*, 1997, **111**, 65–74.
14 W. Li, N. Gandra, E. D. Ellis, S. Courtney, S. Li, E. Butler and R. Gao, *ACS Appl. Mater. Interfaces*, 2009, **1**, 1778–1784.
15 J. S. Baskin, H.-Z. Yu and A. H. Zewail, *J. Phys. Chem. A*, 2002, **106**, 9837–9844.
16 S. Perun, J. Tatchen and C. M. Marian, *Chemphyschem*, 2008, **9**, 282–292.
17 F. Zapata, M. Nucci, O. Castaño, M. Marazzi and L. M. Frutos, *J. Chem. Theory Comput.*, 2021, **17**, 5429–5439.
18 C. W. M. Kay, *J. Am. Chem. Soc.*, 2003, **125**, 13861–13867.
19 P. G. Mahajan, N. C. Dige, B. D. Vanjare, A. R. Phull, S. J. Kim, S.-K. Hong and K. H. Lee, *J. Fluoresc.*, 2018, **28**, 871–882.
20 T. L. C. Figueiredo, R. A. W. Johnstone, A. M. P. S. Sørensen, D. Burget and P. Jacques, *Photochem. Photobiol.*, 1999, **69**, 517–528.
21 A. A. Cordones, C. D. Pemmaraju, J. H. Lee, I. Zegkinoglou, M.-E. Ragoussi, F. J. Himpsel, G. de la Torre and R. W. Schoenlein, *J. Phys. Chem. Lett.*, 2021, **12**, 1182–1188.
22 V. Vaz da Cruz, S. Eckert and A. Föhlisch, *Phys. Chem. Chem. Phys.*, 2021, **23**, 1835–1848.

23 P. Deria, J. Yu, R. P. Balaraman, J. Mashni and S. N. White, *Chem. Commun.*, 2016, **52**, 13031–13034.
24 Y. Keum, S. Park, Y.-P. Chen and J. Park, *Angew. Chem., Int. Ed.*, 2018, **57**, 14852–14856.
25 M. M. Kruk and S. E. Braslavsky, *Photochem. Photobiol. Sci.*, 2012, **11**, 972–978.
26 A. Pietzsch and S. Eisebitt, *J. Large-Scale Res. Facil.*, 2016, **2**, A54.
27 K. Kunnus, I. Rajkovic, S. Schreck, W. Quevedo, S. Eckert, M. Beye, E. Suljoti, C. Weniger, C. Kalus, S. Grübel, M. Scholz, D. Nordlund, W. Zhang, R. W. Hartsock, K. J. Gaffney, W. F. Schlotter, J. J. Turner, B. Kennedy, F. Hennies, S. Techert, P. Wernet and A. Föhlisch, *Rev. Sci. Instrum.*, 2012, **83**, 123109.
28 M. Fondell, S. Eckert, R. M. Jay, C. Weniger, W. Quevedo, J. Niskanen, B. Kennedy, F. Sorgenfrei, D. Schick, E. Giangrisostomi, R. Ovsyannikov, K. Adamczyk, N. Huse, P. Wernet, R. Mitzner and A. Föhlisch, *Struct. Dyn.*, 2017, **4**, 054902.
29 P. S. Miedema, W. Quevedo and M. Fondell, *J. Large-Scale Res. Facil.*, 2016, **2**, A27.
30 R. Flesch, A. A. Pavlychev, J. J. Neville, J. Blumberg, M. Kuhlmann, W. Tappe, F. Senf, O. Schwarzkopf, A. P. Hitchcock and E. Rühl, *Phys. Rev. Lett.*, 2001, **86**, 3767–3770.
31 A. W. Gillespie, F. L. Walley, R. E. Farrell, T. Z. Regier and R. I. R. Blyth, *J. Synchrotron Radiat.*, 2008, **15**, 532–534.
32 R. Büchner, M. Fondell, R. Haverkamp, A. Pietzsch, V. Vaz da Cruz and A. Föhlisch, *Phys. Chem. Chem. Phys.*, 2021, **23**, 24765–24772.
33 M. V. Nardi, R. Verucchi, L. Pasquali, A. Giglia, G. Fronzoni, M. Sambi, G. Mangione and M. Casarin, *Phys. Chem. Chem. Phys.*, 2015, **17**, 2001–2011.
34 F. Neese, *Wiley Interdiscip. Rev.: Comput. Mol. Sci.*, 2012, **2**, 73–78.
35 V. Barone and M. Cossi, *J. Phys. Chem. A*, 1998, **102**, 1995–2001.
36 A. D. Becke, *J. Chem. Phys.*, 1993, **98**, 5648–5652.
37 P. J. Stephens, F. J. Devlin, C. F. Chabalowski and M. J. Frisch, *J. Chem. Phys.*, 1994, **98**, 11623–11627.
38 F. Weigend and R. Ahlrichs, *Phys. Chem. Chem. Phys.*, 2005, **7**, 3297–3305.
39 F. Weigend, *Phys. Chem. Chem. Phys.*, 2006, **8**, 1057–1065.
40 S. Grimme, J. Antony, S. Ehrlich and H. Krieg, *J. Chem. Phys.*, 2010, **132**, 154104.
41 S. Grimme, S. Ehrlich and L. Goerigk, *J. Comput. Chem.*, 2011, **32**, 1456–1465.
42 T. Lu and F. Chen, *J. Comput. Chem.*, 2012, **33**, 580–592.
43 C. Nicolas and C. Miron, *J. Electron Spectrosc. Relat. Phenom.*, 2012, **185**, 267–272.
44 M. Gouterman, *J. Chem. Phys.*, 1959, **30**, 1139–1161.
45 A. Ghosh, *Angew. Chem., Int. Ed.*, 2021, **60**, 9760–9770.
46 M. Gouterman, *J. Mol. Spectrosc.*, 1961, **6**, 138–163.
47 J. C. De Paula, V. A. Walters, C. Nutaitis, J. Lind and K. Hall, *J. Phys. Chem.*, 1992, **96**, 10591–10594.
48 M. Gouterman, *Ann. N. Y. Acad. Sci.*, 1973, **206**, 70–83.
49 B. Minaev, Y.-H. Wang, C.-K. Wang, Y. Luo and H. Ågren, *Spectrochim. Acta, Part A*, 2006, **65**, 308–323.
50 M. V. Zeller and R. G. Hayes, *J. Am. Chem. Soc.*, 1973, **95**, 3855–3860.
51 M. Nardi, R. Verucchi, C. Corradi, M. Pola, M. Casarin, A. Vittadini and S. Iannotta, *Phys. Chem. Chem. Phys.*, 2010, **12**, 871–880.
52 R. Büchner, M. Fondell, E. J. Mascarenhas, A. Pietzsch, V. Vaz da Cruz and A. Föhlisch, *J. Phys. Chem. B*, 2021, **125**, 2372–2379.
53 R. F. Khairutdinov and N. Serpone, *J. Phys. Chem. B*, 1999, **103**, 761–769.
54 M. Taniguchi, J. S. Lindsey, D. F. Bocian and D. Holten, *J. Photochem. Photobiol., C.*, 2021, **46**, 100401.
55 R. Burgner and A. Ponte Goncalves, *Chem. Phys. Lett.*, 1977, **46**, 275–278.
56 S. E. J. Bell, C. B. Aakeröy, A. H. R. Al-Obaidi, J. N. M. Hegarty, J. J. McGarvey, C. R. Lefley, J. N. Moore and R. E. Hester, *J. Chem. Soc., Faraday Trans.*, 1995, **91**, 411–418.
57 F. K. Gel'Mukhanov, L. Mazalov and A. Kondratenko, *Chem. Phys. Lett.*, 1977, **46**, 133–137.
58 J. Stöhr, *NEXAFS Spectroscopy*, Springer, San Jose, 1992.
59 V. Vaz da Cruz, N. Ignatova, R. C. Couto, D. A. Fedotov, D. R. Rehn, V. Savchenko, P. Norman, H. Ågren, S. Polyutov, J. Niskanen, S. Eckert, R. M. Jay, M. Fondell, T. Schmitt, A. Pietzsch, A. Föhlisch, F. Gel'mukhanov, M. Odelius and V. Kimberg, *J. Chem. Phys.*, 2019, **150**, 234301.
60 M. A. El-Sayed, *J. Chem. Phys.*, 1963, **38**, 2834–2838.
61 A. Barbon, M. G. Dal Farra, S. Ciuti, M. Albertini, L. Bolzonello, L. Orian and M. Di Valentin, *J. Chem. Phys.*, 2020, **152**, 034201.
62 M. Gouterman, *Optical Spectra and Electronic Structure of Porphyrins and Related Rings*, Academic Press, New York, 1978, vol. 3, pp. 1–165.
63 O. Ohno, Y. Kaizu and H. Kobayashi, *J. Chem. Phys.*, 1985, **82**, 1779–1787.
64 J. G. Radziszewski, J. Waluk, M. Nepras and J. Michl, *J. Phys. Chem.*, 1991, **95**, 1963–1969.
65 T. D. Santos, A. Morandeira, S. Koops, A. J. Mozer, G. Tsekouras, Y. Dong, P. Wagner, G. Wallace, J. C. Earles, K. C. Gordon, D. Officer and J. R. Durrant, *J. Phys. Chem. C*, 2010, **114**, 3276–3279.
66 C.-M. Yang, C.-H. Wu, H.-H. Liao, K.-Y. Lai, H.-P. Cheng, S.-F. Horng, H.-F. Meng and J.-T. Shy, *Appl. Phys. Lett.*, 2007, **90**, 133509.
67 S. Mathai, T. A. Smith and K. P. Ghiggino, *Photochem. Photobiol. Sci.*, 2007, **6**, 995–1002.

5 Conclusion

In this thesis, electronic structure variations within two classes of aromatic molecules were assessed: pyridones and porphyrins. The issue of an accurate theoretical description of the electron delocalization in aromatic compounds has been addressed by chemical physics since its very beginning. Experimentally, the characteristic optical bands have long been used to access the electronic structure, but limited the view to global transitions between frontier orbitals. X-ray spectroscopy allows to project a wide range of occupied and unoccupied states onto specific chemical sites, enabling a fundamental understanding of the origins of the electronic structure variations. In detail, RIXS and NEXAFS at the K-edge of the nitrogen heteroatom in aromatic systems were used to probe the local density of states and their response to isomerism, complex formation, solvation, and optical excitation.

Upon all influencing factors of the charge itinerance and localization, the chemical composition of a molecule is naturally most important. In the discussed bio-inspired molecules, the nitrogen heteroatom introduces reactivity into the stable, parent benzene ring giving rise to tautomerism and complexation. In publication I, the prototypical keto-enol tautomerism of the three HP/PO isomers and their acidity were investigated. In the N K-edge NEXAFS spectra, the species differ mainly by the position of the π^* resonance, which is firstly dependent on the charge at the probed atom. The resulting shift between the protonated and deprotonated nitrogen sites has meanwhile been established as a general trend for aromatic molecules [33]. Secondly, the resonance position is influenced by the relaxation of the core-excited state, revealing a marginal influence of the per se highly electron attracting oxygen site in 3PO. This interpretation is supported by CASSCF calculations and confirms the reduced conjugation of the oxygen site in this isomer. The resulting reduced stability of 3PO is a decisive factor for the isomeric differences.

The 3HP/3PO equilibrium was further examined in publication II. RIXS at the nitrogen proton transfer site was used to probe the density and symmetry of occupied states for each tautomer individually by utilizing the site selectivity and polarization anisotropy of the scattering process. In combination

with RSA-TD-DFT calculations, a polarization inversion between the tautomers has been uncovered: The charge density is significantly increased at the respectively protonated site. The retrieved, detailed information on the electronic structure of both tautomers emphasizes that the described method is expected to be valuable for the investigation of tautomeric systems, in general.

Publication III concentrates on the influence of different central moieties on hybridization in the porphyrin complex. N K-edge NEXAFS spectroscopy is shown to be ideally suited to characterize the electronic structure beyond the frontier orbitals, which are accessible by UV/VIS spectroscopy and well-described by the Gouterman model. Consequently, the interpretation of the NEXAFS features being caused by transitions to higher unoccupied states has been debated in the past. By a systematic variation of biorelevant metal centers in combination with a benchmark of TD-DFT and TP-DFT calculations with a number of functionals, a consistent interpretation of the NEXAFS features is achieved. Based on this assignment, the metal-ligand covalency of porphyrins (Ps) can be seen to increase from MgP to ZnP to CuP. For the conjugation of peripheral substituents an opposite trend is observed: the lower the central covalency the higher the charge localization on the porphyrin ligand.

The proposed regulating role of the metal ion allows to comprehend the need for different central moieties for the versatile applications of this class of molecules: The ionicity of the $Mg^{2+}P^{2-}$ complex eases the charge transfer in the closely related chlorophyll molecule during photosynthesis, but also causes a rather low stability. Transition metal porphyrins have a strong metal-ligand bond, which explains why heme (FeP) is used for oxygen transport in blood. The compensation of different oxidation states of the central metal atom during the respiratory process is supported by π hybridization with substituents, as also indicated by Johansson et al.. If iron is scarce the body synthesizes ZnP[90], which has a reduced covalency of the central complex concomitant with similar photophysical properties to H_2P and MgP. The resulting strong fluorescence upon optical excitation is utilized to detect an iron deficiency in medical diagnosis[59].

In addition to the effect of these intramolecular constitutional changes, the modification of the electronic structure as a consequence of hydrogen bonding and optical excitations has been studied. The nature of hydrogen bonding – of which the covalent character is still of scientific debate[3] – has been further clarified in publication I. A correlation between the intensity of hydrogen bond interactions and acidity was established, confirming that the hydrogen bond $X{-}Y\cdots Y$ is a step towards the proton transfer forming $X^{-}\cdots H{-}Y^{+}$[116]. X and Y denote a PO and a water molecule, respectively, in that specific case.

By the inclusion of hydrogen bonding via minimally solvated models (provided by molecular dynamics simulations), the macroscopic HP/PO tautomeric constants and acidities have been traced back on the microscopic interplay of the inherent charge density and orbital re-hybridization upon solvation. The charge localization in 3PO and steric hindrance of hydration in 2PO are identified as driving factors for the three orders of magnitude difference regarding the tautomeric constant and acidity between the isomers. The electronic structure and hydrogen bond analysis of the PO series has later been used by Tang et al. to unravel the catalytic activity of PO-based ionic liquids.

Since the genetic information in DNA and RNA is contained in the hydrogen bond pattern between the nucleobases, which show large structural similarities – especially with 2PO, these findings also have biological implications[135]. The exceptional stability of the protonation state of this isomer is crucial,

since both tautomerism and acidity of nucleobases can alter the DNA hydrogen bond pattern causing for example diseases or mutations [88,115,96]. Additionally, the orbital rehybridization upon hydrogen bond formation of pyridones (publication II) helps to explain the increased aromaticity of nucleobases in the DNA hydrogen bond network [21] by a reduction of the π charge density at the nitrogen site, which makes the molecule more benzene-like.

In contrast to pyridones, the class of porphyrins exhibits rather low hydrogen bond abilities due to the low polarity. This eases the incorporation into proteins e.g. heme into hemoglobin, but also inhibits the excretion in case of an impaired porphyrin metabolism, which can lead to accumulation of the free base porphyrin in the body resulting in hepatic disease and a pathological photosensitivity – colloquially referred to as "vampire disease" [143]. The cause for the initial absorption of UV/VIS photons is – analogous to chlorophyll during photosynthesis – the large aromatic system.

The relaxation pathway of the photoexcited free base porphyrin macrocycle has been studied by transient NEXAFS spectroscopy in publication IV. The experimental data confirm an unusually long lifetime of the first singlet excited state, which can be understood by the angular momentum forbidden decay in the free electron ring model. The long lifetime is essential for the charge injection in dye-sensitized solar cells. After about 5 ns the dissolved molecule undergoes efficient intersystem crossing to the lowest triplet excited state even though this transition is El-Sayed forbidden and not facilitated by a heavy atom. Instead, a vibronic coupling mechanism was proposed by Perun et al., which is supported by the presumably temperature-dependent variation of the singlet state lifetime in the presented measurements and related studies. By the calculation of the excited states by the RSA-TD-DFT approach, an inversion of the unoccupied frontier orbitals is observed in the geometrically distorted triplet excited state. Such a bent structure is expected to facilitate the triplet energy transfer to ground state molecular oxygen forming reactive singlet oxygen, which is utilized in photodynamic therapy and green chemistry. Thereby, the structure-function interplay, electronic configurations, and lifetimes during the de-excitation of free base porphyrin have been uncovered.

Overall, this thesis establishes, that even though the investigated aromatic molecules differ largely by their optical absorption bands and hydrogen bonding abilities, they all share a global stabilization of local constitutional changes and the respectively relevant external perturbation. This allows molecules, which are part of the pyridone and porphyrin classes of highly similar compounds, to fulfill their specific function in the diverse biological or technical processes driven by these groups of substances.

In the future, it will be of scientific relevance to apply the presented methods to a wider group of bio-inspired aromatic molecules. Especially the study of the relaxation pathway of further biologically relevant porphyrins and nucleobases will contribute to a more fundamental understanding of natural light-harvesting applications and light-induced damage of tissue and genetic material. Besides the need for more exploratory studies, publication I and III show the power of systemic investigations to provide a consistent interpretation of spectral features with direct implications on the conception of charge distribution and its role in natural and artificial processes. While this thesis concentrates on groups of reduced biological systems, specific modifications e.g. of substituents, the oxidation number of a metal center in a complex, or solvent polarity are expected to reveal fundamental links between structure and function in aromatic molecules.

Another trend in physical chemistry is the investigation of aromatic systems of increasing size. Anal-

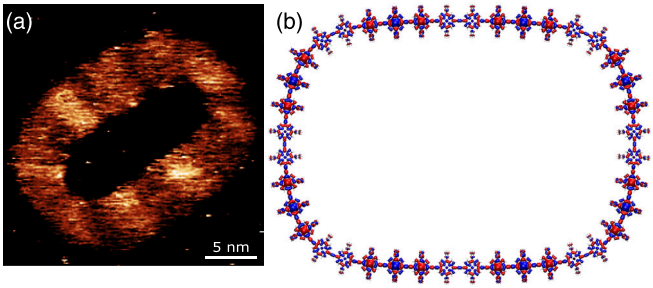

Figure 5.1: a) Differential (scanning tunneling microscopy) conduction map of stacked 40-membered cyclic zinc porphyrin oligomers at sample bias -1.1 V. b) Structure of a single layer with the corresponding calculated molecular orbital (HOMO-8). Adapted from Judd et al. (https://doi.org/10.1103/PhysRevLett.125.206803, CC BY 4.0).

ogous to their linear counterparts [57,144], the reduction of bond delocalization in aromatic molecules was expected for ones larger than porphyrins until 2016 [154]. By the clear signature of the aromatic ring current in nuclear magnetic resonance (NMR) spectroscopy, zinc-porphyrin-based molecules with 62 [160] and recently also 162 π electron systems were confirmed [160].

Figure 5.1a shows the scanning tunneling microscopy image of a stack of 40-membered cyclic zinc porphyrin oligomers [72]. The bias voltage is chosen, so that the electron density around the HOMO-8 orbital is probed, which is shown in Figure 5.1b. Even though the resolution is not sufficient to probe the individual nodes of the electronic wave function, the intensity pattern resembles that of a free electron ring and shows that global charge delocalization exists in these 20 nm sized rings.

The confirmation of the validity of Hückel's rule for aromatic systems of increasing size reaches into the field of mesoscopic physics. Approximately 500 nm sized metal rings in a magnetic field have been shown to comprise ring currents, which are predicted to follow the same pattern as aromatic compounds [95]. The analogy of aromatic systems and superconducting quantum rings goes back to London [38]. Both a fundamental understanding of aromatic properties, as promoted by this thesis, and further studies with the aim to bridge the gap to mesoscopic physics pave the way for innovations in molecular electronics [69].

The aim to comprehend increasingly complex biomolecular systems is equally fascinating as the extension of aromatic physical chemistry into the mesoscopic scale. The presented RIXS spectra of dilute samples and transient NEXAFS results with picosecond time resolution are close to the edge of feasibility with the brilliance and time resolution of third-generation synchrotron light sources. Follow-up studies are thus expected to benefit from the continuous development of instrumental methods, such as the increasing availability and brilliance of coherent X-ray sources enabling to observe ultrafast processes. The METRIXS and hRIXS spectrometers, which have been initially commissioned as part of this thesis, will soon provide access to vibrational excitations yielding potential energy surfaces of organic substances in solution. Thereby the understanding of the influencing factors and effects of the electronic structure in a wide range of bio-inspired aromatic molecules will be facilitated.

References

[1] Albert, A. & Phillips, J. N. (1956). Ionization constants of heterocyclic substances. Part II. Hydroxy-derivatives of nitrogenous six-membered ring-compounds. *J. Chem. Soc.*, (0), 1294 – 1304.

[2] Ament, L. J. P., van Veenendaal, M., Devereaux, T. P., Hill, J. P., & van den Brink, J. (2011). Resonant inelastic x-ray scattering studies of elementary excitations. *Rev. Mod. Phys.*, 83, 705–767.

[3] Atkins, P. W. & de Paula, J. (2011). *Physical Chemistry for the Life Sciences*. Oxford: Oxford University Press, second edition.

[4] Atkins, P. W., de Paula, J., & Keeler, J. (2018). *Atkins' physical chemistry*. Oxford: Oxford University Press, eleventh edition.

[5] Atkins, P. W. & Friedman, R. (2011). *Molecular quantum mechanics*. Oxford: Oxford University Press, fifth edition.

[6] Attwood, D. & Sakdinawat, A. (2016). *X-rays and extreme ultraviolet radiation: principles and applications*. Cambridge: Cambridge University Press, second edition.

[7] Azenha, E. G., Serra, A. C., Pineiro, M., Pereira, M. M., Seixas de Melo, J., Arnaut, L. G., Formosinho, S. J., & Rocha Gonsalves, A. (2002). Heavy-atom effects on metalloporphyrins and polyhalogenated porphyrins. *Chem. Phys.*, 280(1), 177–190.

[8] Barlin, G. B. & Pfleiderer, W. (1971). Ionization constants of heterocyclic substances. Part IX. Protonation of aminopyridones and aminopyrimidones. *J. Chem. Soc. B*, (0), 1425–1432.

[9] Barone, V. & Cossi, M. (1998). Quantum calculation of molecular energies and energy gradients in solution by a conductor solvent model. *J. Phys. Chem. A*, 102(11), 1995–2001.

[10] Beak, P. (1977). Energies and alkylations of tautomeric heterocyclic compounds: Old problems–new answers. *Acc. Chem. Res.*, 10(5), 186–192.

[11] Beak, P., Fry, F. S., Lee, J., & Steele, F. (1976). Equilibration studies. protomeric equilibria of 2- and 4-hydroxypyridines, 2- and 4-hydroxypyrimidines, 2- and 4-mercaptopyridines, and structurally related compounds in the gas phase. *J. Am. Chem. Soc.*, 98(1), 171–179.

[12] Becke, A. D. (1988). Density-functional exchange-energy approximation with correct asymptotic behavior. *Phys. Rev. A*, 38, 3098–3100.

[13] Becke, A. D. (1993). A new mixing of Hartree–Fock and local density-functional theories. *J. Chem. Phys.*, 98(2), 1372–1377.

[14] Bonnett, R. (1995). Photosensitizers of the porphyrin and phthalocyanine series for photodynamic therapy. *Chem. Soc. Rev.*, 24, 19–33.

[15] Born, M. & Oppenheimer, R. (1927). Zur Quantentheorie der Molekeln. *Ann. Phys.*, 389(20), 457–484.

[16] Brumboiu, I. E., Prokopiou, G., Kronik, L., & Brena, B. (2017). Valence electronic structure of cobalt phthalocyanine from an optimally tuned range-separated hybrid functional. *J. Chem. Phys.*, 147(4), 044301.

[17] Cai, Z.-L., Crossley, M. J., Reimers, J. R., Kobayashi, R., & Amos, R. D. (2006). Density functional theory for charge transfer: The nature of the N-bands of porphyrins and chlorophylls revealed through CAM-B3LYP, CASPT2, and SAC-CI calculations. *J. Phys. Chem. B*, 110(31), 15624–15632.

[18] Callaghan, S. & Senge, M. O. (2018). The good, the bad, and the ugly – controlling singlet oxygen through design of photosensitizers and delivery systems for photodynamic therapy. *Photochem. Photobiol. Sci.*, 17, 1490–1514.

[19] Chen, Z., Wannere, C. S., Corminboeuf, C., Puchta, R., & von Ragué Schleyer, P. (2005). Nucleus-independent chemical shifts (NICS) as an aromaticity criterion. *Chem. Rev.*, 105(10), 3842–3888.

[20] Cossi, M., Rega, N., Scalmani, G., & Barone, V. (2003). Energies, structures, and electronic properties of molecules in solution with the C-PCM solvation model. *J. Comput. Chem.*, 24(6), 669–681.

[21] Cyrański, M. K., Gilski, M., Jaskólski, M., & Krygowski, T. M. (2003). On the aromatic character of the heterocyclic bases of DNA and RNA. *J. Org. Chem.*, 68(22), 8607–8613.

[22] Dashwood, R. (1997). Chlorophylls as anticarcinogens. *Int. J. Oncol.*, 10(4), 721–727.

[23] de Groot, F. & Kotani, A. (2008). *Core level spectroscopy of solids*. Boca Raton: CRC Press.

[24] de Souza, J. R., de Moraes, M. M. F., Aoto, Y. A., & Homem-de Mello, P. (2020). Can one use the electronic absorption spectra of metalloporphyrins to benchmark electronic structure methods? A case study on the cobalt porphyrin. *Phys. Chem. Chem. Phys.*, 22, 23886–23898.

[25] Demtröder, W. (2008). *Experimentalphysik 1 Mechanik und Wärme*. Kaiserslautern: Springer Spektrum.

[26] Dirac, P. A. M. (1927). The quantum theory of the emission and absorption of radiation. *Proc. R. Soc. London, Ser. A*, 114(767), 243–265.

[27] Docken, K. K. & Hinze, J. (1972). LiH potential curves and wavefunctions for $X\,^1\Sigma^+$, $A\,^1\Sigma^+$, $B\,^1\Pi$, $^3\Sigma^+$, and $^3\Pi$. *J. Chem. Phys.*, 57(11), 4928–4936.

[28] Dou, L., Liu, Y., Hong, Z., Li, G., & Yang, Y. (2015). Low-bandgap near-IR conjugated polymers/molecules for organic electronics. *Chem. Rev.*, 115(23), 12633–12665.

[29] Dreuw, A. & Head-Gordon, M. (2005). Single-reference ab initio methods for the calculation of excited states of large molecules. *Chem. Rev.*, 105(11), 4009–4037.

[30] Eckert, S., Miedema, P., Quevedo, W., O'Cinneide, B., Fondell, M., Beye, M., Pietzsch, A., Ross, M., Khalil, M., & Föhlisch, A. (2016). Molecular structures and protonation state of 2-mercaptopyridine in aqueous solution. *Chem. Phys. Lett.*, 647, 103–106.

[31] Eckert, S., Norell, J., Jay, R. M., Fondell, M., Mitzner, R., Odelius, M., & Föhlisch, A. (2019). T1 population as the driver of excited-state proton-transfer in 2-thiopyridone. *Chem. Eur. J.*, 25(7), 1733–1739.

[32] Eckert, S., Vaz da Cruz, V., Gel'mukhanov, F., Ertan, E., Ignatova, N., Polyutov, S., Couto, R. C., Fondell, M., Dantz, M., Kennedy, B., Schmitt, T., Pietzsch, A., Odelius, M., & Föhlisch, A. (2018). One-dimensional cuts through multidimensional potential-energy surfaces by tunable x rays. *Phys. Rev. A*, 97, 053410.

[33] Eckert, S., Vaz da Cruz, V., Ochmann, M., von Ahnen, I., Föhlisch, A., & Huse, N. (2021). Breaking the symmetry of pyrimidine: Solvent effects and core-excited state dynamics. *J. Phys. Chem. Lett.*, 12(35), 8637–8643.

[34] Ehlert, C., Gühr, M., & Saalfrank, P. (2018). An efficient first principles method for molecular pump-probe NEXAFS spectra: Application to thymine and azobenzene. *J. Chem. Phys.*, 149(14), 144112.

[35] Ehlert, C. & Klamroth, T. (2020). PSIXAS: A Psi4 plugin for efficient simulations of X-ray absorption spectra based on the transition-potential and Δ-Kohn–Sham method. *J. Comput. Chem.*, 41(19), 1781–1789.

[36] Ekimova, M., Quevedo, W., Faubel, M., Wernet, P., & Nibbering, E. T. J. (2015). A liquid flatjet system for solution phase soft-x-ray spectroscopy. *Struct. Dyn.*, 2(5), 054301.

[37] Fermi, E. (1950). *Nuclear physics*. Chicago: University of Chicago Press.

[38] Fomin, V. M., Ed. (2014). *Physics of Quantum Rings*, (pp. 1–3). Springer: Berlin.

[39] Fondell, M., Eckert, S., Jay, R. M., Weniger, C., Quevedo, W., Niskanen, J., Kennedy, B., Sorgenfrei, F., Schick, D., Giangrisostomi, E., Ovsyannikov, R., Adamczyk, K., Huse, N., Wernet, P., Mitzner, R., & Föhlisch, A. (2017). Time-resolved soft X-ray absorption spectroscopy in transmission mode on liquids at MHz repetition rates. *Struct. Dyn.*, 4(5), 054902.

[40] Fox, H. M. & Gardiner, J. S. (1926). Chlorocruorin: A pigment allied to haemoglobin. *Proc. R. Soc. London, Ser. B*, 99(696), 199–220.

[41] Fransson, T., Brumboiu, I. E., Vidal, M. L., Norman, P., Coriani, S., & Dreuw, A. (2021). XABOOM: An X-ray absorption benchmark of organic molecules based on carbon, nitrogen, and oxygen 1s $\rightarrow \pi^*$ transitions. *J. Chem. Theory Comput.*, 17(3), 1618–1637.

[42] Gainar, A., Stevens, J. S., Jaye, C., Fischer, D. A., & Schroeder, S. L. M. (2015). NEXAFS sensitivity to bond lengths in complex molecular materials: A study of crystalline saccharides. *J. Phys. Chem. B*, 119(45), 14373–14381.

[43] Gajewska, B., Raccio, S., Rodriguez, K. J., & Bruns, N. (2019). Chlorophyll derivatives as catalysts and comonomers for atom transfer radical polymerizations. *Polym. Chem.*, 10, 125–135.

[44] Garratt, P. J. (1986). *Aromaticity*. New York: John Wiley & Sons.

[45] Gel'mukhanov, F. & Ågren, H. (1994). Resonant inelastic x-ray scattering with symmetry-selective excitation. *Phys. Rev. A*, 49, 4378–4389.

[46] Gel'mukhanov, F., Odelius, M., Polyutov, S. P., Föhlisch, A., & Kimberg, V. (2021). Dynamics of resonant x-ray and auger scattering. *Rev. Mod. Phys.*, 93, 035001.

[47] Gel'mukhanov, F. & Ågren, H. (1999). Resonant X-ray Raman scattering. *Phys. Rep.*, 312(3), 87–330.

[48] Ghosh, A. (2021). An exemplary gay scientist and mentor: Martin Gouterman (1931–2020). *Angew. Chem., Int. Ed.*, 60(18), 9760–9770.

[49] Golnak, R., Xiao, J., Atak, K., Stevens, J. S., Gainar, A., Schroeder, S. L. M., & Aziz, E. F. (2015). Intermolecular bonding of hemin in solution and in solid state probed by N K-edge X-ray spectroscopies. *Phys. Chem. Chem. Phys.*, 17, 29000–29006.

[50] Gouterman, M. (1973). Angular momentum, magnetic interactions, Jahn-Teller and environment effects in metalloporphyrin triplet states. *Ann. N. Y. Acad. Sci.*, 206(1), 70–83.

[51] Gouterman, M. (1978). *Optical Spectra and Electronic Structure of Porphyrins and Related Rings*, volume 3, (pp. 1–165). Academic Press: New York.

[52] Grätzel, M. (2003). Dye-sensitized solar cells. *J. Photochem. Photobiol. C: Photochem. Rev.*, 4(2), 145–153.

[53] Hähner, G. (2006). Near edge X-ray absorption fine structure spectroscopy as a tool to probe electronic and structural properties of thin organic films and liquids. *Chem. Soc. Rev.*, 35, 1244–1255.

[54] Haldar, R., Batra, K., Marschner, S. M., Kuc, A. B., Zahn, S., Fischer, R. A., Bräse, S., Heine, T., & Wöll, C. (2019). Bridging the green gap: metal–organic framework heteromultilayers assembled from porphyrinic linkers identified by using computational screening. *Chem. Eur. J.*, 25(33), 7847–7851.

[55] Hanson-Heine, M. W. D., George, M. W., & Besley, N. A. (2018). Assessment of time-dependent density functional theory with the restricted excitation space approximation for excited state calculations of large systems. *Mol. Phys.*, 116(11), 1452–1459.

[56] Hartree, D. R. & Hartree, W. (1935). Self-consistent field, with exchange, for beryllium. *Proc. R. Soc. London, Ser. A*, 150(869), 9–33.

[57] Heckmann, A. & Lambert, C. (2012). Organic mixed-valence compounds: A playground for electrons and holes. *Angew. Chem., Int. Ed.*, 51(2), 326–392.

[58] Henke, B., Gullikson, E., & Davis, J. (1993). X-ray interactions: Photoabsorption, scattering, transmission, and reflection at E = 50-30,000 eV, Z = 1-92. *At. Data Nucl. Data Tables*, 54(2), 181–342.

[59] Hennig, G., Homann, C., Teksan, I., Hasbargen, U., Hasmüller, S., Holdt, L. M., Khaled, N., Sroka, R., Stauch, T., Stepp, H., Vogeser, M., & Brittenham, G. M. (2016). Non-invasive detection of iron deficiency by fluorescence measurement of erythrocyte zinc protoporphyrin in the lip. *Nat. Commun.*, 7(1), 10776.

[60] Hertel, I. V. & Schulz, C.-P. (2008). *Atome, Moleküle und optische Physik 1*. Berlin: Springer.

[61] Hohenberg, P. & Kohn, W. (1964). Inhomogeneous electron gas. *Phys. Rev.*, 136, B864–B871.

[62] Hospital, A., Goñi, J. R., Orozco, M., & Gelpí, J. (2015). Molecular dynamics simulations: advances and applications. *Adv. Appl. Bioinform. Chem.*, 8, 37–47.

[63] Hsiang, Y. N., Crespo, M. T., Richter, A. M., Jain, A. K., Fragoso, M., & Levy, J. G. (1993). In vitro and in vivo uptake of benzoporphyrin derivative into human and miniswine atherosclerotic plaque. *Photochem. Photobiol.*, 57(4), 670–674.

[64] Hückel, E. (1931). Quantentheoretische Beiträge zum Benzolproblem. *Z. Phys*, 70(3), 204–286.

[65] Hückel, E. (1932). Quantentheoretische Beiträge zum Problem der aromatischen und ungesättigten Verbindungen. *Z. Phys*, 76(9), 628–648.

[66] Hüfner, S. (2003). *Photoelectron Spectroscopy*. Saarbrücken: Springer-Verlag, third edition.

[67] Hund, F. (1925). Atomtheoretische Deutung des Magnetismus der seltenen Erden. *Z. Phys*, 33(1), 855–859.

[68] Ito, E., Oji, H., Araki, T., Oichi, K., Ishii, H., Ouchi, Y., Ohta, T., Kosugi, N., Maruyama, Y., Naito, T., Inabe, T., & Seki, K. (1997). Soft X-ray absorption and X-ray photoelectron spectroscopic study of tautomerism in intramolecular hydrogen bonds of n-salicylideneaniline derivatives. *J. Am. Chem. Soc.*, 119(27), 6336–6344.

[69] Jirásek, M., Anderson, H. L., & Peeks, M. D. (2021a). From macrocycles to quantum rings: Does aromaticity have a size limit? *Acc. Chem. Res.*, 54(16), 3241–3251.

[70] Jirásek, M., Rickhaus, M., Tejerina, L., & Anderson, H. L. (2021b). Experimental and theoretical evidence for aromatic stabilization energy in large macrocycles. *J. Am. Chem. Soc.*, 143(5), 2403–2412.

[71] Johansson, M. P., Blomberg, M. R., Sundholm, D., & Wikström, M. (2002). Change in electron and spin density upon electron transfer to haem. *Biochim. Biophys. Acta*, 1553(3), 183 – 187.

[72] Judd, C. J., Nizovtsev, A. S., Plougmann, R., Kondratuk, D. V., Anderson, H. L., Besley, E., & Saywell, A. (2020). Molecular quantum rings formed from a π-conjugated macrocycle. *Phys. Rev. Lett.*, 125, 206803.

[73] Kaim, W., Schwederski, B., & Klein, A. (2013). *Bioinorganic Chemistry – Inorganic Elements in the Chemistry of Life: An Introduction and Guide*. Chichester: Wiley.

[74] Karelson, M. M., Katritzky, A. R., Szafran, M., & Zerner, M. C. (1989). Quantitative predictions of tautomeric equilibria for 2-, 3-, and 4-substituted pyridines in both the gas phase and aqueous solution: Combination of AM1 with reaction field theory. *J. Org. Chem.*, 54(26), 6030–6034.

[75] Kohn, W. & Sham, L. J. (1965). Self-consistent equations including exchange and correlation effects. *Phys. Rev.*, 140, A1133–A1138.

[76] Koopmans, T. (1934). Über die Zuordnung von Wellenfunktionen und Eigenwerten zu den Einzelnen Elektronen Eines Atoms. *Physica*, 1(1), 104–113.

[77] Kopp, S. M., Gotfredsen, H., Deng, J.-R., Claridge, T. D. W., & Anderson, H. L. (2020). Global aromaticity in a partially fused 8-porphyrin nanoring. *J. Am. Chem. Soc.*, 142(45), 19393–19401.

[78] Kotani, A. (2005). Resonant inelastic X-ray scattering in d and f electron systems. *Eur. Phys. J. B*, 47(1), 3–27.

[79] Kramers, H. A. & Heisenberg, W. K. (1925). Über die Streuung von Strahlung durch Atome. *Z. Phys.*, 31(1), 681–708.

[80] Kruszewski, J. & Krygowski, T. (1972). Definition of aromaticity basing on the harmonic oscillator model. *Tetrahedron Lett.*, 13(36), 3839–3842.

[81] Krygowski, T. M. (1993). Crystallographic studies of inter- and intramolecular interactions reflected in aromatic character of π-electron systems. *J. Chem. Inf. Comput. Sci.*, 33(1), 70–78.

[82] Kubin, M., Guo, M., Ekimova, M., Baker, M. L., Kroll, T., Källman, E., Kern, J., Yachandra, V. K., Yano, J., Nibbering, E. T. J., Lundberg, M., & Wernet, P. (2018a). Direct determination of absolute absorption cross sections at the L-edge of dilute Mn complexes in solution using a transmission flatjet. *Inorg. Chem.*, 57(9), 5449–5462.

[83] Kubin, M., Kern, J., Guo, M., Källman, E., Mitzner, R., Yachandra, V. K., Lundberg, M., Yano, J., & Wernet, P. (2018b). X-ray-induced sample damage at the Mn L-edge: a case study for soft X-ray spectroscopy of transition metal complexes in solution. *Phys. Chem. Chem. Phys.*, 20, 16817–16827.

[84] Kunnus, K., Rajkovic, I., Schreck, S., Quevedo, W., Eckert, S., Beye, M., Suljoti, E., Weniger, C., Kalus, C., Grübel, S., Scholz, M., Nordlund, D., Zhang, W., Hartsock, R. W., Gaffney, K. J., Schlotter, W. F., Turner, J. J., Kennedy, B., Hennies, F., Techert, S., Wernet, P., & Föhlisch, A. (2012). A setup for resonant inelastic soft x-ray scattering on liquids at free electron laser light sources. *Rev. Sci. Instrum.*, 83(12), 123109.

[85] Kunnus, K., Zhang, W., Delcey, M. G., Pinjari, R. V., Miedema, P. S., Schreck, S., Quevedo, W., Schröder, H., Föhlisch, A., Gaffney, K. J., Lundberg, M., Odelius, M., & Wernet, P. (2016). Viewing the valence electronic structure of ferric and ferrous hexacyanide in solution from the Fe and cyanide perspectives. *J. Phys. Chem. B*, 120(29), 7182–7194.

[86] Kutzelnigg, W. (2007). What I like about Hückel theory. *J. Comput. Chem.*, 28(1), 25–34.

[87] Kutzelnigg, W. & Morgan, J. D. (1996). Hund's rules. *Z. Phys. D: At., Mol. Clusters*, 36(3), 197–214.

[88] Kwiatkowski, J. & Pullman, B. (1975). Taulomerism and electronic structure of biological pyrimidines. In A. Katritzky & A. Boulton (Eds.), *Advances in Heterocyclic Chemistry*, volume 18 (pp. 199 – 335). Academic Press.

[89] Lambrechts, S. A. G., Aalders, M. C. G., & van Marle, J. (2005). Mechanistic study of the photodynamic inactivation of *candida albicans* by a cationic porphyrin. *Antimicrob. Agents Chemother.*, 49(5), 2026–2034.

[90] Lamola, A. A. & Yamane, T. (1974). Zinc protoporphyrin in the erythrocytes of patients with lead intoxication and iron deficiency anemia. *Science*, 186, 936 – 938.

[91] Lee, C., Yang, W., & Parr, R. G. (1988). Development of the colle-salvetti correlation-energy formula into a functional of the electron density. *Phys. Rev. B*, 37, 785–789.

[92] Li, D., Fedeles, B. I., Singh, V., Peng, C. S., Silvestre, K. J., Simi, A. K., Simpson, J. H., Tokmakoff, A., & Essigmann, J. M. (2014). Tautomerism provides a molecular explanation for the mutagenic properties of the anti-hiv nucleoside 5-aza-5,6-dihydro-2'-deoxycytidine. *Proc. Natl. Acad. Sci. U. S. A.*, 111(32), E3252–E3259.

[93] London, F. (1937). Théorie quantique des courants interatomiques dans les combinaisons aromatiques. *J. Phys. Radium*, 8(10), 397–409.

[94] Lonsdale, K. Y. & Bragg, W. H. (1937). Magnetic anisotropy and electronic structure of aromatic molecules. *Proc. R. Soc. London, Ser. A*, 159(896), 149–161.

[95] Loss, D. & Goldbart, P. (1991). Period and amplitude halving in mesoscopic rings with spin. *Phys. Rev. B*, 43, 13762–13765.

[96] Löwdin, P.-O. (1963). Proton tunneling in dna and its biological implications. *Rev. Mod. Phys.*, 35, 724–732.

[97] Manne, R. (1970). Molecular orbital interpretation of X-ray emission spectra: Simple hydrocarbons and carbon oxides. *J. Chem. Phys.*, 52(11), 5733–5739.

[98] March, A. M., Stickrath, A., Doumy, G., Kanter, E. P., Krässig, B., Southworth, S. H., Attenkofer, K., Kurtz, C. A., Chen, L. X., & Young, L. (2011). Development of high-repetition-rate laser pump/x-ray probe methodologies for synchrotron facilities. *Rev. Sci. Instrum.*, 82(7), 073110.

[99] Metzler, D. E. & Snell, E. E. (1955). Spectra and ionization constants of the vitamin B6 group and related 3-hydroxypyridine derivatives. *J. Am. Chem. Soc.*, 77(9), 2431–2437.

[100] Michelson, A. Z., Petronico, A., & Lee, J. K. (2012). 2-pyridone and derivatives: Gas-phase acidity, proton affinity, tautomer preference, and leaving group ability. *J. Org. Chem.*, 77(4), 1623–1631.

[101] Mobilio, S., Meneghini, C., & Boscherini, F., Eds. (2015). *Synchrotron Radiation: Basics, Methods and Applications*. Berlin Heidelberg: Springer.

[102] Mårtensson, N., Sokolowski, E., & Svensson, S. (2014). 50 years anniversary of the discovery of the core level chemical shifts. The early years of photoelectron spectroscopy. *J. Electron Spectrosc. Relat. Phenom.*, 193, 27–33.

[103] Nagasaka, M., Hatsui, T., Horigome, T., Hamamura, Y., & Kosugi, N. (2010). Development of a liquid flow cell to measure soft X-ray absorption in transmission mode: A test for liquid water. *J. Electron Spectrosc. Relat. Phenom.*, 177(2), 130–134.

[104] Nicolas, C. & Miron, C. (2012). Lifetime broadening of core-excited and -ionized states. *J. Electron Spectrosc. Relat. Phenom.*, 185(8), 267–272.

[105] Nordgren, J., Bray, G., Cramm, S., Nyholm, R., Rubensson, J. E., & Wassdahl, N. (1989). Soft x-ray emission spectroscopy using monochromatized synchrotron radiation. *Rev. Sci. Instrum.*, 60(7), 1690–1696.

[106] Norman, P. & Dreuw, A. (2018). Simulating X-ray spectroscopies and calculating core-excited states of molecules. *Chem. Rev.*, 118(15), 7208–7248.

[107] Oji, H., Mitsumoto, R., Ito, E., Ishii, H., Ouchi, Y., Seki, K., Yokoyama, T., Ohta, T., & Kosugi, N. (1998). Core hole effect in NEXAFS spectroscopy of polycyclic aromatic hydrocarbons: Benzene, chrysene, perylene, and coronene. *J. Chem. Phys.*, 109(23), 10409–10418.

[108] Okajima, T., Yamamoto, Y., Ouchi, Y., & Seki, K. (2001). NEXAFS spectra of metallotetraphenylporphyrins with adsorbed nitrogen monoxide. *J. Electron Spectrosc. Relat. Phenom.*, 114-116, 849–854.

[109] Olsen, S. (2015). Canonical-ensemble state-averaged complete active space self-consistent field (SA-CASSCF) strategy for problems with more diabatic than adiabatic states: Charge-bond resonance in monomethine cyanines. *J. Chem. Phys.*, 142(4), 044116.

[110] O'Regan, B. & Grätzel, M. (1991). A low-cost, high-efficiency solar cell based on dye-sensitized colloidal TiO_2 films. *Nature*, 353(6346), 737–740.

[111] Pauli, W. (1925). Über den Zusammenhang des Abschlusses der Elektronengruppen im Atom mit der Komplexstruktur der Spektren. *Z. Phys.*, 31(1), 765–783.

[112] Pauling, L. (1936). The diamagnetic anisotropy of aromatic molecules. *J. Chem. Phys.*, 4(10), 673–677.

[113] Penfold, T. J., Gindensperger, E., Daniel, C., & Marian, C. M. (2018). Spin-vibronic mechanism for intersystem crossing. *Chem. Rev.*, 118(15), 6975–7025.

[114] Perun, S., Tatchen, J., & Marian, C. M. (2008). Singlet and triplet excited states and intersystem crossing in free-base porphyrin: TDDFT and DFT/MRCI study. *ChemPhysChem*, 9(2), 282–292.

[115] Pullman, B. & Pullman, A. (1971). Electronic aspects of purine tautomerism. In A. Katritzky & A. Boulton (Eds.), *Advances in Heterocyclic Chemistry*, volume 13 (pp. 77 – 159). Academic Press.

[116] Reichardt, C. (2004). *Solvents and Solvent Effects in Organic Chemistry*, chapter 2, (pp. 5–56). John Wiley & Sons: Weinheim.

[117] Reid, I., Zhang, Y., Demasi, A., Blueser, A., Piper, L., Downes, J. E., Matsuura, A., Hughes, G., & Smith, K. E. (2009). Electronic structure of the organic semiconductor copper tetraphenylporphyrin (CuTPP). *Appl. Surf. Sci.*, 256(3), 720–725.

[118] Roos, B. O., Taylor, P. R., & Siegbahn, P. E. (1980). A complete active space SCF method (CASSCF) using a density matrix formulated super-CI approach. *Chem. Phys.*, 48(2), 157–173.

[119] Rowland, H. A. (1882). Preliminary notice of the results accomplished in the manufacture and theory of gratings for optical purposes. *Philosophical Magazine Series 5*, 13(84), 469–474.

[120] Rubensson, J.-E. (2000). RIXS dynamics for beginners. *J. Electron Spectrosc. Relat. Phenom.*, 110, 135–151.

[121] Ruedenberg, K. (1954). Free-electron network model for conjugated systems. V. Energies and electron distributions in the FE MO model and in the LCAO MO model. *J. Chem. Phys.*, 22(11), 1878–1894.

[122] Runge, E. & Gross, E. K. U. (1984). Density-functional theory for time-dependent systems. *Phys. Rev. Lett.*, 52, 997–1000.

[123] Ryan, A. A. & Senge, M. O. (2015). How green is green chemistry? Chlorophylls as a bioresource from biorefineries and their commercial potential in medicine and photovoltaics. *Photochem. Photobiol. Sci.*, 14, 638–660.

[124] Saes, M., van Mourik, F., Gawelda, W., Kaiser, M., Chergui, M., Bressler, C., Grolimund, D., Abela, R., Glover, T. E., Heimann, P. A., Schoenlein, R. W., Johnson, S. L., Lindenberg, A. M., & Falcone, R. W. (2004). A setup for ultrafast time-resolved x-ray absorption spectroscopy. *Rev. Sci. Instrum.*, 75(1), 24–30.

[125] Sakurai, J. J. & Napolitano, J. (2021). *Modern quantum mechanics*. Cambridge, United Kingdom: Cambridge University Press, third edition.

[126] Sasaki, S. (1994). Analyses for a planar variably-polarizing undulator. *Nucl. Instrum. Methods Phys. Res. A*, 347(1), 83–86.

[127] Schmidt, O. (1940a). Das Kastenmodell in Theorie und Praxis der aromatischen Verbindungen. *Ber. Dtsch. Chem. Ges.*, 73(8), A97–A116.

[128] Schmidt, O. (1940b). Die Berechnung der diamagnetischen Anisotropie der Aromaten aus der vom Kastenmodell gelieferten Dichteverteilung der B-Elektronen. *Z. Phys. Chem.*, 47B(1), 1–47.

[129] Schreck, S., Gavrila, G., Weniger, C., & Wernet, P. (2011). A sample holder for soft x-ray absorption spectroscopy of liquids in transmission mode. *Rev. Sci. Instrum.*, 82(10), 103101.

[130] Schreck, S., Pietzsch, A., Kennedy, B., Såthe, C., Miedema, P. S., Techert, S., Strocov, V. N., Schmitt, T., Hennies, F., Rubensson, J.-E., & Föhlisch, A. (2016). Ground state potential energy surfaces around selected atoms from resonant inelastic x-ray scattering. *Sci. Rep.*, 6(1), 20054.

[131] Schrödinger, E. (1926). Quantisierung als Eigenwertproblem (Erste Mitteilung). *Ann. Phys.*, 384(4), 361–376.

[132] Schrödinger, E. (1926). Quantisierung als Eigenwertproblem (Vierte Mitteilung). *Ann. Phys.*, 386(18), 109–139.

[133] Sette, F., Stöhr, J., & Hitchcock, A. P. (1984). Determination of intramolecular bond lengths in gas phase molecules from K shell shape resonances. *J. Chem. Phys.*, 81(11), 4906–4914.

[134] Silva, E. F. F., Serpa, C., Dąbrowski, J. M., Monteiro, C. J. P., Formosinho, S. J., Stochel, G., Urbanska, K., Simões, S., Pereira, M. M., & Arnaut, L. G. (2010). Mechanisms of singlet-oxygen and superoxide-ion generation by porphyrins and bacteriochlorins and their implications in photodynamic therapy. *Chem. Eur. J.*, 16(30), 9273–9286.

[135] Singh, V., Fedeles, B. I., & Essigmann, J. M. (2015). Role of tautomerism in RNA biochemistry. *RNA*, 21(1), 1–13.

[136] Slater, J. C. & Johnson, K. H. (1972). Self-consistent-field $X\alpha$ cluster method for polyatomic molecules and solids. *Phys. Rev. B*, 5, 844–853.

[137] Stanovnik, B., Tišler, M., Katritzky, A. R., & Denisko, O. V. (2006). The tautomerism of heterocycles: Substituent tautomerism of six-membered ring heterocycles. In A. R. Katritzky (Ed.), *Advances in Heterocyclic Chemistry*, volume 91 (pp. 1 – 134). New York: Academic Press.

[138] Stiel, H., Braenzel, J., Tuemmler, J., Jonas, A., Mantouvalou, I., Erko, A., Heilmann, A., Moerbeck-Bock, M., & Schnuerer, M. (2021). Ultrafast NEXAFS spectroscopy in the lab using laser-based sources and advanced X-ray optics. In D. Bleiner (Ed.), *International Conference on X-Ray Lasers 2020*, volume 11886 (pp. 290 – 297).: International Society for Optics and Photonics.

[139] Stöhr, J. (1992). *NEXAFS Spectroscopy*. Berlin Heidelberg: Springer.

[140] Sánchez-Ruiz, J. M., Llor, J., & Cortijo, M. (1984). Thermodynamic constants for tautomerism and ionization of pyridoxine and 3-hydroxypyridine in water–dioxane. *J. Chem. Soc., Perkin Trans.*, 2(12), 2047–2051.

[141] Tanaka, S. & Kotani, A. (1993). Resonant x-ray emission spectroscopy in La_2CuO_4 and CuO. *J. Phys. Soc. Jpn.*, 62(2), 464–467.

[142] Tang, M., Zhang, F., Zhao, Y., Wang, Y., Ke, Z., Li, R., Zeng, W., Han, B., & Liu, Z. (2021). A CO_2-mediated base catalysis approach for the hydration of triple bonds in ionic liquids. *Green Chem.*, 23, 9870–9875.

[143] Todd, D. (1994). Erythropoietic protoporphyria. *Br. J. Dermatol.*, 131(6), 751–766.

[144] Tolbert, L. M. & Zhao, X. (1997). Beyond the cyanine limit: peierls distortion and symmetry collapse in a polymethine dye. *J. Am. Chem. Soc.*, 119(14), 3253–3258.

[145] Triguero, L., Pettersson, L. G. M., & Ågren, H. (1998). Calculations of near-edge x-ray-absorption spectra of gas-phase and chemisorbed molecules by means of density-functional and transition-potential theory. *Phys. Rev. B*, 58, 8097–8110.

[146] Tsuda, A., Furuta, H., & Osuka, A. (2001). Syntheses, structural characterizations, and optical and electrochemical properties of directly fused diporphyrins. *J. Am. Chem. Soc.*, 123(42), 10304–10321.

[147] Uhlenbeck, G. E. & Goudsmit, S. (1925). Ersetzung der Hypothese vom unmechanischen Zwang durch eine Forderung bezüglich des inneren Verhaltens jedes einzelnen Elektrons. *Sci. Nat.*, 13(47), 953–954.

[148] Urbani, M., Grätzel, M., Nazeeruddin, M. K., & Torres, T. (2014). Meso-substituted porphyrins for dye-sensitized solar cells. *Chem. Rev.*, 114(24), 12330–12396.

[149] Valeur, B. (2001). *Molecular fluorescence : principles and applications*. New York: Wiley-VCH.

[150] Vaz da Cruz, V., Eckert, S., & Föhlisch, A. (2021). TD-DFT simulations of K-edge resonant inelastic X-ray scattering within the restricted subspace approximation. *Phys. Chem. Chem. Phys.*, 23, 1835–1848.

[151] Vaz da Cruz, V., Ignatova, N., Couto, R. C., Fedotov, D. A., Rehn, D. R., Savchenko, V., Norman, P., Ågren, H., Polyutov, S., Niskanen, J., Eckert, S., Jay, R. M., Fondell, M., Schmitt, T., Pietzsch, A., Föhlisch, A., Gel'mukhanov, F., Odelius, M., & Kimberg, V. (2019). Nuclear dynamics in resonant inelastic X-ray scattering and X-ray absorption of methanol. *J. Chem. Phys.*, 150(23), 234301.

[152] von Hofmann, A. W. (1857). On insolinic acid. *Proc. R. Soc. London*, 8, 1–3.

[153] Wachulak, P., Duda, M., Bartnik, A., Węgrzyński, L., Fok, T., & Fiedorowicz, H. (2019). NEXAFS at nitrogen K-edge and titanium L-edge using a laser-plasma soft x-ray source based on a double-stream gas puff target. *APL Photonics*, 4(3), 030807.

[154] Wannere, C. S. & von Ragué Schleyer, P. (2003). How aromatic are large $(4n + 2)\pi$ annulenes? *Org. Lett.*, 5(6), 865–868.

[155] Werner, H. & Meyer, W. (1981). A quadratically convergent MCSCF method for the simultaneous optimization of several states. *J. Chem. Phys.*, 74(10), 5794–5801.

[156] Willmott, P. (2011). *An introduction to synchrotron radiation: Techniques and applications*. Villigen: John Wiley and Sons.

[157] Wondrak, G. T., Roberts, M. J., Jacobson, M. K., & Jacobson, E. L. (2004). 3-Hydroxypyridine chromophores are endogenous sensitizers of photooxidative stress in human skin cells. *J. Biol. Chem.*, 279(29), 30009–30020.

[158] Xiang, D., Wang, X., Jia, C., Lee, T., & Guo, X. (2016). Molecular-scale electronics: From concept to function. *Chem. Rev.*, 116(7), 4318–4440.

[159] Yanai, T., Tew, D. P., & Handy, N. C. (2004). A new hybrid exchange–correlation functional using the coulomb-attenuating method (CAM-B3LYP). *Chem. Phys. Lett.*, 393(1), 51–57.

[160] Yoneda, T., Soya, T., Neya, S., & Osuka, A. (2016). [62]tetradecaphyrin and its mono- and bis-Zn^{II} complexes. *Chem. Eur. J.*, 22(41), 14518–14522.

Supporting information for publication I

Supporting Information: How Hydrogen Bonding Amplifies Isomeric Differences in Pyridones Towards Strong Changes in Acidity and Tautomerism

Robby Büchner,[*,†] Mattis Fondell,[‡] Eric J. Mascarenhas,[‡,†] Annette Pietzsch,[‡] Vinícius Vaz da Cruz,[*,‡] and Alexander Föhlisch[‡,†]

†*Institute of Physics and Astronomy, University of Potsdam, Karl-Liebknecht-Str. 24-25, 14476 Potsdam, Germany*

‡*Institute for Methods and Instrumentation for Synchrotron Radiation Research, Helmholtz-Zentrum Berlin für Materialien und Energie, Albert-Einstein-Str. 15, 12489 Berlin, Germany*

E-mail: robby.buechner@helmholtz-berlin.de; vinicius.vaz_da_cruz@helmholtz-berlin.de

Resonance structures of the Pyridone isomers

The resonance structures of the *ortho*, *meta*, and *para* Pyridone isomers are shown in Fig. S1.

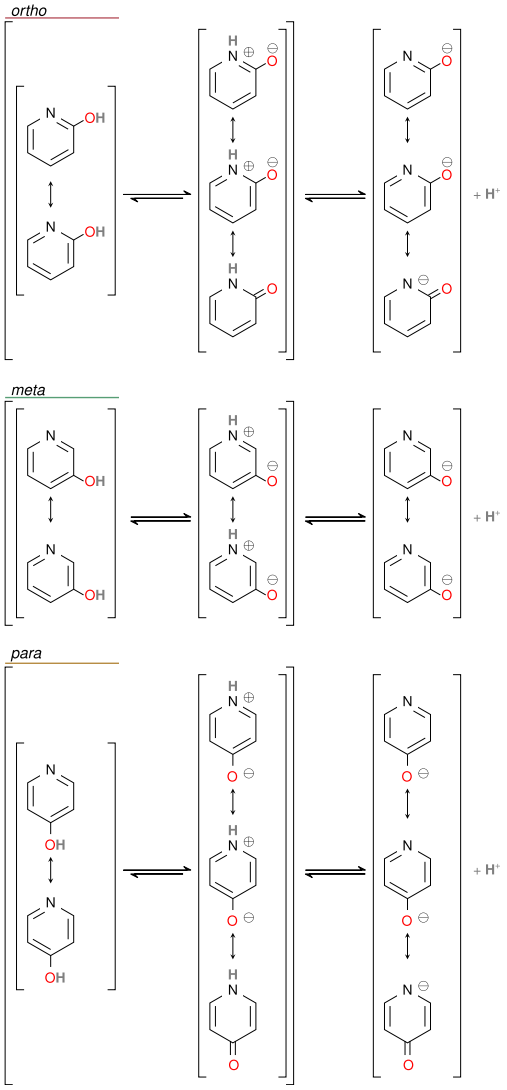

Figure S1: Resonance structures of the Hydroxypyridine (left) and Pyridone (middle) tautomers along with the fully deprotonated species (right).

Details of the Molecular Dynamics Simulations

The following procedure was carried out for all nine chemical species under study: Initially, a cubic box of 3.4 nm length comprising the chemical species of interest has been generated, then one Cl^- and K^+ counterion was added to the box for positively charged (PyH^+) and negatively charged molecules ($2PO^-$, $3PO^-$, $4PO^-$), respectively. The remaining space was filled with solvent molecules by using the *gmx_solvate* tool from the Gromacs package.[S1] All calculations used periodic boundary conditions. The temperature was controlled by a modified Berendsen thermostat (0.1 ps time constant) and in NPT runs the Parrinello-Rahman pressure-coupling (2 ps time constant) was used. For the calculation of the Coulomb and van der Waals term a cut-off of 1.4 nm was employed, while long-range electrostatics were treated via the particle mesh Ewald (PME) procedure. The energy of the initially generated system was minimized and subsequently the box was equilibrated in two steps: Firstly, an NVT equilibration at T = 298 K was run for 500 ps (Δt = 0.5 fs), followed by an NPT equilibration at T = 298 K and P = 1 bar, which was also run for 500 ps (Δt = 0.5 fs). The coordinates of the complex were constrained to the center of the box throughout the equilibration. Finally, a production NPT run of 10 ns (Δt = 0.5 fs, T = 298 K and P = 1 bar) was performed from which snapshots were collected every 1 ps. The final run was used for analysis of the radial distribution functions (see Fig. S2), hydrogen bonding properties (see below) and solvent mass-density plots (in the main article).

Force field and chelpg charges

The parameters for the intramolecular degrees of freedom as well as the Lennard-Jones non-bonded interactions were taken from the OPLS-aa[S2] force field by choosing the closest match to the molecules at hand. Since the charges used for the Coulomb interactions are not transferable as the other parameters, we chose to derive them for each molecule using the chelpg[S3] procedure, as implemented in the *orca_chelpg* utility program. The charges were

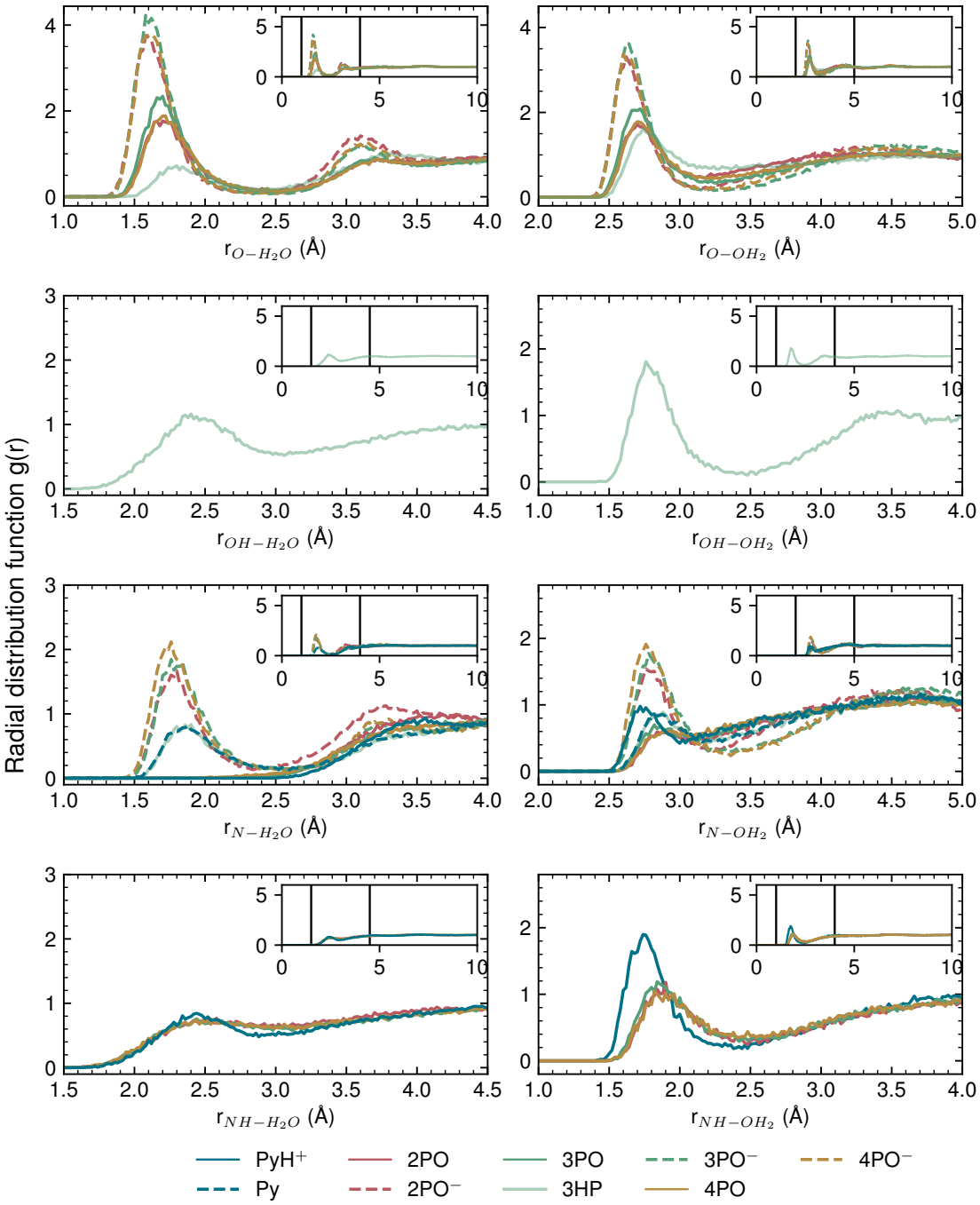

Figure S2: Radial distribution functions between oxygen (1st row), hydrogen (2nd, 4th row), or nitrogen (3rd row) of the sample and hydrogen (left) or oxygen (right) of water.

derived based on structures optimized at the RI-MP2 level of theory with the aug-cc-pVTZ basis set and the aug-cc-pVTZ/C auxiliary basis set. The calculations used CPCM.[S4] The full set of charges obtained is shown in Tab. S1.

Table S1: Chelpg charges used for the description of the electrostatic interactions in the MD simulations. For all molecules the nitrogen atom is labeled N1, then all carbon atoms are numbered clockwise. The numbering of the oxygen and hydrogen atoms is taken as the same number of the respective atom to which they are bonded.

PyH^+		Py		2PO		$2PO^-$			
label	q (e)	label	q (e)	label	q (e)	label	q (e)		
N1	-0.089	N1	-0.665	N1	-0.310	N1	-0.891		
H1	0.341	C2	0.482	H1	0.303	C2	1.173		
C2	-0.008	C3	-0.530	C2	0.646	C3	-0.750		
C3	-0.058	C4	0.272	C3	-0.333	C4	0.265		
C4	-0.016	C5	-0.530	C4	0.009	C5	-0.744		
C5	-0.059	C6	0.482	C5	-0.276	C6	0.466		
C6	-0.008	H2	0.020	C6	-0.046	H3	0.168		
H2	0.184	H3	0.191	H3	0.171	H4	0.029		
H3	0.179	H4	0.067	H4	0.123	H5	0.171		
H4	0.170	H5	0.191	H5	0.164	H6	-0.016		
H5	0.180	H6	0.020	H6	0.155	O2	-0.871		
H6	0.184			O2	-0.606				
3PO		$3PO^-$		3HP		4PO		$4PO^-$	
label	q (e)	label	q (e)	label	q (e)	label	q (e)	label	q (e)
N1	-0.059	N1	-0.729	N1	-0.636	N1	-0.257	N1	-0.847
H1	0.304	C2	0.283	C2	0.343	H1	0.311	C2	0.494
C2	-0.259	C3	0.252	C3	0.071	C2	-0.019	C3	-0.837
C3	0.606	C4	0.009	C4	-0.005	C3	-0.378	C4	1.050
C4	-0.292	C5	-0.573	C5	-0.441	C4	0.701	C5	-0.837
C5	-0.063	C6	0.312	C6	0.377	C5	-0.367	C6	0.492
C6	-0.229	H2	-0.005	H2	0.077	C6	-0.027	H2	-0.020
H2	0.163	H4	0.060	H4	0.115	H2	0.145	H3	0.187
H4	0.160	H5	0.158	H5	0.189	H3	0.177	H5	0.187
H5	0.142	H6	-0.007	H6	0.044	H5	0.173	H6	-0.019
H6	0.165	O3	-0.760	O3	-0.548	H6	0.148	O4	-0.850
O3	-0.638			H3	0.414	O4	-0.607		

Hydrogen bonding properties

The analysis of the hydrogen bonding properties was carried out by examining the radial distribution functions, obtained with the *gmx_rdf* tool, as well as analysing hydrogen bond (HB) statistics with the *gmx_hbond* tool included in the Gromacs package. The full set of HB parameters is shown in Tab. S2

Table S2: Hydrogen bonding parameters extracted from the MD simulations in aqueous solution. The r_{NH} distance is obtained from the maximum of the $g_{XH}(r)$ and $g_{HO}(r)$ pair-correlation functions. The number of HBs (n_{HB}) is defined via the X=N,O and the water OH bond for $\angle XHO < 20°$ and $r_{X-O} <$ 3.5 Å.

Molecule	r_{N-H}	r_{N-O} (Å)	$\angle NOH$ (°)	n_{HB}
Py	1.87	2.92 ± 0.18	11.16 ± 4.91	0.90 ± 0.60
$2PO^-$	1.79	2.86 ± 0.17	10.01 ± 4.78	1.58 ± 0.58
$3PO^-$	1.80	2.88 ± 0.18	10.16 ± 4.83	1.92 ± 0.63
$4PO^-$	1.77	2.86 ± 0.18	9.71 ± 4.74	2.09 ± 0.61
3HP	1.88	2.93 ± 0.18	11.22 ± 4.88	0.87 ± 0.61
Molecule	r_{NH-O}	r_{N-O} (Å)	$\angle NHO$ (°)	n_{HB}
PyH^+	1.76	2.78 ± 0.13	10.86 ± 4.89	0.72 ± 0.45
2PO	1.90	2.95 ± 0.19	11.48 ± 4.91	0.60 ± 0.50
3PO	1.88	2.91 ± 0.19	11.61 ± 4.87	0.60 ± 0.51
4PO	1.90	2.95 ± 0.20	11.69 ± 4.88	0.58 ± 0.53
Molecule	r_{CO-H}	r_{CO-O} (Å)	$\angle OOH$ (°)	n_{HB}
2PO	1.72	2.78 ± 0.17	10.50 ± 4.84	1.59 ± 0.66
3PO	1.71	2.77 ± 0.17	10.24 ± 4.82	1.96 ± 0.68
4PO	1.72	2.79 ± 0.17	10.57 ± 4.91	1.66 ± 0.69
$2PO^-$	1.58	2.70 ± 0.16	9.00 ± 4.59	2.76 ± 0.54
$3PO^-$	1.58	2.71 ± 0.16	8.92 ± 4.55	3.11 ± 0.56
$4PO^-$	1.62	2.70 ± 0.16	9.00 ± 4.60	2.87 ± 0.55
3HP	1.80	2.88 ± 0.19	11.35 ± 4.89	0.72 ± 0.58
Molecule	r_{OH-O}	r_{CO-O} (Å)	$\angle OHO$ (°)	n_{HB}
3HP	1.80	2.83 ± 0.18	10.88 ± 4.87	1.52 ± 0.71

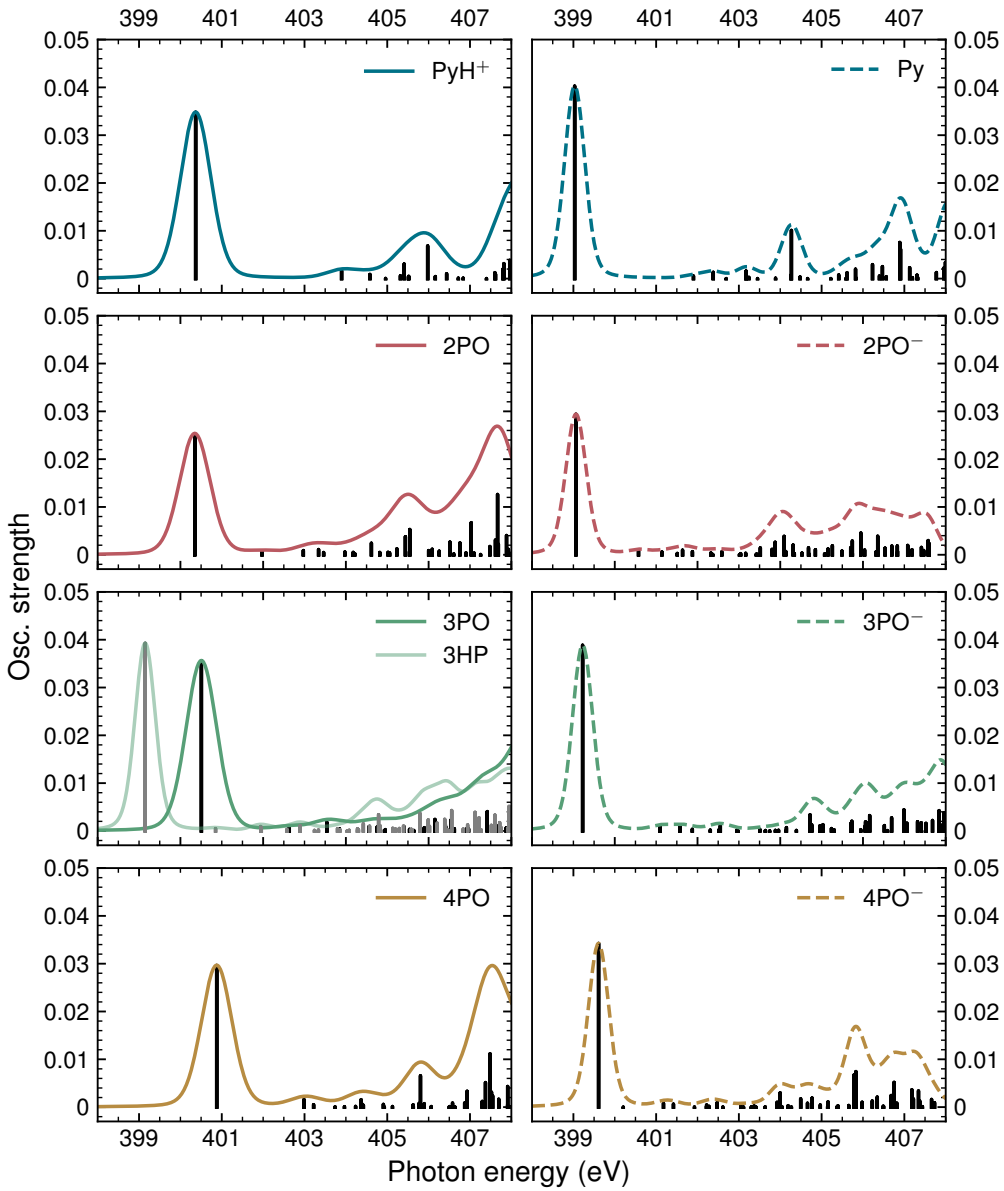

Figure S3: X-ray absorption at the N K-edge as calculated by the TD-DFT method. The energy axis is shifted by 11.135 eV to ease the comparison with the experimental spectra in the main article. Transition moments are shown as black bars. For the plotted spectra a lifetime broadening of 0.13 eV[S5] and an experimental broadening of 0.51 eV (deprotonated nitrogen) or 0.80 eV (protonated nitrogen) have been used.

TD-DFT

As described in the computational details section of the main article, TD-DFT calculations were performed on the optimized geometries with the minimally-solvated models resulting from the MD simulation. The TD-DFT calculations were carried out with PBE0 hybrid functionals[S6] utilizing the def2-QZVPPD[S7,S8] basis and def2/J[S9] auxiliary basis set with the RIJCOSX[S10] approximation. CPCM[S4] was used to account for bulk-liquid effects. For numerical integration the ORCA[S11] Grid7 (and GridX9 as COSX grid) were used.

N K-edge absorption spectra (see Fig. S3) were obtained by applying a Voigt function to every transition moment. The Gaussian broadening results from a global fit of the experimental π^* resonance of all molecules with the same nitrogen protonation state and a fixed Lorentzian FWHM of 0.13 eV.[S5] Additionally the spectra were shifted according to the difference of the TD-DFT and experimental π^* resonance of Py.

References

(S1) Lindahl,; Abraham,; Hess,; van der Spoel, GROMACS 2019 source code. `https://doi.org/10.5281/zenodo.2424363`.

(S2) Jorgensen, W. L.; Maxwell, D. S.; Tirado-Rives, J. Development and testing of the OPLS all-atom force field on conformational energetics and properties of organic liquids. *J. Am. Chem. Soc.* **1996**, *118*, 11225–11236.

(S3) Breneman, C. M.; Wiberg, K. B. Determining atom-centered monopoles from molecular electrostatic potentials. The need for high sampling density in formamide conformational analysis. *J. Comput. Chem.* **1990**, *11*, 361–373.

(S4) Barone, V.; Cossi, M. Quantum calculation of molecular energies and energy gradients in solution by a conductor solvent model. *J. Phys. Chem. A* **1998**, *102*, 1995–2001.

(S5) Nicolas, C.; Miron, C. Lifetime broadening of core-excited and -ionized states. *J. Electron Spectrosc. Relat. Phenom.* **2012**, *185*, 267 – 272.

(S6) Adamo, C.; Barone, V. Toward reliable density functional methods without adjustable parameters: The PBE0 model. *J. Chem. Phys.* **1999**, *110*, 6158–6170.

(S7) Weigend, F.; Ahlrichs, R. Balanced basis sets of split valence, triple zeta valence and quadruple zeta valence quality for H to Rn: Design and assessment of accuracy. *Phys. Chem. Chem. Phys.* **2005**, *7*, 3297–3305.

(S8) Rappoport, D.; Furche, F. Property-optimized Gaussian basis sets for molecular response calculations. *J. Chem. Phys.* **2010**, *133*, 134105.

(S9) Weigend, F. Accurate Coulomb-fitting basis sets for H to Rn. *Phys. Chem. Chem. Phys.* **2006**, *8*, 1057–1065.

(S10) Neese, F.; Wennmohs, F.; Hansen, A.; Becker, U. Efficient, approximate and parallel Hartree-Fock and hybrid DFT calculations. A chain-of-spheres-algorithm for the Hartree-Fock exchange. *Chem. Phys.* **2009**, *356*, 98 – 109.

(S11) Neese, F. The ORCA program system. *Wiley Interdiscip. Rev.: Comput. Mol. Sci.* **2012**, *2*, 73–78.

Supporting Information for: Targeting Individual Tautomers in Equilibrium by Resonant Inelastic X-ray Scattering

Vinícius Vaz da Cruz,*,† Robby Büchner,† Mattis Fondell,† Annette Pietzsch,† Sebastian Eckert,† and Alexander Föhlisch†

†*Helmholtz-Zentrum Berlin für Materialien und Energie GmbH, Institute for Methods and Instrumentation for Synchrotron Radiation Research, 12489 Berlin, Germany.*

‡*Universität Potsdam, Institut für Physik und Astronomie, 14476 Potsdam, Germany.*

E-mail: vinicius.vaz_da_cruz@helmholtz-berlin.de

Resonant Inelastic X-ray Scattering Theory

Let us briefly recap the basic theory of resonant inelastic X-ray scattering (RIXS). Neglecting pre-factors, the RIXS cross-section is written[1]

$$\sigma(\omega', \omega) = \sum_f |F_f|^2 \Delta(\omega - \omega' - \omega_{f0}, \Gamma_f), \tag{1}$$

where ω and ω' are the incoming and outgoing photon frequencies, respectively. $\omega_{f0} = (\epsilon_f - \epsilon_0)/\hbar$ is the transition frequency difference between the initial state and final state. And where $\Delta(\Omega, \Gamma) = \Gamma/\pi(\Omega^2 + \Gamma^2)$ is a Lorentzian function with HWHM Γ. And the Scattering amplitude of a given final state is given by the Kramers-Heisenberg equation

$$F_f = \sum_i \omega_{if}\omega_{i0} \frac{\langle f|\mathbf{e}' \cdot \mathbf{r}|i\rangle\langle i|\mathbf{e} \cdot \mathbf{r}|0\rangle}{\omega - \omega_{i0} + i\Gamma}. \tag{2}$$

To obtain the final working equations, let us introduce the tensor component of the cross-section in terms of the electronic transition dipole moments as follows

$$\sigma^{(f)}_{\alpha\beta\gamma\delta} = F_f^{\beta\delta\,\dagger} F_f^{\alpha\gamma}, \quad F_f^{\alpha\gamma} = \sum_i \frac{\mu^{\alpha}_{fi}\mu^{\gamma}_{i0}}{\omega - \omega_{i0} + \imath\Gamma} \tag{3}$$

Here $\alpha, \beta, \gamma, \delta \in \{x, y, z\}$. Then, after averaging over orientations,[2] the total cross-section reads

$$\begin{aligned}\overline{\sigma(\omega', \omega, \chi)} = \quad & \frac{1}{30}\sum_f \sum_{\alpha,\beta} [(3 + \cos^2\chi)\sigma^{(f)}_{\alpha\alpha\beta\beta} + \frac{1}{2}(1 - 3\cos^2\chi)(\sigma^{(f)}_{\alpha\beta\alpha\beta} + \sigma^{(f)}_{\alpha\beta\beta\alpha})] \\ & \times \Delta(\omega' + \omega_{f0} - \omega, \Gamma_f),\end{aligned} \tag{4}$$

all of our RIXS simulations are based on this equation. The final RIXS cross-section therefore is a function of the photon energies and the angle χ between the incoming photon polarization and the wave vector of the emitted photon defined as $\cos\chi = \mathbf{e} \cdot \mathbf{k}'$. In the main text the standard convention is used for vertical polarization ($\chi = 90°$) and horizontal

polarization ($\chi = 0°$).

Electronic Structure Calculations

Geometry optimizations were carried out at the B3LYP/PBE0 level with the def2-TZVP(-f)[3] basis set, using the D3BJ[4,5] correction. The RIJCOSX approximation[6] was used with the def2/J[7] auxiliary basis. For simulations in solution, the conductor-like polarizable continuum model[8] (CPCM) was used using the Gaussian charge scheme[9] with a scaled Van der Waals cavity with radii from Bondi.[10] All electronic structure calculations used the ORCA package.[11]

RIXS calculations based on the optimized geometries As mentioned in the main text, the electronic RIXS scattering amplitudes are computed within the RSA-TD-DFT method described in detail within ref.[12] The linear response equations were solved considering restricted subspaces defined as (N_c,N_o,N_u) $\equiv$ (1,18,20), where N_c is the number of core orbitals considered (in this case only the N 1s orbital), N_o is the number of occupied orbitals considered and N_u is the number of unoccupied orbitals included. A total of 365 roots were computed, for each tautomer, comprising the manifold of valence excited state and the 5 lowest core-excited states. The transition dipole moments were computed using Multifwn,[13] based on the ORCA output. For the final calculations in the main text, the PBE functional was selected, as better intensity ratios were obtained with this functional (see below). The def2-TZVP(-f)[3] basis set was adopted.

Functional dependence No strong functional dependency was found for RIXS calculations considering pure PBE and BLYP and hybrid PBE0 and B3LYP exchange and correlation functionals. However, considering both tautomers, we deemed the results to be slightly better in terms of intensity ratios and transition energies in the RIXS spectra for the calculations employing the PBE functional. The comparison of the RIXS spectra obtained with

different functionals is shown in Fig. 1.

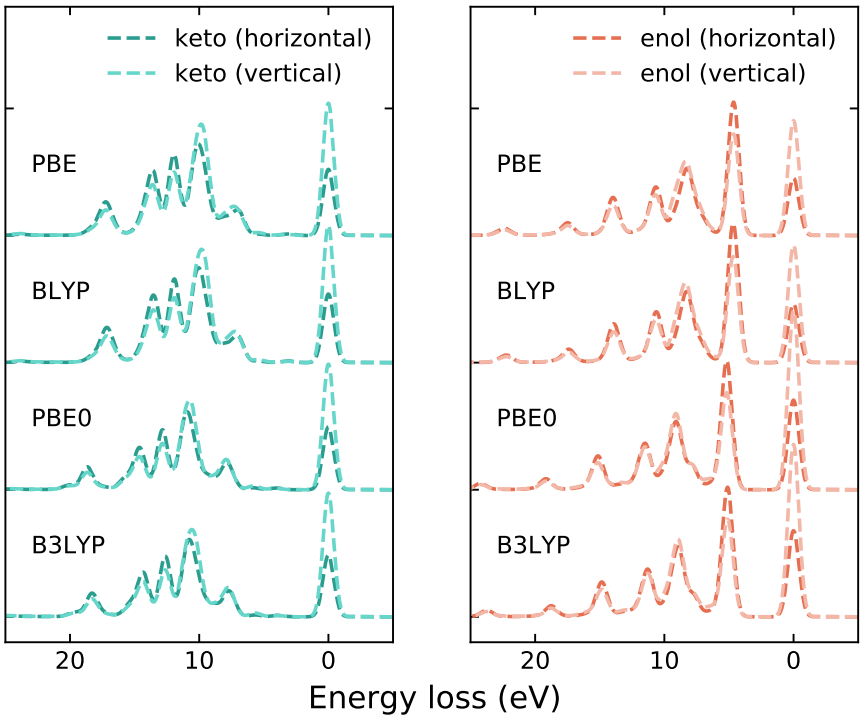

Figure 1: Analysis of functional dependence of the RIXS simulations.

QM/MM Molecular Dynamics Simulations

Details of the simulations

The Quantum Mechanics/Molecular Mechanics (QM/MM) Molecular Dynamics (MD) simulations were carried out using NAMD[14] interfaced with ORCA,[11] as mentioned in the main text. The quantum region consisted only of the solute molecule, while the solvent was modelled classically. The interaction between classical and quantum region was modelled using Chelpg[15] charges derived from the QM region combined with classical intermolecular pa-

rameters taken from the CHARM[16] force field. The simulations were set up with the aid of the QwikMD module.[17] First, each of the tautomers was placed in a cubic box of length 3.6 nm filled with water molecules. Then the energy of the system was minimized, followed by a temperature annealing phase where the temperature was gradually raised from 60 K to 300 K, over a 7.5 ps interval, during which the pressure was kept constant at 1 bar. After that, the annealed system was further equilibrated for 0.25 ps at 300 K and 1 bar. Lastly, the equilibrated system was propagated for 40 ps in a final NPT (T = 300K, P= 1 bar) production run. From this trajectory snapshots were taken for computing the radial distribution functions, hydrogen bond analysis as well as for the sampled RIXS spectra calculations.

Micro-solvation structure and hydrogen bonding

From the QM/MM simulations we can characterize the microsolvation structure of each tautomer in aqueous solution, as discussed in the main text. In Fig. 2 the radial distribution function between the solute and the water molecules of the solvent are shown at the N, H and O atoms of each tautomer.

From the radial distribution functions, we calculated the coordination number around the hydrogen bonding sites, as well as the average number of hydrogen bonds considering the criteria $r_{X-H} < 3.0$ Å and $\angle XHO < 20°$. These results are compiled in Tab. 1

Table 1: Hydrogen bond analysis from the MD simulation for each 3HP tautomer in aqueous solution. The average number of HBs (n_{HB}) between water and the soluted is defined via the criteria $\angle XHO < 20°$ and $r_{N-O} <$ 3.0 Å.

keto			enol		
moiety	n_c	n_{HB}	moiety	n_c	n_{HB}
N-H (donor)	1.0	0.6 ± 0.5	N: (acceptor)	1.2	0.6 ± 0.5
C=O (acceptor)	3.8	2.2 ± 1.0	O-H (donor)	1.0	0.8 ± 0.4
			O-H (acceptor)	0.9	0.3 ± 0.5

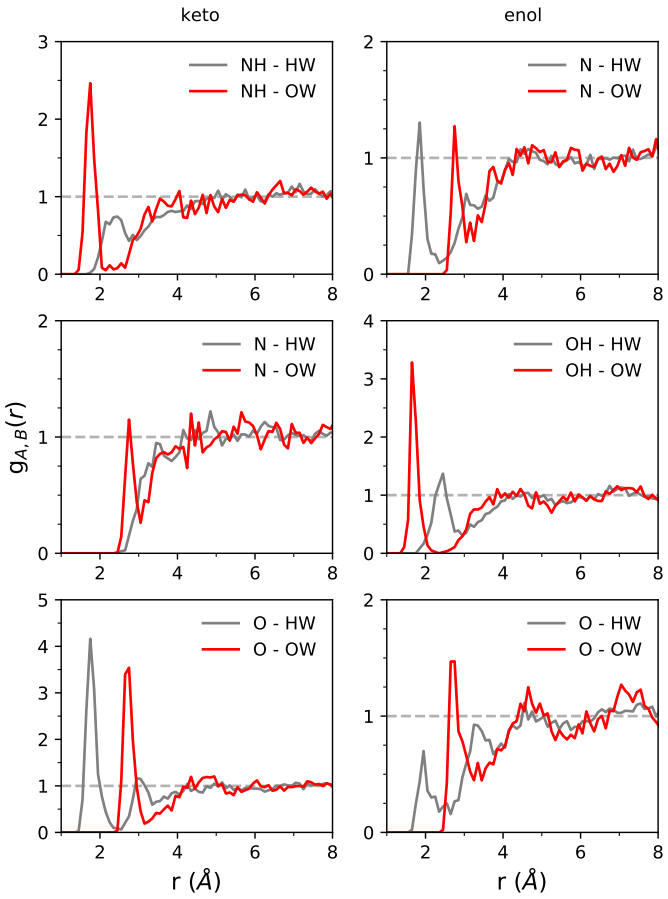

Figure 2: Radial distribution functions computed from 400 snapshots from a 40 ps QM/MM MD simulation of the keto form and enol form in aqueous solution.

RIXS simulations including explicit solvation

The effects of the hydrogen bonding interactions, with each tautomer, and thermal geometrical distortions was evaluated by computing an averaged RIXS spectrum sampled from snapshots of the QM/MM MD. From the snapshots, minimally solvated snapshot were constructed including the solute (either the keto, or the enol form of 3HP) and the first solvation shell at the both the nitrogen, hydrogen and oxygen atoms. The cut-off distance for selecting

the explicitly solvating water molecules was chosen as the first minimum in the respective radial distribution function for the given atom (See Fig. 2). The remaining bulk solvation effects were accounted for by a CPCM layer around the minimally solvated cluster. The same level of theory from the calculations based on the optimized geometries was adopted. A similar orbital truncation was used, except the subspaces were defined as (1,N_o,20) in which $N_o = 18 + 4 \times n_{H_2O}$, since each explicit water molecule adds 4 orbitals to the occupied subspace in the calculation (ignoring the O 1s core orbitals).

Sources of broadening in the X-ray absorption step

In order to correctly simulate the averaged RIXS spectrum in solution, it is necessary to ensure a correct description of the broadening of the X-ray absorption step. This is because of the coupled nature of the excitation and emission step and the dependence on the incoming photon energy. Therefore, the weight of the contribution from each sampled configuration will be affected by the broadening of the absorption line of each snapshot. The most basic broadening mechanism is the inherent core-hole lifetime, which for nitrogen is $\Gamma = 0.06$ eV[18](HWHM), this is accounted in Eq. 2. On top of that, we have the inhomogeneous broadening due to solvation. This is accounted for in the calculations by the sampling of configurations from the QM/MM MD simulation. Another important broadening mechanism is the vibrational (Franck-Condon) broadening, which is large at soft X-ray K edges. Lastly, we have to consider for the finite incomning photon bandwidth of the X-ray source $\Delta\omega = 0.19$ eV for the RIXS measurements and 0.11 eV for the XAS measurements.

In Fig. 3 we show calculations for the aforementioned broadening mechanism compared with the experimental XAS. From these calculations we can estimate that the vibrational broadening is very large, and is the main broadening mechanism determining the lineshape. For the enol form FWHM(vibrational) = 0.96 eV, while FWHM(solvation) = 0.21, while for the keto form FWHM(vibrational) = 1.10 eV, while FWHM(solvation) = 0.31 eV.

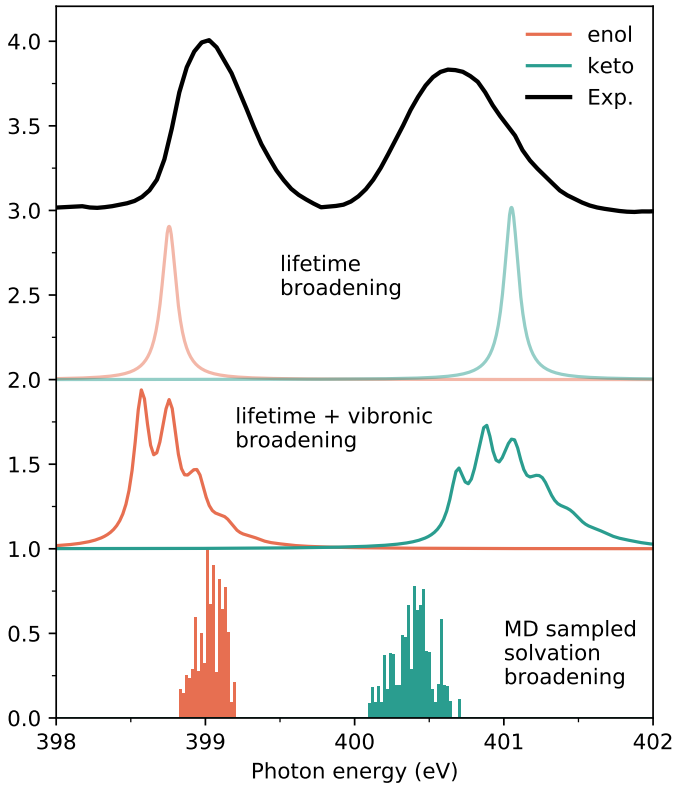

Figure 3: Constributions to the X-ray absorption absorption lineshape. The top row shows the experimental X-ray absorption spectrum(XAS) of the tautomeric mixture. The second row shows the calculated XAS (gas-phase) considering only the core-hole lifetime broadening. The third row shows the calculated XAS including the core-hole lifetime and the Franck-Condon vibrational lineshape. The fourth row shows the inhomogeneous broadening induced by the solvent, histograms based on the transition energies and transition dipole moments sampled from the QM/MM MD.

Franck-Condon calculations

The vibronic profiles discussed in the previous section were computed using the linear coupling model, based on core-excited gradients computed using the Z+1 approximation. Calculations included all normal modes for each system and were carried out in gas-phase. The potentials were assumed to be harmonic along each normal mode, and the core-excited po-

tential was assumed to have the same shape as the ground state, except shifted. The shift was determined from the computed gradient. Calculations were done using in-house programmed python routines. The gradients and frequencies were computed with ORCA, at the same level of used for the remaining calculations.

Convolution of the calculated RIXS spectra in solution

The simulated RIXS map for each tautomer sampled from the MD simulations inherently accounts for the solvation broadening as well as for the core-hole lifetime broadening, hence the missing vibrational broadening was added phenomenologically by convolution with a Gaussian function along the excitation energy axis, using the values from the previous section. The broadening due to the incoming photon bandwidth of 0.19 eV was also added. On the emission energy axis, we are limited by the resolution of the spectrometer. In this case, and effective Gaussian broadening of 0.9 eV was added for best comparison with the experimental data.

Extraction of the tautomerization constant K_T

The tautomerization constant has been reported to be 1.17 by Metzler and Snell[19] and 1.10 by Sanchez-Ruiz et al.[20] Later, Llor and Aresenio[21] reported the temperature dependence of the equilibrium constant. Using a Van 't Hoff analysis, they reported a standard enthalpy of 2.39 kcal/mol for the process. This is important for our measurements, because they are performed in liquid jets under vaccum, which are subject to evaporative cooling. The jet is initially at room temperature. The expected temperature drop is on the order of 5-10°C from 25°C. In Fig. 4, we derived K_T based on the X-ray absorption spectrum, assuming the lineshapes descibed in the previous section. The value obtained $K_T = 1.08 \pm 0.02$ is in good agreement with the values reported by Llor and Arsenio for the temperature range of 20-10°C, confirming the expectation that the constant is not strongly affected by the vaccum environment.

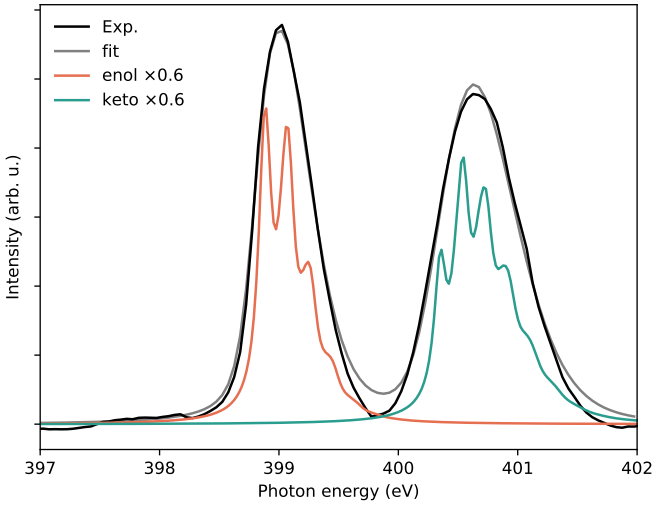

Figure 4: Extraction of the tautomerization constant from the experimental XAS. The computed vibronic lineshapes are convoluted with the estimated solvation broadening and incoming photon energy bandwidth and subsequently the amplitueds and shifts are fitted to the experimental XAS, yielding a tautomerization constant $K_T = 1.08 \pm 0.02$.

Resonance structures of 3HP

For completeness, we display the possible resonance structures of 3-hydroxypyridine in Fig. 5. It should be mentioned that unlike the 2HP and 4HP isomers, there is no reasonable neutral Lewis structure for the keto tautomer. Fig. 5 excludes possible zwitterionic structures with formal charges on the carbon atoms, as they are chemically unfavourable. Possible biradical structures are also ignored.

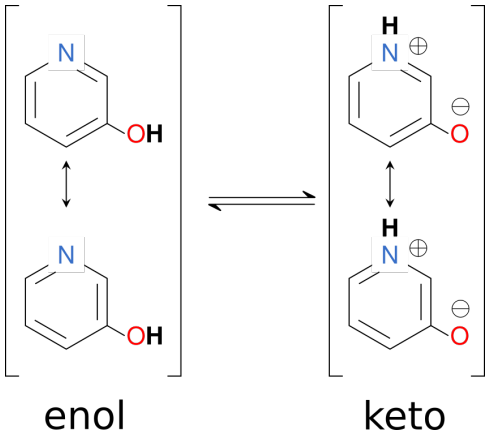

Figure 5: Resonance structures of the enol and keto tautomers of 3-hydroxypyridine (3HP).

References

(1) Gel'mukhanov, F.; Odelius, M.; Polyutov, S. P.; Föhlisch, A.; Kimberg, V. Dynamics of resonant x-ray and Auger scattering. *Rev. Mod. Phys.* **2021**, *93*, 035001.

(2) Gel'mukhanov, F.; Ågren, H. Resonant Inelastic X-Ray Scattering With Symmetry-Selective Excitation. *Phys. Rev. A* **1994**, *49*, 4378–4389.

(3) Weigend, F.; Ahlrichs, R. Balanced Basis Sets of Split Valence, Triple Zeta Valence and Quadruple Zeta Valence Quality for H to Rn: Design and Assessment of Accuracy. *Phys. Chem. Chem. Phys.* **2005**, *7*, 3297–3305.

(4) Grimme, S.; Antony, J.; Ehrlich, S.; Krieg, H. A Consistent and Accurate Ab Initio Parametrization of Density Functional Dispersion Correction (DFT-D) for the 94 Elements H-Pu. *J. Chem. Phys.* **2010**, *132*, 154104.

(5) Grimme, S.; Ehrlich, S.; Goerigk, L. Effect of the Damping Function in Dispersion Corrected Density Functional Theory. *J. Comput. Chem.* **2011**, *32*, 1456–1465.

(6) Neese, F.; Wennmohs, F.; Hansen, A.; Becker, U. Efficient, Approximate and Parallel Hartree-Fock and Hybrid DFT Calculations. A Chain-of-Spheres-Algorithm for the Hartree-Fock Exchange. *Chem. Phys.* **2009**, *356*, 98 – 109.

(7) Weigend, F. Accurate Coulomb-Fitting Basis Sets for H to Rn. *Phys. Chem. Chem. Phys.* **2006**, *8*, 1057–1065.

(8) Barone, V.; Cossi, M. Quantum Calculation of Molecular Energies and Energy Gradients in Solution by a Conductor Solvent Model. *J. Phys. Chem. A* **1998**, *102*, 1995–2001.

(9) Lange, A. W.; Herbert, J. M. A Smooth, Nonsingular, and Faithful Discretization Scheme for Polarizable Continuum Models: The Switching/Gaussian Approach. *J. Chem. Phys.* **2010**, *133*, 244111.

(10) Bondi, A. v. Van der Waals Volumes and Radii. *J. Phys. Chem.* **1964**, *68*, 441–451.

(11) Neese, F. The ORCA Program System. *Wiley Interdiscip. Rev. Comput. Mol. Sci.* **2012**, *2*, 73–78.

(12) Vaz da Cruz, V.; Eckert, S.; Föhlisch, A. TD-DFT Simulations of K-edge Resonant Inelastic X-ray Scattering Within the Restricted Subspace Approximation. *Phys. Chem. Chem. Phys.* **2021**, *23*, 1835–1848.

(13) Lu, T.; Chen, F. Multiwfn: A Multifunctional Wavefunction Analyzer. *J. Comput. Chem.* **2012**, *33*, 580–592.

(14) Melo, M. C.; Bernardi, R. C.; Rudack, T.; Scheurer, M.; Riplinger, C.; Phillips, J. C.; Maia, J. D.; Rocha, G. B.; Ribeiro, J. V.; Stone, J. E. et al. NAMD Goes Quantum: An Integrative Suite for Hybrid Simulations. *Nat. Methods* **2018**, *15*, 351–354.

(15) Breneman, C. M.; Wiberg, K. B. Determining Atom-Centered Monopoles from Molecular Electrostatic Potentials. The Need for High Sampling Density in Formamide Conformational Analysis. *J. Comput. Chem.* **1990**, *11*, 361–373.

(16) Yu, W.; He, X.; Vanommeslaeghe, K.; MacKerell Jr., A. D. Extension of the CHARMM

General Force Field to Sulfonyl-Containing Compounds and its Utility in Biomolecular Simulations. *J. Comput. Chem.* **2012**, *33*, 2451–2468.

(17) Ribeiro, J. V.; Bernardi, R. C.; Rudack, T.; Stone, J. E.; Phillips, J. C.; Freddolino, P. L.; Schulten, K. QwikMD — Integrative Molecular Dynamics Toolkit for Novices and Experts. *Sci. Rep.* **2016**, *6*, 1–14.

(18) Nicolas, C.; Miron, C. Lifetime Broadening of Core-Excited and -Ionized States. *J. Electron Spectrosc. Relat. Phenom.* **2012**, *185*, 267 – 272.

(19) Metzler, D. E.; Snell, E. E. Spectra and Ionization Constants of the Vitamin B6 Group and Related 3-Hydroxypyridine Derivatives. *J. Am. Chem. Soc.* **1955**, *77*, 2431–2437.

(20) Sánchez-Ruiz, J. M.; Llor, J.; Cortijo, M. Thermodynamic constants for tautomerism and ionization of pyridoxine and 3-Hydroxypyridine in water–dioxane. *J. Chem. Soc., Perkin Trans. 2* **1984**, 2047–2051.

(21) Llor, J.; Asensio, S. B. Thermodynamics of the Solution Equilibria of 3-Hydroxypyridine and Pyridoxine in Water-Dioxane Mixtures. *J. Sol. Chem.* **1995**, *24*, 1293–1305.

Electronic Supplementary Material (ESI) for Physical Chemistry Chemical Physics.

Supplementary Information

The Porphyrin Center as a Regulator for Metal-Ligand Covalency and π Hybridization in the Entire Molecule

Robby Büchner,*[a] Mattis Fondell,[b] Robert Haverkamp,[b] Annette Pietzsch,[b] Vinícius Vaz da Cruz,*[b] and Alexander Föhlisch[a,b]

[a] *Institute of Physics and Astronomy, University of Potsdam, Karl-Liebknecht-Str. 24-25, 14476 Potsdam, Germany. Tel: +49 30 806213967; E-mail: rbuechner@uni-potsdam.de,*
[b] *Institute for Methods and Instrumentation for Synchrotron Radiation Research, Helmholtz-Zentrum Berlin für Materialien und Energie, Albert-Einstein-Str. 15, 12489 Berlin, Germany. Tel: +49 30 806214987; E-mail: vinicius.vaz_da_cruz@helmholtz-berlin.de*

UV/VIS spectra

The UV/VIS spectra of all investigated carboxylated tetraphenylporphyrins – more specifically 5,10,15,20-tetrakis(4-carboxyphenyl)porp
(TCPPs) – are plotted in Figure S1. They show the characteristic strong Soret (410-430 eV) and weaker Q bands (510-640 eV) common
to all porphyrins. The rather narrow lineshape of the former evidences the prevalence of monomers [1].

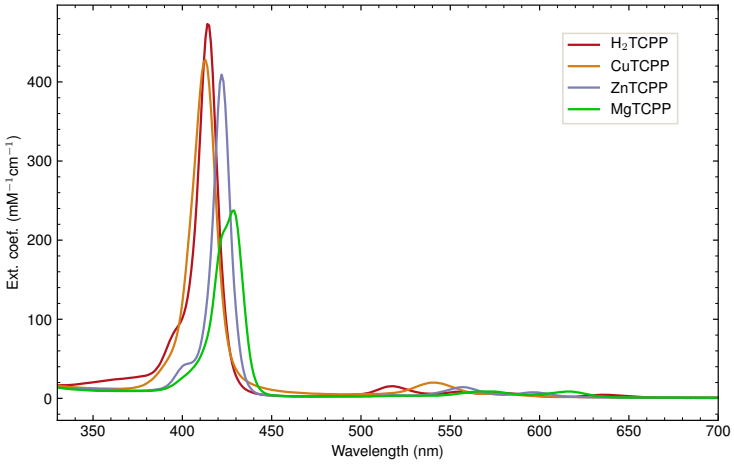

Figure S1 UV/VIS spectra of free base, copper, zinc, and magnesium TCPP in basic aqueous solution.

NEXAFS decomposition

The decomposition of the experimental X-ray absorption spectra of the series of TCPPs at the N K-edge is shown in Figure S2. Voigt profiles with a fixed Lorenzian FWHM of 0.13 eV[2] were fitted for each recognizable resonance in addition to an arctangent step function to model the edge jump.

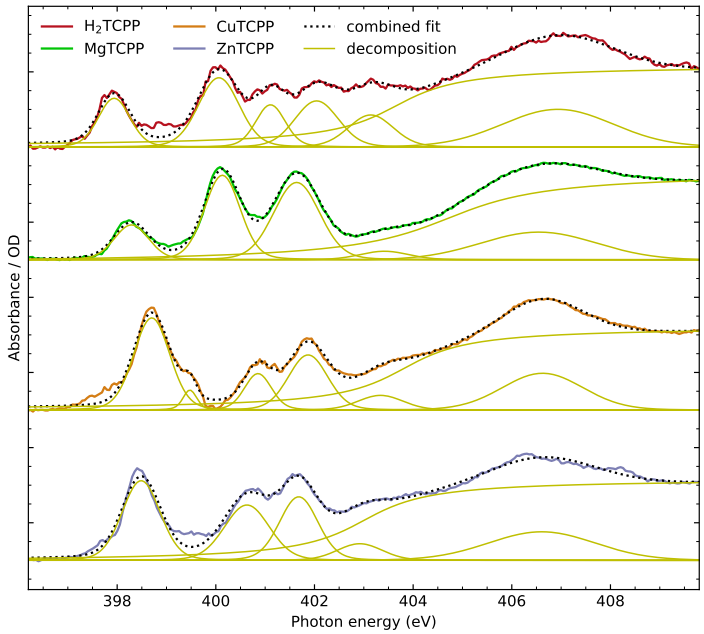

Figure S2 Decomposition of the experimental N K-edge NEXAFS of free base and metal TCPPs by 5-6 Voigt profiles and an arctangent step function.

Molecular geometries

Details of the optimized geometries of the 5,10,15,20-tetraphenylporphyrin (TPP) cores in the gas phase and with implicit solvation (CPCM[3]) are given in Table S1.

Table S1 Calculated TPP N–X bond length (X = H, Mg, Zn, Cu) and phenyl tilt (0° corresponds to a flat arrangement in the porphyrin plane) in the gas phase and with implicit solvation

Molecule	N–X length (gas)	N–X length (CPCM)	phenyl tilt (gas)	phenyl tilt (CPCM)
H_2TPP	2.05 Å	2.06 Å	65.1°	64.1°
MgTPP	2.04 Å	2.04 Å	64.8°	64.5°
ZnTPP	2.01 Å	2.01 Å	66.2°	66.1°
CuTPP	1.01 Å	1.01 Å	66.9°	66.8°

DFT benchmark

In Figure S3, the calculated X-ray absorption spectra of the investigated metal TPP cores are compared. It can be seen that solvation (TD-DFT with CPCM[3] versus gas phase) has a minor effect on the overall spectral shape, but the interspecies shifts are better reproduced with implicit solvation. As discussed in the main article, the inclusion of relaxation by TP-DFT leads to a concentration of the intensities on the energetically lower resonances, which increases the prominence of the experimentally observed features.

If different functionals are compared, it can be seen that the additional feature of CuTPP (b_{1g}) shifts to higher energies with increasing Hartree-Fock exchange (e.g. TD-DFT with CPCM: 398.3 eV for BLYP[4,5], 398.5 eV for B3LYP[6,7], 400.3 eV for BHandHLYP[8]), due to a more accurate description of the metal-ligand interactions. The b_{1g} energy is in qualitative agreement with the experimental data (between the $1e_g$ and b_{2u} peak) for all shown calculations with the BHandHLYP functional and for the cam-B3LYP[9] functional with the transition potential method.

Even though the combination of Hartree-Fock exchange and TP-DFT yields good agreement with the experimental spectra and supports our spectral assignments, this approach is problematic, since the mixing of Kohn-Sham and Hartree-Fock eigenvalues is known to depend strongly on the amount of exchange and core-hole occupation[10].

After all, the experimental shifts are best described by the TD-DFT BHandHLYP calculations, since the transition potential method neglects configuration interactions. As shown in Figure S4, also the shift of the third resonance (b_{2u} around 401.3 eV) upon substitution of NiP is well reproduced by TD-DFT BHandHLYP calculations. The experimental reference has been published by Svirskiy *et al.* [11].

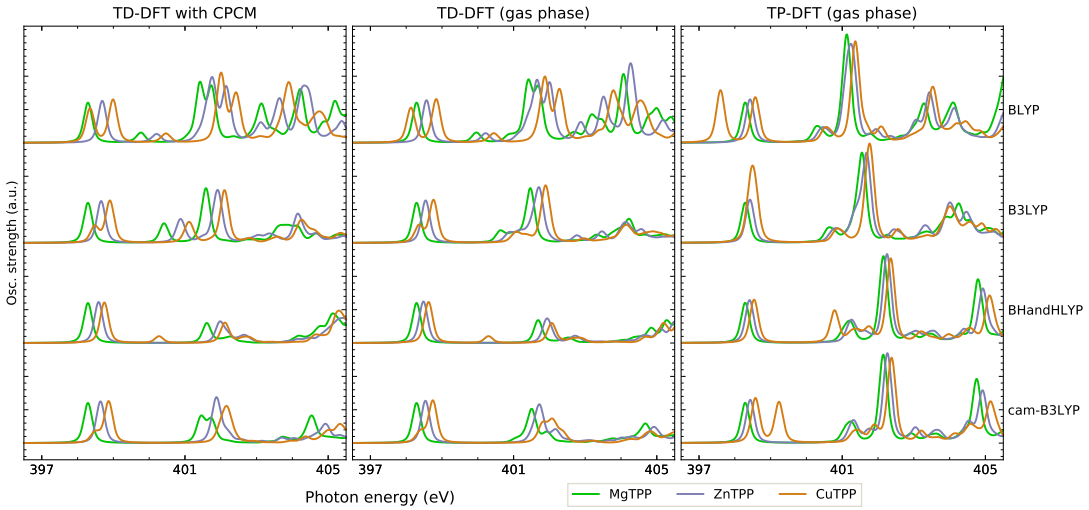

Figure S3 Metal TPP N K-edge NEXAFS calculated by time dependent DFT with and without implicit solvation and by the transition potential method for 4 different functionals (BLYP, B3LYP, BHandHLYP, cam-B3LYP). All transitions were broadened by 0.13 eV^2 (Lorentzian FWHM) and 0.20 eV (Gaussian FWHM) and normalized by the experimental peak height and energy of the first resonance in MgTPP ($1e_g$ at 398.3 eV).

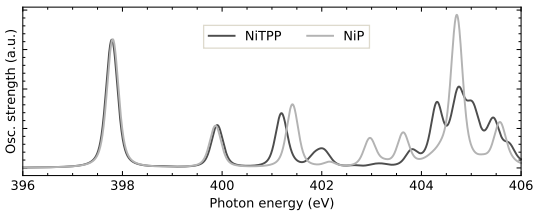

Figure S4 N K-edge NEXAFS of NiP and NiTPP calculated by TD-DFT with the BHandHLYP functional in the gas phase.

References

[1] L. M. Scolaro, M. Castriciano, A. Romeo, S. Patanè, E. Cefalì and M. Allegrini, *J. Phys. Chem. B*, 2002, **106**, 2453–2459.

[2] C. Nicolas and C. Miron, *J. Electron Spectrosc. Relat. Phenom.*, 2012, **185**, 267 – 272.

[3] V. Barone and M. Cossi, *J. Phys. Chem. A*, 1998, **102**, 1995–2001.

[4] A. D. Becke, *Phys. Rev. A*, 1988, **38**, 3098–3100.

[5] C. Lee, W. Yang and R. G. Parr, *Phys. Rev. B*, 1988, **37**, 785–789.

[6] A. D. Becke, *J. Chem. Phys.*, 1993, **98**, 5648–5652.

[7] P. J. Stephens, F. J. Devlin, C. F. Chabalowski and M. J. Frisch, *J. Chem. Phys.*, 1994, **98**, 11623–11627.

[8] A. D. Becke, *J. Chem. Phys.*, 1993, **98**, 1372–1377.

[9] T. Yanai, D. P. Tew and N. C. Handy, *Chem. Phys. Lett.*, 2004, **393**, 51–57.

[10] T. Fransson, I. E. Brumboiu, M. L. Vidal, P. Norman, S. Coriani and A. Dreuw, *J. Chem. Theory Comput.*, 2021, **17**, 1618–1637.

[11] G. I. Svirskiy, A. V. Generalov, A. Y. Klyushin, K. A. Simonov, S. A. Krasnikov, N. A. Vinogradov, A. L. Trigub, Y. V. Zubavichus, A. B. Preobrazhenski and A. S. Vinogradov, *Phys. Solid State*, 2018, **60**, 581–591.

Supplementary Information

Fundamental electronic changes upon intersystem crossing in large aromatic photosensitizers: free base 5,10,15,20-tetrakis(4-carboxylatophenyl)porphyrin

Robby Büchner*, Vinícius Vaz da Cruz*, Nitika Grover, Asterios Charisiadis, Mattis Fondell, Robert Haverkamp, Mathias O. Senge*, and Alexander Föhlisch

Contents

1 Synthesis

Methyl 4-formylbenzoate (50 g, 0.31 mol) was added in a 1 L single necked flask and was fully dissolved in propionic acid (400 mL). The solution was heated at 100 °C and then pyrrole (20.2 mL, 0.31 mol) was added dropwise and the mixture was refluxed for 1.5 h. After the reaction completion, the mixture was cooled to room temperature and submerged in an ice bath. The precipitates were isolated through vacuum filtration, and further recrystallized and washed with methanol to obtain the pure product 5,10,15,20-tetrakis(4-methoxycarbonylphenyl)porphyrin (TCOOMePP) as a purple crystalline powder (12.2 g, 13.23 mmol, yield 17%). ^{1}H NMR spectroscopic data were similar to those previously reported in the literature.[1] [^{1}H NMR (400 MHz, $CDCl_3$) δ = 8.82 (s, 8H), 8.45 (d, J = 8.2 Hz, 8H), 8.30 (d, J = 8.2 Hz, 8H), 4.12 (s, 12H), -2.81 (s, 2H) ppm.]

TCOOMePP (11 g, 12.99 mmol) was dissolved in a (1:1) THF/MeOH mixture (400 mL) and an aqueous solution (80 mL) of KOH (44 g, 779.3 mmol) was then added. The reaction was refluxed overnight. The following day, THF and MeOH were removed under reduced pressure, water was added, and the solution was acidified with 1M HCl and the desired product was precipitated and collected though filtration. Finally, the desired product was washed with a large volume of dichloromethane and dried under vacuum to obtain 5,10,15,20-tetrakis(4-carboxyphenyl)porphyrin (TCPP) as a purple solid (10 g, 12.65 mmol, yield: 97%). ^{1}H NMR spectroscopic data were similar to those previously reported in the literature.[2] [^{1}H NMR (400 MHz, DMSO-d_6) δ = 8.86 (s, 8H), 8.38 (db, J = 7.4 Hz, 8H), 8.31 (db, J = 8.0 Hz, 8H), -2.93 (s, 2H) ppm.]

2 Full ground state and transient spectra

Figure S1 shows the ground state and transient X-ray absorption spectra of aqueous free base $TCPP^{4-}$ (pH≈12) including transitions to the anti-bonding b_{1u} (400.0 eV, 401.1 eV) and higher b_{2g}/b_{3g} vacant orbitals (402.0 eV, 403.1 eV). See the previously published $TCPP^{4-}$ (pH≈8) data[3] for details of this assignment.

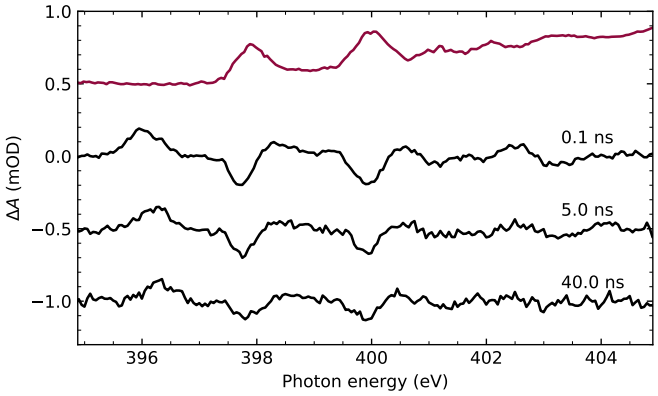

Fig. S1 $TCPP^{4-}$ N K-edge ground state (red) and transient X-ray absorption spectra 0.1 ns, 5.0 ns, 40.0 ns after 343 nm excitation (black).

3 Reconstruction of excited state spectra

The procedure to retrieve approximated N K-edge NEXAFS spectra of the lowest singlet and triplet excited states of $TCPP^{4-}$ is demonstrated in Figure S2. Compared to Figure 4a in the main text, the data is scaled here so that the shown and added ground state contributions are equal. In the main text, the resulting spectra are scaled so that the intensities of the different features is on average the same.

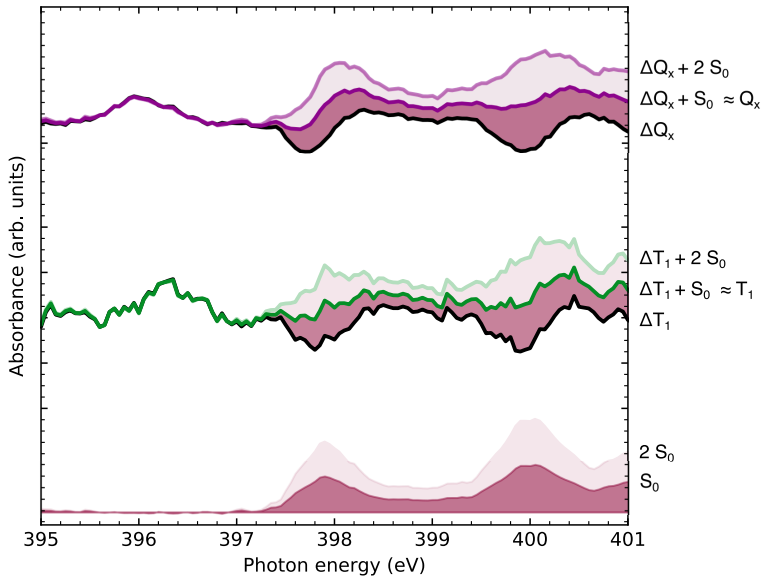

Fig. S2 Reconstruction of the T_1 (green) and Q_x (magenta) excited state spectra by adding the the ground state spectrum S_0 (red area) to the transients (ΔT_1, ΔQ_x – black). The double of the ground state spectrum 2 S_0 (light red area) has been added as well, to show that the depletion is overcompensated in this case (light green/ magenta curves).

The experimentally determined transients at pump-probe delays of 0.1 ns (ΔQ_x) and 40.0 ns (ΔT_1) are dominated by the ground state depletion above 397.5 eV. To make double excitations (as observed for a zinc porphyrin[4]) visible, the ground state spectrum (S_0)

has been added to the transient spectra. To retrieve reproducible results, the intensity of the transients has been scaled so that the absorbance at the minimum region of the depletion dips is zero.

4 Optimized geometries

The calculated out-of-plane distortions of the free base 5,10,15,20-tetraphenylporphyrin (TPP) geometry in the optically excited states (Q_x, T_1) compared to the ground state (S_0) can be seen in Figure S3.

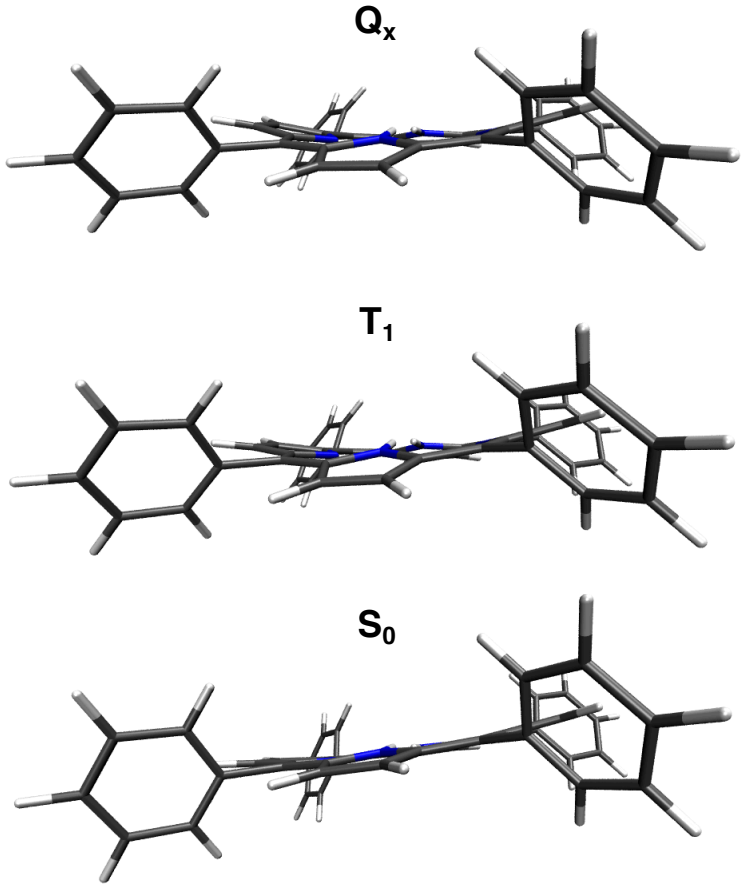

Fig. S3 Optimized geometries of TPP in the lowest singlet excited (Q_x), triplet excited(T_1), and ground state (S_0).

5 Application of the restricted subspace approximation

TD-DFT calculations within the restricted subspace approximation (RSA) were originally proposed to simulate resonant inelastic X-ray scattering (RIXS) spectra.[5] However, the procedure is also applicable to the modelling of pre-edge transient X-ray absorption features, as it has been carried out in this work. By truncating the excitation spaces we obtain the necessary valence- and core-excited states relevant to transient absorption. In this work, the virtual space was made up by the 20 lowest unoccupied orbitals, while the occupied space was comprised of the nitrogen 1s orbital (either =N– or –NH–) and the four highest occupied orbitals, leading to an orbital space (1,4,20). Then 170 roots were computed, populating the valence excitations and core excitation from the selected orbitals. The calculations were carried out from an unrestricted Kohn-Sham ground state determinant, which allows to compute also excited states with a spin flip. Lastly, the X-ray absorption spectra for each electronic state were obtained by using Multiwfn[6] to compute the transition dipole moment between the states. The ground state optical and X-ray absorption spectra of TPP are compared to the classical (full) TD-DFT outcome in Figure S4.

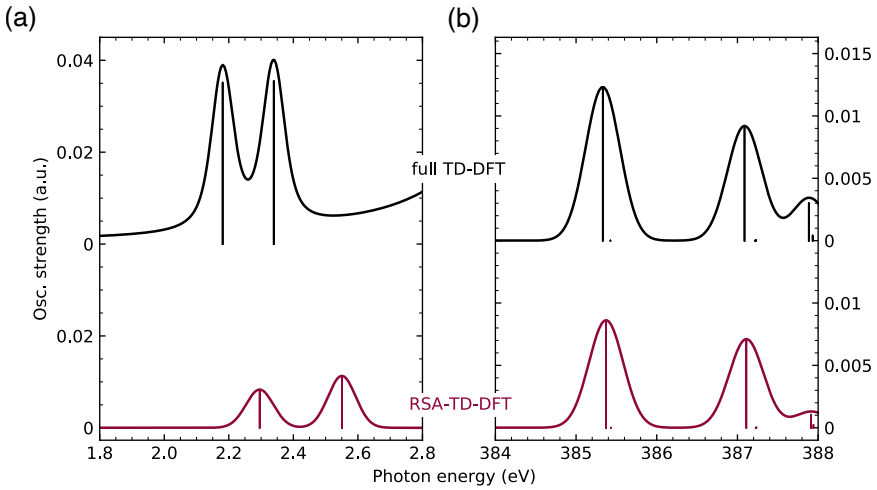

Fig. S4 TD-DFT calculation of the TPP (a) optical bands and (b) N K-edge NEXAFS within and without the restricted subspace approximation (RSA).

References

1 Y. Keum, S. Park, Y.-P. Chen and J. Park, *Angew. Chem., Int. Ed.*, 2018, **57**, 14852–14856.

2 P. Deria, J. Yu, R. P. Balaraman, J. Mashni and S. N. White, *Chem. Commun.*, 2016, **52**, 13031–13034.

3 R. Büchner, M. Fondell, R. Haverkamp, A. Pietzsch, V. Vaz da Cruz and A. Föhlisch, *Phys. Chem. Chem. Phys.*, 2021, **23**, 24765–24772.

4 A. A. Cordones, C. D. Pemmaraju, J. H. Lee, I. Zegkinoglou, M.-E. Ragoussi, F. J. Himpsel, G. de la Torre and R. W. Schoenlein, *J. Phys. Chem. Lett.*, 2021, **12**, 1182–1188.

5 V. Vaz da Cruz, S. Eckert and A. Föhlisch, *Phys. Chem. Chem. Phys.*, 2021, **23**, 1835–1848.

6 T. Lu and F. Chen, *J. Comput. Chem.*, 2012, **33**, 580–592.

Acknowledgments

Last but not least, I would like to thank all the people in and outside science, who supported me during my PhD. I owe particular thanks to ...

... Alexander Föhlisch for this challenging, but fascinating PhD project; the confidence in its success and the encouraging guidance through the years.

... Tobias Lau as my second supervisor for productive and expedient progress meetings. And thanks to you and your team at the neighboring beamline for some extra minutes of beamtime whenever our liquid jet was finally running at the end of a shift.

... Annette Pietzsch for mentoring me since my first day at BESSY II.

... Prof. Dr. Birgit Kanngießer and Prof. Dr. Jan-Erik Rubensson for reviewing this thesis as well as Prof. Dr. Matias Bargheer for chairing the committee.

... Mattis Fondell for not giving up on my hardly soluble samples and enduring the unpleasant smell of test runs with various solvents. And together with Artur Born and Robert Haverkamp for an amazing working spirit at the beamline, in the office, and on the court.

... Vinícus Vaz da Cruz for sharing your deep expertise on physical chemistry and setting up all the calculations for the publications.

... Mathias Senge and your co-workers for finding and synthesizing sufficiently soluble porphyrin derivatives enabling this thesis in the present form.

... Rolf Mitzner for the substantial support in the preparation of pump-probe experiments.

... Sebastian Eckert for sharing your scientific expertise.

... Stefan Neppl and Eric Mascarenhas for supporting numerous beamtimes.

... my family and friends for a large number of emotional and nutritional care packages.

... Kevin Huber for all your support and unwavering patience during an unexpected deep dive into the world of synchrotron science with an occasionally hangry or frustrated boyfriend in our shared home office. I'm so lucky to have you.